Chapter 1

Introduction

1.1 High-Speed Milling and Applications

High Speed Milling, like other metal cutting processes, is a kind of chip-forming machining process, in which the unneeded work-piece material is removed by a well-shaped cutting tool. “High-speed”, in general, refers to cutting and/or rotational speeds that are significantly higher, say 10 times higher, than those used in conventional milling. For example, in high speed cutting aluminum (say, type: Al 7075) with a ball-end mill coated with TiCN, the cutting speed v_c (m/min) can reach 2,000 m/min or above. In high speed cutting hard steel (say, ORVAR steel: HRC 52) with a carbide ball-end mill (e.g. type: PWZH8074118TAX made by SANDVIK), the cutting speed can reach 800 m/min or even above with cooling fluid, for example, Blaser 2000 (7%). Figure 1.1 (a) and (b) show some examples in application for high-speed machining in comparison with conventional machining.

Saloman was one of the first proponents of high speed machining. After he filed his application for German patent on machining at high cutting speeds in 1931, it took more than 50 years until appropriate machines with high rotational speeds were available for the practical application of high-speed milling technology.
The considerable increase of material removal rate at high-speed cutting justifies machining parts that would previously have been made by other manufacturing methods for example casting or forging.
In addition by combining separate components into a single part machined at high-speed, the costs of assembly and fixture storage can be

substantially reduced and the strength and rigidity of them can be significantly improved.
Important applications of high-speed milling include manufacture of thin walled, ribbed, aluminum components for aircraft and transmission cases for automobile and machining of sculptured surfaces in die and mold making.

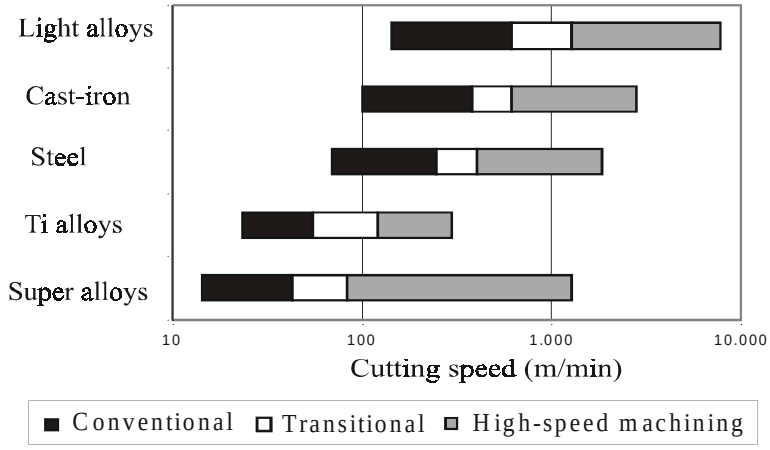

(a)

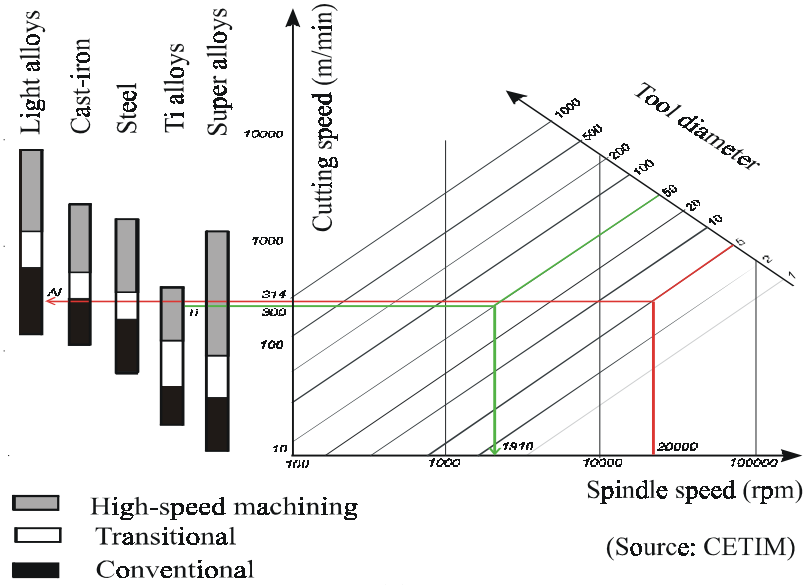

(b)

Figure 1.1: Examples in application for high-speed machining in comparison with conventional machining

1.2 Challenges for Force Evaluation and Chatter Prediction in High-speed Milling

To make full use of the high speed milling technology, we need first to understand the cutting process and then optimize the process by correctly selecting cutting parameters.

Instantaneous cutting force information helps us to know the chip load at any instant during cutting and thus facilitates the understanding of chip formation mechanism and the optimization of NC (numeric control) programs.
In high-speed milling, however, force measurement and/or evaluation is a challenging task. The high-speed milling process is characterized by intermittent strong impact when the tool enters/exits the workpiece material.
The force produced at high rotation/cutting speed contains high harmonics, which are usually in the neighborhood of the milling system's natural frequencies.
These high frequency harmonic excitations make the milling system vibrate at or near the system's resonance frequencies and thus result in dynamic noise in the force measurement due to the low damping of the dynamometer.
If these high frequencies are filtered out with a low pass filter, the cutting force signals may also be significantly filtered out together with the dynamic noises.

To optimize the cutting process, we need to find the optimal cutting conditions and cutting parameters to avoid chatter vibration and maximize the metal removal rate.
Chatter is a self-excited vibration due to interaction of the structural and process dynamics.
To analytically predict chatter, we require the knowledge of the system dynamics, i.e., modal parameters of the machine structure and process constant (i.e., specific cutting force).
In high-speed milling, chatter frequency detected from tests is often about 1 ~ 5 kHz. In a modern machine, the geometrical are very small so that the stiffness in the joints is very high and the damping is very small, resulting in high natural frequencies and low damping. These high natural frequencies and low damping (i.e. dynamic very compliant machine) are responsible for those high chatter frequencies.
Measuring the high harmonic frequency components of the transfer functions of the tool/tool-holder/spindle structure is quite difficult or impossible with hammer excitation (see Figure 4.4 (a) and (b) in section

4.2.3). The process constant is also not easy to obtain in case of high speed milling due to the difficulties in force measurement (see section 3.3).

1.3 Objective and Major Achievements

The objective of this dissertation, is to measure and evaluate the instantaneous high-speed milling force and to find the optimal cutting parameters (i.e., the most stable cutting zone in terms of spindle speed and depth of cut) to avoid chatter vibration.

New strategies have been developed within this doctoral research for evaluating the cutting force and obtaining the analytical stability lobes (see Figure 2.3 in Chapter 2) for chatter avoidance and process optimization in high-speed milling.
To evaluate the high-speed milling force, the force compensation method and the force coefficient identification technique are developed and verified.
A study of the cutting process by comparing the specific cutting force at different cutting speeds is also given in this thesis.
A practical way of identifying the natural frequencies and damping ratios of the structure and the process constant without measuring the transfer functions of the milling system as seen at the tip of the tool has been developed and described in detail. As a result, analytical prediction of chatter becomes feasible.
A strategy for selection of optimal spindle speed and axial depth of cut to avoid chatter vibration is thus developed and verified in high-speed milling of aluminum.
Based on this strategy, it is possible to incorporate the stability lobes into CAD/CAM systems to avoid chatter rather than measure the transfer functions and specific cutting forces separately before cutting.

1.4 Overview of this Thesis

In order to help readers to have insight into dynamics, force evaluation, chatter avoidance, and process optimization in high speed milling, the contents of this dissertation are organized as follows:

The second chapter (Chapter 2 “State of the Art of Force Measurement/Evaluation and Chatter Avoidance”) introduces the

instantaneous cutting force measurement and evaluation technique, which is essential for the modeling of the milling system's dynamics and helpful for the study of the cutting process. This chapter also reviews the research on chatter control in milling and overviews the state of the art of chatter control strategies.
The third chapter (Chapter 3 "Cutting Forces in High-speed Milling") describes Kienzle's formula currently used in the force evaluation and the dynamic model of a dynamometer. A compensation method to take the dynamic effect of the dynamometer into account for high-speed milling force measurement is illustrated. The strategy for evaluating specific cutting forces in high-speed milling is developed and explained in detail in this chapter. Force prediction in 5-axis milling with a helical-fluted cutter is discussed. A study of the milling process by comparing the specific cutting forces at different cutting speeds is illustrated in this chapter as well.

The fourth chapter (Chapter 4 "Chatter in High-Speed Milling") presents the measurement result of the frequency response function (FRF) of a typical tool/tool-holder/spindle assembly used in high-speed milling. The influence of transient vibration on tool wear and part surface roughness in high-speed milling of hard steel is experimentally investigated and discussed. Chatter vibration in high-speed milling of aluminum and steel with different cutting parameters is studied. The test results are presented. The method for analytical prediction of stability lobes in high-speed milling is described in detail for both a single and multiple degree-of-freedom system. Finally the strategy for the selection of optimal spindle speed to avoid chatter is described and experimentally verified in high-speed milling of aluminum.

The fifth chapter (Chapter 5 "General Conclusions and Future Work") gives the main conclusions drawn from this research and recommendations for the future.

Chapter 2

State of the Art of Force Measurement/Evaluation and Chatter Avoidance

2.1 Cutting Force Measurement/Evaluation

Cutting force information facilitates the theoretical and experimental study of tool failure and tool life, system dynamics and the optimization of NC programs. It is important, by adjusting spindle speed and/or feed and/or engagement parameters, to maintain reasonable loads on machine/cutting tool.

Researchers all over the world have contributed constantly to the improvement and enlargement of the know-how in force measurement, estimation and modeling.
Peters, Vanherck and Van Brussel [43] have done valuable work in measuring the dynamic force coefficient in turning operation. Armarego, et. al. [6, 7] developed a computer-aided predictive cutting model for face milling allowing for eccentricity, cutter deflections and tooth run-out. Altintas et. al. [2, 4, 5] have also contributed series of papers to the mechanistic modeling of the cutting force in milling. Tlusty and Smith [56, 71] overviewed the modeling and milling simulation process. Many other force evaluation-related research works can also be found in publications (for example, [1, 8, 9, 10, 12, 13, 23, 24, 27, 28, 29, 31, 37, 41, 46, 47, 49, 58, 59, 60, 62, 63, 64, 74, 75, 76, 82, 83, 84, 85, 86, 87]).

All the above mentioned research has however been done in conventional cutting/milling. Whatever kind of force model is used to predict/evaluate the cutting force, the force coefficients of the model need to be identified from experimental force measurements. In conventional milling, this is usually done by measuring the cutting force components with a dynamometer. The force measurement in conventional milling is relatively easier than that in high-speed milling. Direct measurement of high-speed milling force is a challenging task.

In high-speed milling, strong impact is induced while the tool enters/exits the work-piece material. The measured force signals are significantly deteriorated by the dynamic noise as mentioned in section 1.2. There are very limited publications found to deal with high-speed milling force measurement/evaluation.
Several solutions have been suggested for the evaluation of high-speed milling forces. For example, Schulz and Hock [48] tried to re-compute the forces for a linear system by knowing the transfer functions of the milling systems. Rotberg, Shoval and Ber [46] suggested to calculate the total cutting forces based on the basic cutting force functions obtained from an experiment under a low impact cutting condition.
Through this doctoral research, force compensation and coefficient methods (see section 3.4 and 3.5) are developed.

2.2 Chatter Avoidance

Another key issue in terms of process optimization in high-speed milling is the instability of the cutting process. The process dynamics depend on the values of the machining parameters such as spindle speed and depth of cut. During cutting the structural and process dynamics are intrinsically coupled.

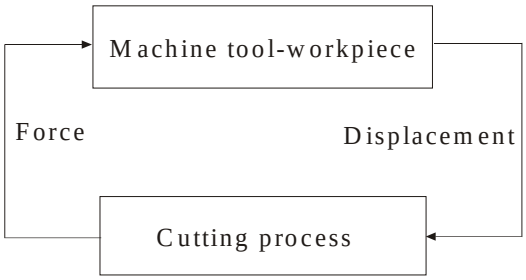

Figure 2.1: A closed feedback loop of cutting process and structural dynamics

The cutting force excites the machine tool structure, which responds with a tool relative displacement. This displacement in turn induces fluctuating dynamic forces.
The coupling effect can be described by a closed feedback loop, as schematically shown in Figure 2.1.
Chatter is a kind of self-excited vibration, which is the result of the interaction between the structure and the cutting process when the closed loop milling system becomes unstable.
Chatter results from the regeneration of chip thickness by the mechanism of the regenerative dynamic cutting process, as schematically illustrated in Figure 2.2.

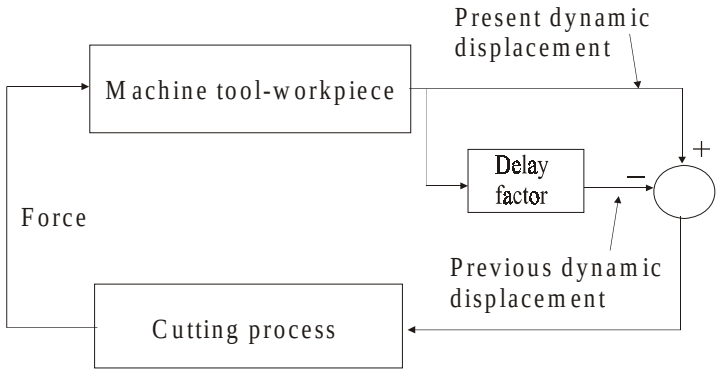

Figure 2.2: A schematic presentation of regenerative process

In Figure 2.2, we see that regeneration of chip thickness variation results from the phase shift between the present dynamic displacement and the previous one when the tool passed the same point as indicated through the time delay factor in the diagram.
With the knowledge of chatter phenomenon and the fundamental mechanism behind it, manufacturers attempt to design machine tools (including tool-holder/tool clamping assembly) with sufficient stiffness and damping so that chatter problem can be minimized in cutting.
When chatter does occur, system parameters such as spindle speed, depth of cut can be adjusted to avoid chatter.

Van Brussel [77] studied the chatter problem in turning operation as his Ph.D dissertation under the supervision of Peters. Vanherck did many research works in this field including developing a passive control approach. He used irregularly spaced teeth in a milling cutter to combat the regenerative effect. Tlusty et. al. [66, 67, 68, 69, 70, 71, 72, 73] did a

lot of research in analyzing the regenerative effects on the system's instability and described how the sound generated by chatter can be used for recognition of the occurrence of chatter. Altintas, Y. and Budak, E. [3] presented an analytical method to predict chatter in milling and derived a model of the dynamic milling process by considering Fourier series expansion of the time varying milling force coefficients and taking the average component of it. Eigenvalues of the dynamic milling expression are therefore calculated analytically by selecting a chatter frequency around the dominant structure's modes. The chatter free axial depth of cuts and spindle speeds are finally analytically formulated as a function of the structure's transfer functions at the tool-workpiece contact zone, static cutting force constants, number of teeth and radial depth of cut. Besides the above-mentioned research, there has been considerable work in techniques for chatter suppression/prediction in the world: see for example [15, 16, 18, 19, 20, 21, 22, 33, 34, 40, 44, 50, 51, 52, 53, 54, 57, 61, 65, 66, 69, 78, 79, 80, 81].

In summary, two general strategies have been developed for chatter avoidance. One is the active process control technique through a feedback control system or the passive control approach with intentionally designed cutter geometry. The other is the process planning method by predicting the stable/unstable zones based on the analytical stability lobes calculated (see for example Figure 2.3).

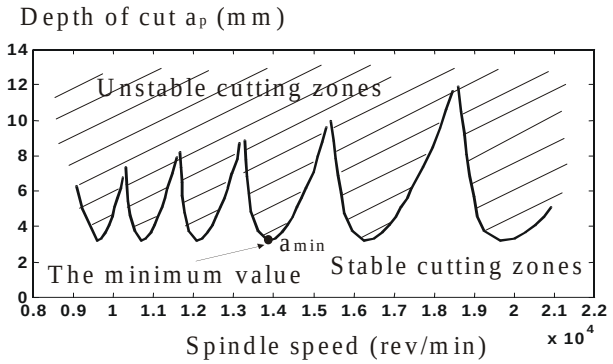

Figure 2.3: Stability lobes delimiting stable/ unstable cutting zones.

These two strategies face challenges in case of high-speed milling. The former needs to design a reliable feedback control system with a very quick response. The latter requires the frequency response function (FRF) of the structure as seen at the tip of the tool and the specific cutting forces

for the models. Both the transfer functions and specific forces in case of high-speed milling are not easy to obtain as mentioned in section 1.2.
Smith et. al. and Tlusty [55] attempted to detect chatter in high-speed milling with a microphone and stabilise the cutting process by regulating the spindle speed. The disadvantage of this method is that when you detect the occurrence of chattering, the part being machined has already been damaged on the one hand and on the other hand the regulated spindle speed by this way may not be optimal.
A practical way to obtain the analytical stability lobes for chatter avoidance in high-speed milling has been developed and verified by the author of this thesis and will be described in detail in Chapter 4.

Chapter 3

Cutting Force in High Speed Milling

3.1 Introduction

Instantaneous force data are helpful for theoretical and experimental studies of the cutting process. The need for readily available and reliable quantitative instantaneous force information is emphasized by the metal cutting industry.
There is an amount of previous research in this field (refer to section 2.1). In this chapter, the study of cutting force is done from the particular point of view of high-speed milling. The dynamics of a dynamometer is discussed in detail. A force compensation method is introduced to take the dynamic effect of the dynamometer into account for force measurement. A technique of evaluating the force coefficients is also presented. In addition, a way of predicting cutting force in 5-axis milling with complicated tool geometry is described by using Kienzle's force model. A study of the milling process by comparing the specific cutting forces at different cutting speeds is illustrated in this chapter as well.

3.2 O. Kienzle's Empirical Force Model

3.2.1 Influential Factors on Cutting Force

There are a lot of factors that influence cutting force. In general, they are physical/chemical properties of the workpiece/tool materials and the

cutting conditions used for a specific machining process.
The material properties include hardness, yield/shear strength, thermal conductivity, melting point, and so on. At high speeds, material temperatures increase. The heat is concentrated in the chip and the workpiece keeps cool. Peak stresses decrease due to thermal softening of the material. The softening effect could decrease the magnitude of the cutting force.
The cutting conditions include the cutting parameters (for example, cutting/rotation speeds, feed rate, and width of cut), tool type/geometry, and lubrication type. In high speed milling, increase of cutting speed will induce a strong impact at the material entry/exit. This impact may result in a significant dynamic force variation and structural vibration in the neighbourhood of the system's resonance frequencies. The dynamic vibration noise will deteriorate the measured force signals.
It is unrealistic to include all these influential factors in a simple equation to model the cutting force. There are many methods in practice to calculate cutting forces for various milling operations. These methods are all based on empirical force models such as linear force model [10], exponential force model [7], mechanistic force model [2], and high-order force model [4].

3.2.2 O. Kienzle's Force Model

O. Kienzle took just a few direct factors into account and established a simple equation to model the cutting force in turning. This formula has proved sufficient in terms of accuracy for many applications.
The basic Kienzle equation is written as $F_c = k_c A$. The cross section of the cut (A) is a function of both the nominal cut thickness and the width of cut. The specific cutting force k_c depends on the properties of the tool/work-piece material pair (hardness, strength, and friction coefficient…), the lubrication type, cutting speed, and geometrical tool parameters. Experimental results in turning have shown that the specific cutting force k_c can be further expressed as $k_c = k_{c1.1}\, h^{-m_c}$. Where $k_{c1.1}$ and m_c are material-dependent constants and h is the thickness of cut.
Although O. Kienzle's force formula has been verified for the case of turning operation, this formula can still be used for the calculation of the tangential force component in a wide range of engagement (chip thickness) of milling operation except at the material entry/exit. The specific cutting force k_c and the constant m_c in O. Kienzle's force formula are calculated from the measured cutting force data, which are usually acquired from a specific cutting process by the use of a dynamometer.
The force measurement with a dynamometer in milling, particularly in

high-speed milling, is more difficult than that in turning (see section 1.2).

3.3 Milling Force Measurement

3.3.1 The Measuring Chain

A force measuring chain is functionally illustrated in Figure 3.1. It mainly consists of the dynamometer on which the workpiece is clamped, charge amplifier, and PC.
In milling, the cutting force produced from the chip formation process between the cutter and workpiece acts on the workpiece and is transmitted to the dynamometer. The exerted force leads to a deformation of the piezoelectric sensors of the dynamometer. The deforming piezoelectric sensors produce electric charges in correspondence with the relative deformation of the sensors. These electric charges are processed following several steps of signal conditioning and digitalization. At last a data file is saved in memory for the user.

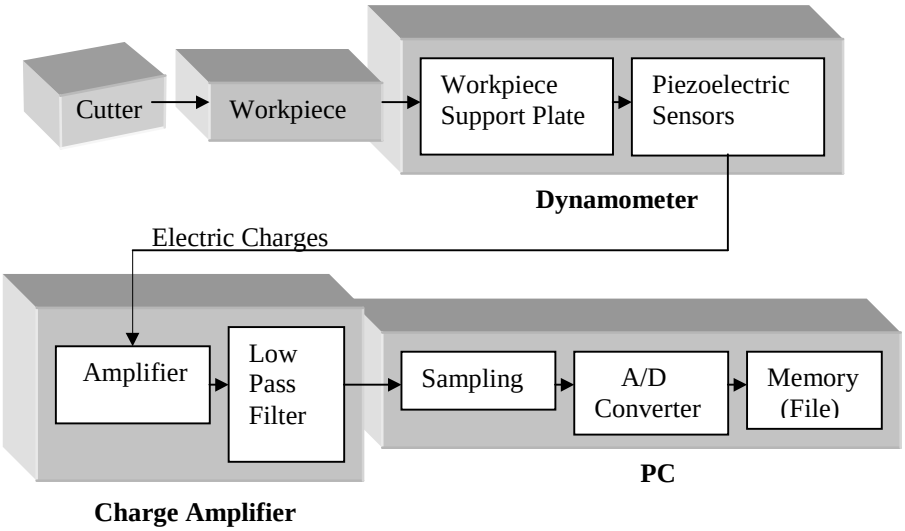

Figure 3.1: Force measurement and data acquisition devices

3.3.2 Dynamic Model of the Dynamometer

The validity of the acquired force data through the above measuring chain depends not only on the accuracy of all the calibrated hardware devices used and their parameter settings, but also the dynamic effect of the dynamometer itself, particularly when measuring forces in high-speed milling. In conventional milling, the tooth passing frequency is usually much lower than the natural frequencies of the dynamometer, say, less than one third of them. In high speed milling, however, the tooth passing frequency and/or the high harmonic frequency components induced from the impact force at material entry/exit are often in the neighborhood of the natural frequencies of the dynamometer. The vibration of the structure including the dynamometer therefore significantly deteriorate the measured force signals because the high frequency harmonic components of the cutting force are in the neighborhood of the dynamometer's natural frequencies and thus are exaggerated in the output signals.
To take into account the influences of the dynamometer's dynamics on the force measurement, dynamic models of the dynamometer need to be established.
The piezoelectric sensors of the dynamometer can be treated as elastic bodies and thus can be mechanistically described by means of spring-damper-mass model and its equivalent scheme can be shown in Figure 3.2 for a single degree-of-freedom case.

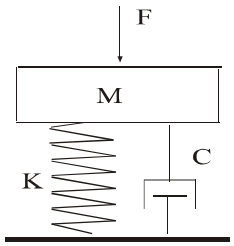

Figure 3.2: A spring-damper-mass model of a dynamometer

Where:
F is the exerting force component on the top plate of the dynamometer together with workpiece.
M is the effective mass of the dynamometer.
K is the static stiffness of the dynamometer.
C is the damping coefficient.

Assuming that the machine structure has an infinite stiffness, the dynamic stiffness (G(s)) of the milling system can be mathematically written as

$$G(s) = Ms^2 + Cs + K$$

Where: s is the Laplace variable.

Given that the equivalent voltage building-up capacitance of the charge amplifier is C_g and that the sensitivity of the sensor in Coulomb per unit displacement is K_{Ts}, then the relationship between input cutting force (F(s)) and output voltage (V(s)) for an ideal measuring chain is

$$F(s) = G(s) \cdot (\frac{1}{K_{Ts}}) \cdot C_g \cdot V(s)$$

Or in the frequency domain, we have

$$\begin{aligned} F(j\omega) &= G(j\omega) \cdot (\frac{1}{K_{Ts}}) \cdot C_g \cdot V(j\omega) \\ &= \text{Scale} \cdot \frac{(-M\omega^2 + j\omega C + K)}{K} \cdot V(j\omega). \end{aligned}$$

Where: $\text{Scale} = \frac{K}{K_{Ts}} \cdot C_g$

The cutting force (F(t)) in discrete time can be readily computed from the inverse Fourier transform as follows:

$$F(n) = \frac{1}{N} \sum_{k=1}^{N} F(jk) \cdot e^{j(k-1)\frac{2\pi}{N}(n-1)}$$

$$F(jk) = \frac{\text{Scale}}{K} \{-M[(k-1) \cdot 2\pi f_o]^2 + j(k-1) \cdot 2\pi f_o C + K\} \sum_{n=1}^{N} V(n) \cdot e^{-j(k-1)\frac{2\pi}{N}(n-1)}$$

Where:
f_o is the fundamental frequency (Hz)
N is the number of points sampled in a chosen window.
V(n) are the measured voltages in discrete time.

Noting that the damping coefficient (C), compared with the stiffness (K), is very small, the equation of F(jk) can therefore be simplified as

$$F(jk)=\frac{Scale}{K}\left\{-M[(k-1)\cdot 2\pi f_o]^2+K\right\}\sum_{n=1}^{N}V(n)\cdot e^{-j(k-1)\frac{2\pi}{N}(n-1)}$$

If the significant highest harmonic frequency component of the force inputs is in the valid measurement range, say, less than one third of the natural frequency of the dynamometer, then the nonlinear term $\{-M[(k-1)2\pi f_o\}^2$ in the equation can also be neglected. This equation is further simplified as

$$F(jk)=\frac{Scale}{K}\cdot K\cdot\sum_{n=1}^{N}V(n)\cdot e^{-j(k-1)\frac{2\pi}{N}(n-1)}$$
$$=Scale\sum_{n=1}^{N}V(n)\cdot e^{-j(k-1)\frac{2\pi}{N}(n-1)}$$

It means that the output voltage is proportional to the input force by a factor (Scale). The force measurement is based on this linear relationship. The relationship holds when the highest harmonic frequency component of the input force is very low compared with the dynamometer's natural frequencies, say, less than one third of the dynamometer's natural frequencies if the mass of the workpiece can be negligible.

In high speed milling, however, it is normal that tooth frequencies and/or high harmonic frequency components are of two thirds or in the neighborhood of the dynamometer's natural frequency. To obtain the cutting force data in high speed milling, compensation/discounting of the inertia forces is necessary to improve the measurement results.

3.4 Compensation Method in High-Speed Milling Force Measurement

The basic idea of the compensation method is that the inertia force of the workpiece together with the dynamometer's equivalent mass has to be taken into account to compensate for the dynamic effect of the dynamometer. The accelerations of the workpiece in a global reference system (i.e. a Newton inertia reference system) are measured with accelerometers.

3.4.1 Experimental Set-up

A schematic presentation of milling operation and the arrangement of the measurement system are shown in Figure 3.3. The tests were conducted on a 3-axis high-speed milling machine (Matsuura FX-5G). A KISTLER dynamometer Type 9265B together with a clamping plate Type 9443B was used to measure the three force components. In addition, two three-component PCB shear accelerometers Type 356B08 with a frequency range of 0.5~5,000 Hz were applied to measure the accelerations of the work-piece during cutting. The two accelerometers were symmetrically arranged on the opposite faces of the workpiece. A KISTLER charge amplifier device Type 5017A and DSA200 (Dynamic Signal Analyser series 200) with D-TAC (Difa Transfer And Control) software were used for data acquisition. The cut-off frequencies of the low pass filters inside the charge amplifier device were all set at 10 kHz.

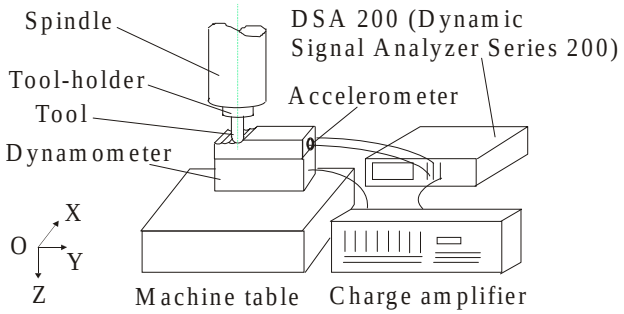

Figure 3.3: Experimental set-up of high-speed milling force measurement by force compensation method

3.4.2 Force and Acceleration Measurements

For the purpose of comparison two tests were done. One is conventional milling with a relatively low speed. The other is high-speed milling. The machining conditions used for both cases are listed in Table 3.1:

Table 3.1: Machining conditions (in dry cutting)

	Test 1	Test 2
Cutting tool	Ball-end mill: ∅10(mm) PWZH80 7418TAX No. of teeth: 2	Ball-end mill: ∅10(mm) PWZH80 74118TAX No. of teeth: 2
Workpiece	C45 (HRC 23)	C45 (HRC 23)
Spindle speed	n=1196 (rpm)	n=6373 (rpm)
Cutting Speed	v_c=38 (m/min)	v_c=200 (m/min)
Feed/tooth	f_z=0.05 (mm)	f_z=0.02 (mm)
Depth of cut	a_p=1 (mm)	a_p=0.4 (mm)
Pick feed	a_e=5 (mm)	a_e=5 (mm)

Both the X-axis force and acceleration measured from Test 1 are given in Figure 3.4 (a) (b) and 3.5 (a) (b), respectively. The sampling frequency used in Test 1 is 6.4 kHz. The window is 0.1 (s). Low pass anti-aliasing filters were all automatically set at 3.2 kHz in the DSA 200 system. The measured force signals (see Fig. 3.4 (a)) are approximately repeating sharp curves and the most significant harmonics are within the frequency range of about 0 ~ 1.375 kHz (see Fig. 3.4 (b)). The acceleration signals (see Fig. 3.5 (b)) indicate two peaks at about 1.05 and 1.37 kHz.
The X-axis force and acceleration measured from Test 2 are given in Figure 3.6 (a) (b) and Figure 3.7 (a) (b), respectively. In Test 2, the sampling frequency is 25.6 kHz. The force curves (see Fig. 3.6 (a)) are also approximately periodic and sharp. Similarly as in Test 1 the harmonics with frequencies higher than 1.375 kHz are not significant (see Fig. 3.6 (b)). However the acceleration signals (see Fig. 3.7 (b)) show that the most significant harmonics are within the frequency range of 0.8 ~ 4 kHz and also two peaks appear at about 1.1 and 1.85 kHz. The amplitudes of the accelerations (see Fig. 3.7 (a)) are significantly larger than those in Test 1 (see Fig. 3.5 (a)).

3.4.3 Force Modification by Considering the Inertia Effect

These experimental results proved that the higher the cutting and rotation speeds, the higher the risk of inducing relatively high frequency vibrations with their harmonic frequencies in the neighbourhood of the dynamometer's resonance frequency (1.8 kHz). Thus the force signals measured may significantly be distorted due to inertia effects.

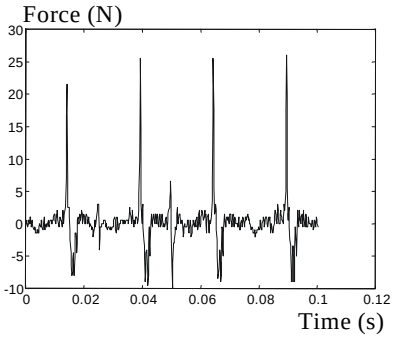

Figure 3.4 (a): X-axis force in the time domain

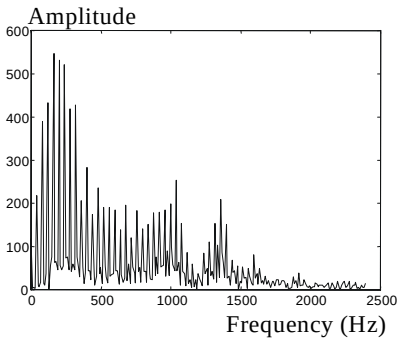

Figure 3.4 (b): X-axis force in the frequency domain

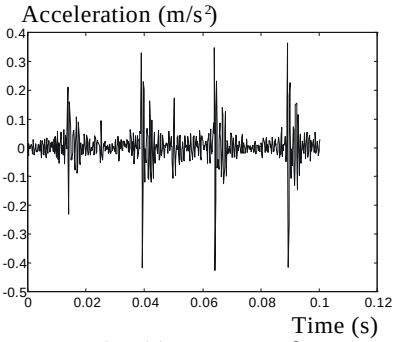

Figure 3.5 (a) X-axis acceleration in the time domain

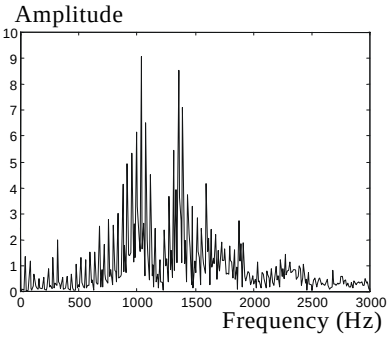

Figure 3.5 (b) X-axis acceleration in the frequency domain

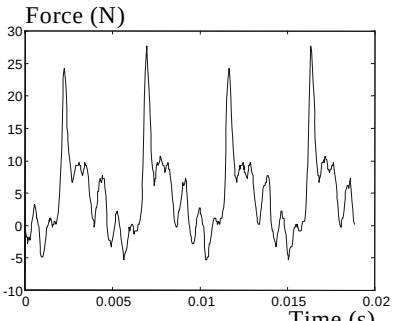

Figure 3.6 (a): X-axis force in the time domain

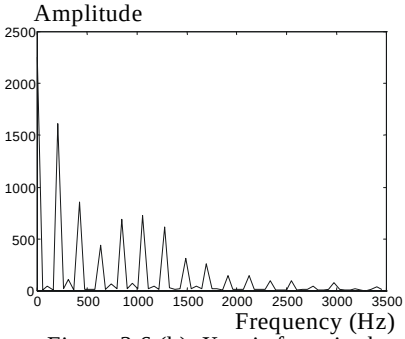

Figure 3.6 (b): X-axis force in the frequency domain

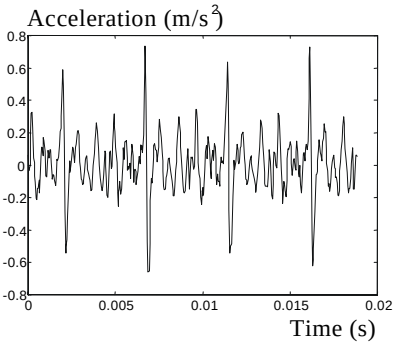

Figure 3.7 (a): X-axis acceleration in the time domain

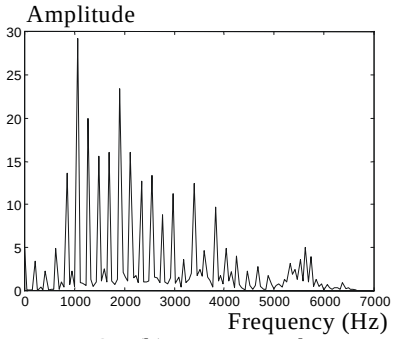

Figure 3.7 (b): X-axis acceleration in the frequency domain

After discounting the inertia force, the modified cutting force is

$$F_{mod} = F_{meas} - F_{inertia}$$

Where:
F_{mod} is the modified cutting force (N).
F_{meas} is the directly measured cutting force (N)
$F_{inertia}$ is the inertia force (N), or $(m_e+m_w)a$, here: m_e (kg) is the equivalent mass of the dynamometer, m_w (kg) is the mass of workpiece, and a (m/s^2) is the measured acceleration.

For both Test 1 and Test 2, the mass of the workpiece is 5 kg and the equivalent mass of the dynamometer is 11 kg. After taking into account the inertia forces, we recalculate the X-axis forces using the above equation. The results are shown in Figure 3.8 (a) (b) and Figure 3.9 (a) (b) for Test 1 and 2, respectively. Comparing Figure 3.8 (a) with Figure 3.4 (a) and also Figure 3.9 (a) with Figure 3.6 (a), we find that the distortion of the force signals for Test 2 is obvious.

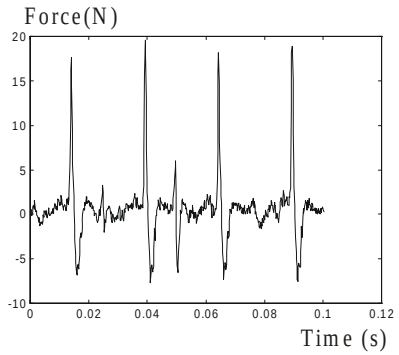

Figure 3.8 (a): Compensated X-axis force in the time domain for Test 1

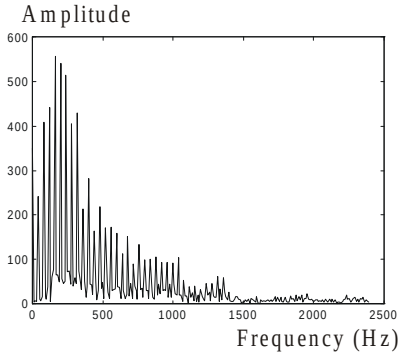

Figure 3.8 (b): Compensated X-axis force in the frequency domain for Test 1

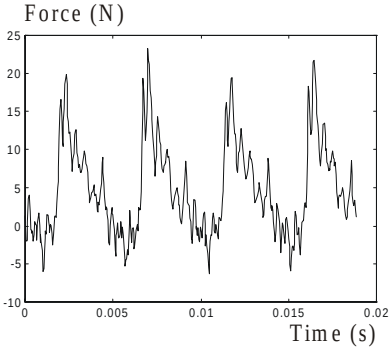

Figure 3.9 (a): Compensaterd X-axis force in the time domain for Test 2

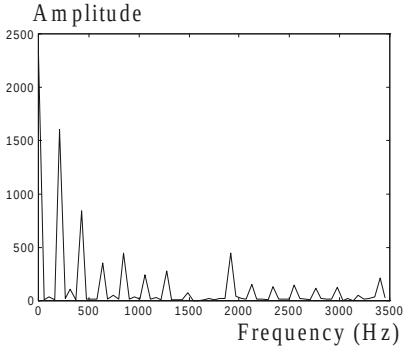

Figure 3.9 (b): Compensated X-axis force in the frequency domain for Test 2

3.5 Identification of Force Coefficients in High Speed Milling

The disadvantage of using previous compensation method is that we have to measure the accelerations on the dynamometer. In this section, a strategy to identify the force coefficients and then the cutting force in high-speed milling without measuring the dynamometer's accelerations is developed. In this method, an engagement matrix of a force model is firstly defined as functions of the nominal cutting parameters. A set of simultaneous equations is then established by considering the dynamic noise effect on the measured results. Force coefficients of the force model are worked out from these equations and cutting force can be calculated from the models.

3.5.1 Engagement Matrix of a Force Model

A schematic presentation of the milling operation is shown in Figure 3.10. F_x and F_y are the force components along the X- and Y-axis, respectively, in the global system XOY. F_t and F_r are the tangent and radial forces.

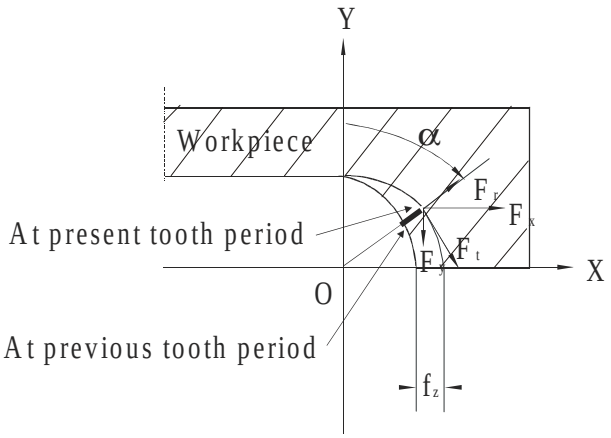

Figure 3.10: A schematic presentation of the milling operation

We use an engagement-dependent matrix together with the force coefficients to model the X and Y force components. The engagement matrix is only dependent on the nominal cutting parameters. Mathematically these force components (F_x and F_y) can be expressed as

$$\begin{bmatrix} F_x \\ F_y \end{bmatrix} = \boldsymbol{U} \begin{bmatrix} k_t \\ k_r \end{bmatrix} \quad (1)$$

$$\boldsymbol{U} = \begin{bmatrix} u_{11} & u_{12} \\ u_{21} & u_{22} \end{bmatrix} \quad (2)$$

Where the matrix $\boldsymbol{U}$ is called engagement matrix. k_t and k_r are force coefficients of the model. The elements (u_{ij}, i, j=1, 2) of $\boldsymbol{U}$ depend on the nominal cutting conditions, i.e. spindle speed, feed per tooth, depth of cut, and the position angle α of the tool tip.

3.5.2 Equations

From equation (1), we can calculate the total theoretical X and Y forces in the XOY system (see Figure 3.10). The real measured forces might be significantly distorted by dynamic noise in a high-speed milling force measurement.
The dynamic noise signals can be expressed as the difference between the directly measured force and the theoretical force in both the X-axis and Y-axis directions.
Here we consider only the two lowest frequency harmonic components as defined by the window related for the FFT analysis of the force signals. This window is taken equal to the tooth period. Or mathematically in the frequency domain as

$$\begin{bmatrix} F_{xnos}(j\omega_0) \\ F_{ynos}(j\omega_0) \end{bmatrix} = \begin{bmatrix} F_{xmes}(j\omega_0) \\ F_{ymes}(j\omega_0) \end{bmatrix} - \boldsymbol{U} \begin{bmatrix} k_t \\ k_r \end{bmatrix} \quad (3)$$

$$\begin{bmatrix} F_{xnos}(j\omega_1) \\ F_{ynos}(j\omega_1) \end{bmatrix} = \begin{bmatrix} F_{xmes}(j\omega_1) \\ F_{ymes}(j\omega_1) \end{bmatrix} - \boldsymbol{U} \begin{bmatrix} k_t \\ k_r \end{bmatrix} \quad (4)$$

Where $F_{xnos}(j\omega_0)$ and $F_{ynos}(j\omega_1)$ are the harmonic components of the dynamic noise force signals in the X- and Y- direction at tooth frequency (ω_0) and double tooth frequency ($\omega_1=2\omega_0$), respectively. $F_{xmes}(j\omega_0)$ and $F_{ymes}(j\omega_1)$ are the harmonic components of directly measured X and Y-axis force signals at these two frequencies, respectively.

We have known that the amplitude of each harmonic component of the measured output voltage is proportional to the amplitude of the

corresponding harmonic component of the input force signals by a factor (Scale) only when the inertia term ($\{-M[(k-1)2\pi f_0\}^2$) can be negligible (see section 3.3.2).
We assume that at angular frequencies ω_0 and ω_1 the inertia terms ($-M\omega_0^2$ and $-M\omega_1^2$) can be neglected. The dynamic noise signals are thus mainly contributed by those harmonics with frequencies higher than ω_1. In the frequency domain, these noise signals (i.e., F_{xnos} and F_{ynos}) at frequencies ω_0 and ω_1 can be considered equal to zero, i.e.,

$$\left|F_{xnos}(j\omega_0)\right| = \left|F_{xnos}(j\omega_1)\right| = 0 \qquad (5)$$

$$\left|F_{ynos}(j\omega_0)\right| = \left|F_{ynos}(j\omega_1)\right| = 0 \qquad (6)$$

From equation (5) and (6), combining with equation (3) and (4), we can work out the force coefficients k_t and k_r.

To have a physical understanding of the above equations, we consider for example the X-axis cutting force and graphically present the relationship (equation (5)) as shown in Figure 3.14.
Figure 3.11 (a) and (b) are the theoretical X-axis cutting force in the time and frequency domain respectively.
Figure 3.12 shows the frequency response function (FRF) of the dynamometer in the X-axis direction.
The directly measured X-axis force is given in Figure 3.13 (a) and (b) in the frequency and time domain respectively.
It is clear that the measured force signals are significantly distorted by the inertia effect at frequency ω_2.
The difference of the measured force and the theoretical one in the frequency domain indicates the induced dynamic noise harmonic component as shown in Figure 3.14.
We find that at frequency ω_0 and ω_1, amplitudes are both almost equal to zero. But at the frequency ω_2, the amplitude is significantly high. This is due to the fact that the input force signal at frequency ω_2 is significantly amplified because the dynamometer has a very small damping ratio (about 0.005~0.01) and ω_2 is in the neighbourhood of the dynamometer's natural frequency ω_n (see Figure 3.12).
If we use a low pass filter to filter out this dynamic noise, then the harmonic component at frequency ω_2 of the actual input force signals will be also filtered out.

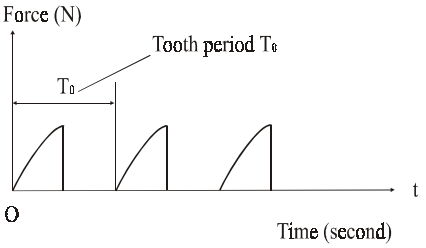

Figure 3.11 (a): The theoretical X-axis cutting force signals in the time domain

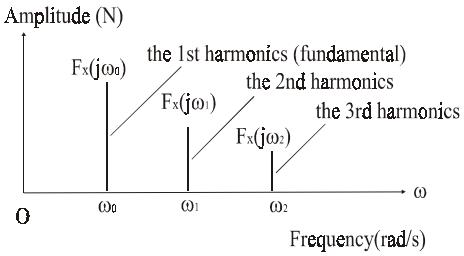

Figure 3.11 (b): The theoretical X-axis cutting force signals in the frequency domain

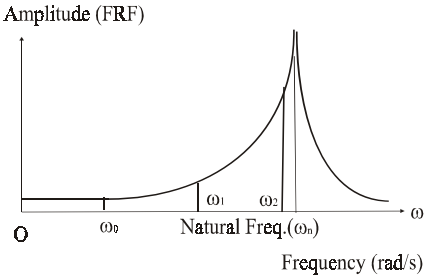

Figure 3.12: The frequency response function (FRF) of the dynamometer

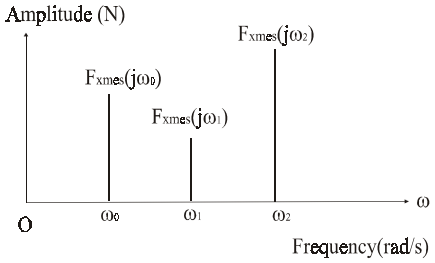

Figure 3.13 (a): The measured X-axis cutting force signals in the frequency domain

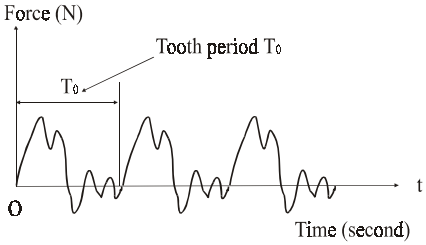

Figure 3.13 (b): The measured X-axis cutting force signals in the time domain

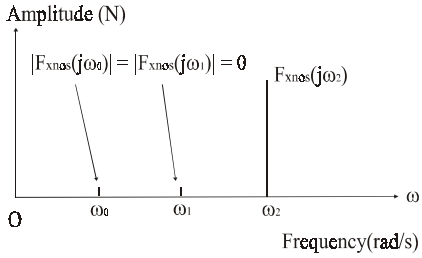

Figure 3.14: The induced dynamic noise signals in the frequency domain, i.e., the difference of Figure 3.13 (a) and Figure 3.11 (b)

3.5.3 Experiments and Application

A ball-end mill with two cutting edges was used in the tests. Figure 3.15 schematically shows the ball end mill engagement.

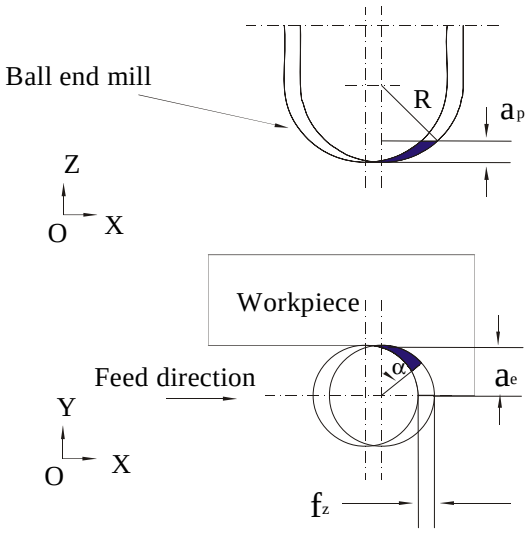

Figure 3.15: A schematic presentation of the ball end mill

As an example, we use Kienzle's force model to define the engagement matrix ***U***. According to Kienzle's empirical law the cutting force is determined by the specific cutting force multiplied by the cross section of the engagement. The instantaneous force components F_x and F_y (refer to Figure 3.10) in the global coordinate system were measured by the dynamometer during cutting. The tangent and radial force components F_t and F_r can be computed through the coordinate transformation from the global (XOY) to the local system (consisting of the F_t and F_r axes) given the rotation angle α. The cross section (S) during the engagement for a ball-end mill can be approximated from the depth of cut (a_p), feed per tooth (f_z) and the position angle α, i.e.

$$S = f_z \cdot a_p \cdot \sin(\alpha) \tag{7}$$

The cutting force F_t and F_r in the local system are

$$F_t = k_t \cdot S = k_t \cdot f_z \cdot a_p \cdot \sin(\alpha) \tag{8}$$

$$F_r = k_r \cdot S = k_r \cdot f_z \cdot a_p \cdot \sin(\alpha) \tag{9}$$

The transformation matrix from local to global system is

$$\begin{bmatrix} \cos(\alpha) & \sin(\alpha) \\ -\sin(\alpha) & \cos(\alpha) \end{bmatrix}$$

The cutting force components in the global system are thereby given as

$$\begin{bmatrix} F_x \\ F_y \end{bmatrix} = \begin{bmatrix} \cos(\alpha) & \sin(\alpha) \\ -\sin(\alpha) & \cos(\alpha) \end{bmatrix} \begin{bmatrix} F_t \\ F_r \end{bmatrix}$$

Substituting (8) and (9) into the above equation, after simple manipulation we obtain

$$\begin{bmatrix} F_x \\ F_y \end{bmatrix} = f_z a_p \sin(\alpha) \begin{bmatrix} \cos(\alpha) & \sin(\alpha) \\ -\sin(\alpha) & \cos(\alpha) \end{bmatrix} \begin{bmatrix} k_t \\ k_r \end{bmatrix}$$

Comparing this matrix equation with equation (1), the engagement matrix is therefore defined as

$$\boldsymbol{U} = f_z a_p \sin(\alpha) \begin{bmatrix} \cos(\alpha) & \sin(\alpha) \\ -\sin(\alpha) & \cos(\alpha) \end{bmatrix} \qquad (10)$$

Or

$$\boldsymbol{U} = f_z a_p \sin(2\pi nt) \begin{bmatrix} \cos(2\pi nt) & \sin(2\pi nt) \\ -\sin(2\pi nt) & \cos(2\pi nt) \end{bmatrix}$$

Where: n is the spindle speed, t is time.

The milling tests were conducted on a 3-axis high-speed machine tool (Matsuura FX-5G).
To measure the total X and Y axis forces (F_x and F_y) in the global system (see Figure 3.10), we used a KISTLER dynamometer (type 9265B) together with a clamping plate (type 9443B). The static stiffness of the dynamometer in both the X and Y directions is 1 kN/μm. Natural frequency in both the X and Y directions is about 1.8 kHz.
A KISTLER charge amplifier 5017A and a Dynamic Signal Analyzer DSA200 with Difa Transfer and Control software D-TAC are employed for the data acquisition.
The cut-off frequencies of the low pass filters inside the charge amplifier device were all set at 10 kHz.
The experimental set-up of the tests is the same as shown in Figure 3.3 in section 3.4 but without the accelerometers. The machining conditions used are given in Table 3.2

Table 3.2: Machining conditions

Cutting tool	Ball-end mill Type:PWZH8074118TAX Diameter: 10 mm Number of teeth: 2
Work-piece	Steel C45 (HRC 23)
Fluid	Dry
Spindle speed	n = 8486 (rpm)
Cutting Speed	v_c = 267 (m/min)
Feed per tooth	f_z = 0.015 (mm)
Depth of cut	a_p= 2 (mm)
Pick feed	a_e = 4 (mm)

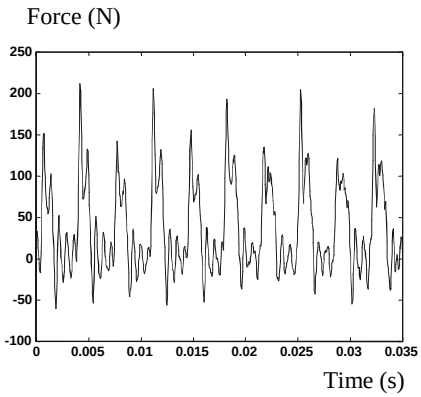

Figure 3.16 (a): X-axis force in the time domain for 5 revolutions

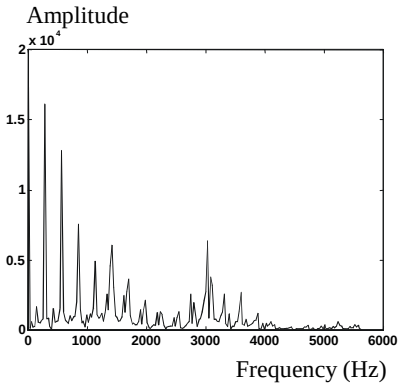

Figure 3.16 (b): X-axis force in the frequency domain for 5 revolutions

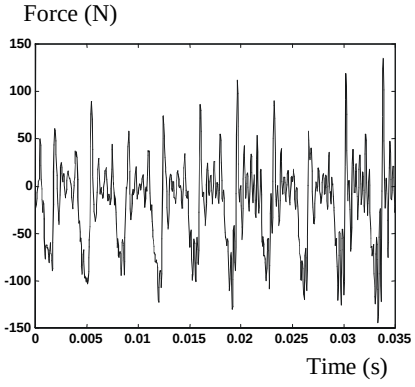

Figure 17 (a): Y-axis force in the time domain for 5 revolutions

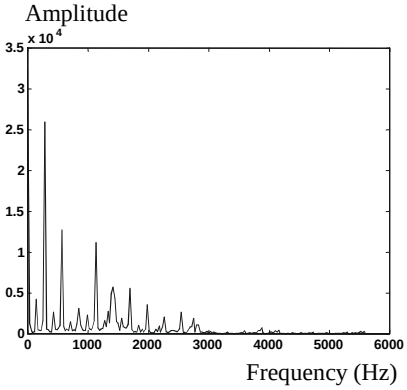

Figure 3.17 (b): Y-axis force in the frequency domain for 5 revolutions

The instantaneous force components F_x and F_y were measured by the dynamometer.
Sampling frequency used is 25.6 kHz. The measured force components F_x and F_y are periodic in the time domain. Based on the sampling frequency and spindle speed used in the tests, a total of 2048 sampling points were acquired with a measuring time of 0.078 seconds.
The measured X and Y force signals for 5 revolutions of cutting are shown in Figure 3.16 (a) (b) and 3.17 (a) (b).

We take just 180 sampling points each for F_x and F_y from one cycle of the rotation of the spindle. We make the assumption that the force signals are repeated at the spindle period. The data from one revolution are therefore sufficient for us to identify the force coefficients.
Figure 3.18 (a) (b) and 3.19 (a) (b) show the measured X and Y force component data for one revolution and their Fast Fourier Transform (FFT).

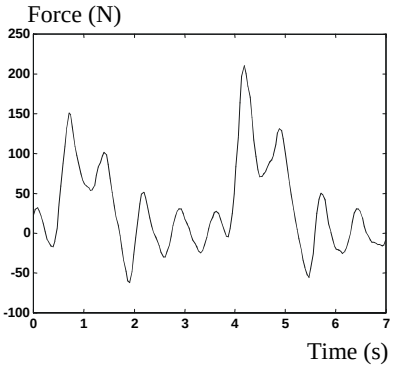

Figure 3.18 (a): X-axis force in the time domain for 1 revolution

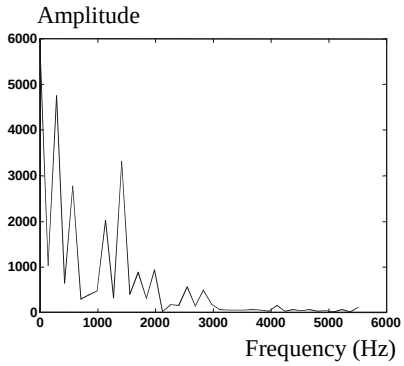

Figure 3.18 (b): X-axis force in the frequency domain for 1 revolution

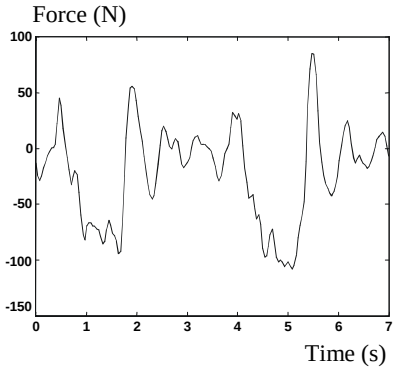

Figure 3.19 (a): Y-axis force in the time domain for 1 revolution

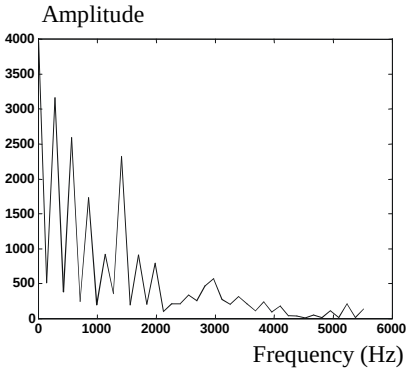

Figure 3.19 (b): Y-axis force in the frequency domain for 1 revolution

The position angle α can be discretised with an increment of 2 degree in correspondence with the 180 sampling points.
The engagement matrix $\boldsymbol{U}$ defined by equation (10) is expressed as functions of position angle α, which is function of time t.
By taking Fourier transform of the elements (u_{ij}, i, j=1, 2) of the matrix $\boldsymbol{U}$, we can equivalently define the engagement matrix in the frequency domain.
The ball-end mill used in this tests has 2 teeth. We chose the FFT rectangular window to coincide with the period of 1 spindle revolution. 180 points were sampled per revolution.
The fundamental harmonics is at the spindle frequency. The second harmonics is at the tooth passing frequency. The second and fourth harmonics of the force signals in the frequency domain thereby correspond to the first and second harmonics (i.e. at the frequencies ω_0 and ω_1), respectively.

Taking Fast Fourier transform of the elements (u_{ij}) of the engagement matrix ($\boldsymbol{U}$) (see equation (10)) and substituting the values (see Table 3.2) for the parameters f_z and a_p, we can readily work out the engagement matrix at the first and second tooth passing frequencies. The results are given as follows:

$$\boldsymbol{U}(j\omega_0) = \begin{bmatrix} 0.0471 - 0.6734j & -0.6434 - 0.9062j \\ 0.6434 + 0.9062j & 0.0471 - 0.6734j \end{bmatrix}$$

and

$$\boldsymbol{U}(j\omega_1) = \begin{bmatrix} -0.2840 - 0.0399j & -0.0499 + 0.5709j \\ 0.0499 - 0.5709j & -0.2840 - 0.0399j \end{bmatrix}$$

The harmonics of the measured force signals at the frequency ω_0 and ω_1 can be directly computed from Fast Fourier Transform as

$$\begin{bmatrix} F_{xmes}(j\omega_0) \\ F_{ymes}(j\omega_0) \end{bmatrix} = \begin{bmatrix} -585.8 - 4723.2j \\ 2003.7 + 2451.4j \end{bmatrix}$$

and

$$\begin{bmatrix} F_{xmes}(j\omega_1) \\ F_{ymes}(j\omega_1) \end{bmatrix} = \begin{bmatrix} -2701.1 + 657.8j \\ 623.6 - 2517.0j \end{bmatrix}$$

After substituting the above results into equations (3) and (4), we can get the absolute values of the dynamic noise signals F_{xnos} and F_{ynos} as functions of the force coefficients k_t and k_r.

From equation (5) and (6), the values of these two coefficients can be worked out. The results are k_t=3844 N/mm^2 and k_r=2052 N/mm^2.

This calculation is based on the assumption that the force component signals are exactly repeated at the spindle period.
In reality, the force component signals measured are not exactly periodic at the spindle period. The signals are also not periodic at the tooth period due to many factors such as tooth run-out, periodic vibrations, and so on.
The spectrum of the measured force signals in the frequency domain by using different window lengths are thereby not identical to each other.
The X and Y force components can be easily calculated by using equation (1) with the known values of k_t and k_r as well as the engagement matrix ***U*** (see equation (10)).

Figure 3.20 and Figure 3.21 show the directly measured force components (solid curves) and the calculated ones (dashed curves) by using the identified force coefficients k_t and k_r.

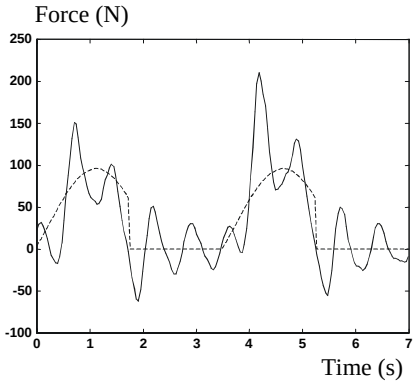

Figure 3.20: The measured X-axis force (solid curve) and the calculated one (dash curve) using the identified force coefficient values

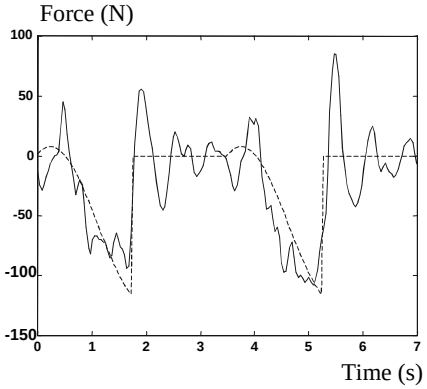

Figure 3.21: The measured Y-axis force (solid curve) and the calculated one (dash curve) using the identified force coefficient values

3.6 Force Prediction in 5-axis milling with a helical-fluted Cutter

The method of identification of force coefficients in section 3.5 is based on the assumption that the cutting force can be modelled by a linear force model (see section 3.5 the definition of engagement matrix) and the cutter used has a negligible helical angle. In this section, the cutting force is predicted by using O. Kienzle's force formula (see section 3.2.2) in 5-axis milling with a helical fluted ball end mill. Due to the complexity of the tool geometry, several steps are needed to obtain the total instantaneous cutting force.
Firstly, a geometric model of the helical fluted ball end mill is developed. Secondly, operation geometry, i.e., the entrance/exit angle, is defined based on the established geometric model. Thirdly, the three force components (tangential, radial, and axial forces) on a small incremental element of cutting edge are locally computed from the O. Kienzle's force formula and their relations. After transforming the force values expressed in the local system into the global system, the total force is finally obtained by the integration along the active cutting edge segment and the summation for all teeth.

3.6.1 Geometric Model of a Helical Fluted Ball-Nose

Ball-nose's geometry is shown in figure3.22. A helical cutting edge BO_1P on the semi-sphere (center O' and radius $O'P=R_0$ normal to plane PMN) of the ball part has its projection PHN (H is O_1's projection), which is

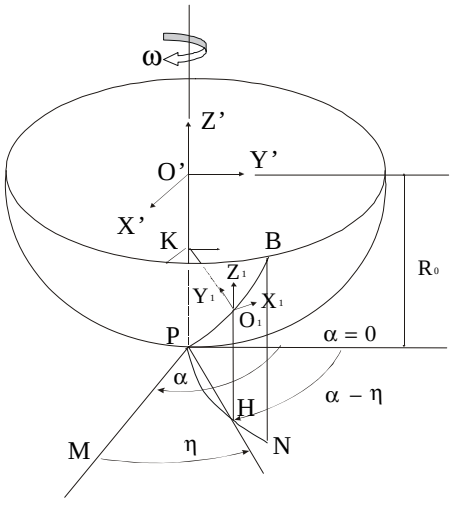

Figure 3.22: A geometric model of a ball nose

tangential to a reference line PM in the plane. O'-X'Y'Z' is a Newton inertia Cartesian system. O_1-$X_1Y_1Z_1$ is a local rectangular system with its origin (O_1) fixed on BO_1P, its bottom plane (X_1-Y_1) paralleled to PMN, and axis (Y_1) perpendicularly intersecting O'P at K. If the reference line PM fixed with cutter at tip P rotates from angular position α=0 to α in O'-X'Y'Z' system, then gyration radius KO_1 with the lag angle of η relative to PM must have a position angle of $\alpha - \eta$ in the same system.

Considering right triangle O'KO_1, we have

$$R_0^2 = O'K^2 + KO_1^2 = (R_0 - O_1H)^2 + R^2 \quad (KO_1=R,\ O'O_1=R_0) \qquad (1)$$

For a typical-formed ball-nose mill its helix pitch keeps constant but its helix angle reduces gradually from maximum value (β_0) at point B to zero at tip P along BO_1P, and furthermore lift O_1H is determined by the values of β_0, R_0, and η, as shown in figure 3.23.

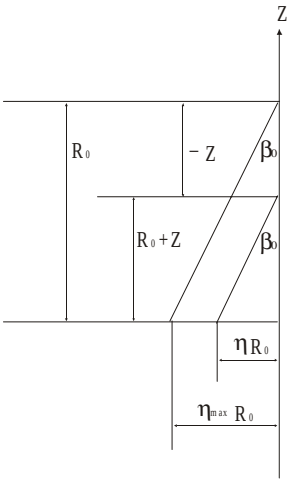

Figure 3.23: A Geometric relationship between lift and helix angle

$$O_1H = R_0 + Z = \eta \cdot R_0 \cdot \cot\beta_0 \qquad (2)$$

Combining (1) and (2), solving for R, we obtain

$$R = R_0 \cdot \sqrt{1-(1-\eta \cdot \cot\beta_0)^2} \qquad (3)$$

From equations (2) and (3), taking position angle $\alpha - \eta$ into account, Point O_1's coordinates in O'-X'Y'Z' therefore can be easily written as

$$\overrightarrow{O'O_1} = \begin{bmatrix} X' \\ Y' \\ Z' \end{bmatrix} = \begin{bmatrix} R \cdot \sin(\alpha-\eta) \\ R \cdot \cos(\alpha-\eta) \\ \eta \cdot R_0 \cdot \cot\beta_0 - R_0 \end{bmatrix}$$

$$= \begin{bmatrix} R_0 \cdot \sqrt{1-(1-\eta \cdot \cot\beta_0)^2}\,\sin(\alpha-\eta) \\ R_0 \cdot \sqrt{1-(1-\eta \cdot \cot\beta_0)^2}\,\cos(\alpha-\eta) \\ R_0(\eta \cdot \cot\beta_0 - 1) \end{bmatrix}$$

3.6.2 Operation Geometry – Entrance/Exit Angle

Boundary curve-dependent entrance/exit angles, measured in reference to Y-axis of a global static system O-XYZ, indicate the starting/finishing of active cutting along each circle (i.e. circle parallel to XY-plane). During one revolution gradually engaged different zones of tool edges cut off a ball-shaped workpiece profile bounded by three curves AB, BE and AE, as shown in figure 3.24.

If the top surface of the workpiece is flat, both AB and BE are arcs of the circles that have center [0 0 -(R_0-a_p)] and radius $\sqrt{R_0^2-(R_0-a_p)^2}$; [0 0 0] and R_0 respectively. However AE is part of the intersection between the semi-sphere and the cylindrical surface created from the last previous tool path. It is worth noting that the cylindrical surface is an idealized model. In fact there exist scallops in the feed direction besides in the X direction. Based on the above discussion AB, BE and AE's equations in O-XYZ are identified with

$$\text{AB: } \begin{cases} X_{AB}^2 + Y_{AB}^2 = R_0^2 - Z_{AB}^2 \\ Z_{AB} = -(R_0 - a_p) \end{cases}$$

$$\text{BE: } \begin{cases} X_{BE}^2 + Z_{BE}^2 = R_0^2 \\ Y_{BE} = 0 \end{cases}$$

$$\text{AE: } \begin{cases} X_{AE}^2 + Y_{AE}^2 + Z_{AE}^2 = R_0^2 \\ (X_{AE} - a_e)^2 + Z_{AE}^2 = R_0^2 \\ Y_{AE} = t \ \text{(parameter)} \end{cases}$$

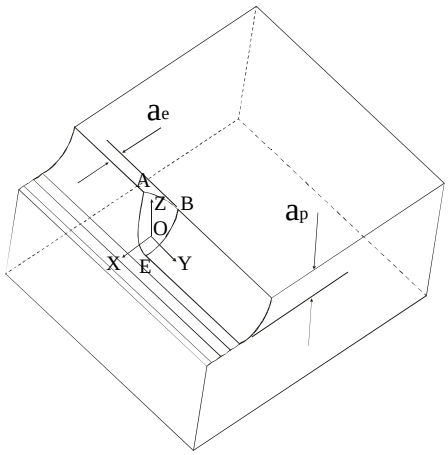

Figure 3.24: A geometric model of the ball end mill engagement

And also boundary points A, B, and E's coordinates are

$$\text{Point A: } \begin{bmatrix} -(R-a_e) \\ -\sqrt{R^2-(R-a_e)^2} \\ -(R_0-a_p) \end{bmatrix}$$

$$\text{Point B: } \begin{bmatrix} -R \\ 0 \\ -(R_0-a_p) \end{bmatrix}, \qquad \text{Point E: } \begin{bmatrix} 0 \\ 0 \\ -\sqrt{R_0^2-(1/4)\cdot a_e^2} \end{bmatrix}$$

Assuming that the cutter is inclined both in and perpendicular to the feed direction with the lead and tilt angles of δ_f and δ_n, respectively, the transformation matrix from system O'-X'Y'Z' to system O-XYZ is

$$T_{o'-o}=\begin{bmatrix} \cos\delta_f & \sin\delta_f \cdot \sin\delta_n & -\sin\delta_f \cdot \cos\delta_n \\ 0 & \cos\delta_n & \sin\delta_n \\ \sin\delta_f & -\cos\delta_f \cdot \sin\delta_n & \cos\delta_f \cdot \cos\delta_n \end{bmatrix}$$

So the above boundary curve equations, as well as points A, B, and E's coordinates in O-XYZ can be expressed in the O'-X'Y'Z' system through this transformation matrix. By substituting cutting edge's Z'-axis coordinate-- $R_0(\eta \cdot \cot\beta_0 - 1)$ --for the Z' values in the boundary curve equations written in O'-X'Y'Z' system, after some manipulations we can figure out Y'-axis coordinates on curves AB, BE, and AE. Similarly by equalizing the Z' values between cutting edge's and intersections' (i.e. points A, B, and E), three critical values of η corresponding to A, B, and E, are found. The entrance/exit angles as a result can immediately be calculated as $2k\pi + \cos^{-1}(Y'/R)$ according to the different ranges of η.

3.6.3 Force Prediction

For a finite element of the cutting edge its length is

$$b = \sqrt{dX^2 + dY^2 + dZ^2}$$

Differentiating $\overrightarrow{O'O_1}$ and substituting into the above equation, thus

$$b = \sqrt{R_0^{\,2} \cdot [1-(1-\eta \cdot \cot\beta_0)^2] + R_0^{\,2} \cdot \cot^2\beta_0 + \frac{R_0^{\,2} \cdot \cot^2\beta_0 \cdot (1-\eta \cdot \cot\beta_0)^2}{1-(1-\eta \cdot \cot\beta_0)^2}} \cdot d\eta$$

After transforming the feed vector per tooth $\left[\overrightarrow{f_Z}\right]_{O'}$ in O-XYZ into the O'-X'Y'Z' system, namely, $\left[\overrightarrow{f_Z}\right]_{O'} = [T_{O'-O}]^{-1} \left[\overrightarrow{f_Z}\right]_{O}$ the thickness of cut (h) can be readily approximated by projecting $\left[\overrightarrow{f_Z}\right]_{O'}$ onto vector $\left[\overrightarrow{OO_1}\right]_{O'}$, or

$$h = \left| f_z \cdot \frac{\left(\left[\overrightarrow{OO_1}\right]_{O'} \cdot \left[\overrightarrow{f_z}\right]_{O'}\right)}{\left|\overrightarrow{OO_1}\right| \cdot f_z} \right| = \left| \frac{\left(\left[\overrightarrow{OO_1}\right]_{O'} \cdot \left[\overrightarrow{f_z}\right]_{O'}\right)}{R_0} \right|$$

The magnitude of the instantaneous tangential force on the element b is determined by $F_c = k_{c1.1} \cdot b \cdot h^{1-m_c}$, and its direction coincides with the X_1-axis (refer to figure 3.22). The magnitudes of the related radial and axial forces are computed from the equations: $F_r = K_r \cdot F_c$ and $F_a = K_a \cdot F_c$ (K_r and K_a are constants). Their directions are along the Y_1 and Z_1 axes, respectively.
The transformation matrix from O_1-$X_1Y_1Z_1$ to O'-X'Y'Z' is given by

$$T_{O_1-O'} = \begin{bmatrix} -\cos(\alpha-\eta) & -\sin(\alpha-\eta) & 0 \\ \sin(\alpha-\eta) & -\cos(\alpha-\eta) & 0 \\ 0 & 0 & 1 \end{bmatrix}$$

The force vector in O-XYZ is therefore equal to

$$\begin{aligned} \overrightarrow{F_G} &= T_{O'-O} \cdot T_{O_1-O'} \cdot \overrightarrow{F_L} \\ &= T_{O'-O} \cdot T_{O_1-O'} \cdot \begin{bmatrix} F_c \\ F_r \\ F_a \end{bmatrix} = F_c \cdot T_{O'-O} \cdot T_{O_1-O'} \cdot \begin{bmatrix} 1 \\ K_r \\ K_a \end{bmatrix} \cdot \\ &= k_{c1.1} \cdot b \cdot h^{1-m_c} \cdot T_{O'-O} \cdot T_{O_1-O'} \cdot \begin{bmatrix} 1 \\ K_r \\ K_a \end{bmatrix} \end{aligned}$$

Now three force components in O-XYZ have been worked out for a small element of the cutting edge. Provided that the rotation angle (α_n) and the location angle (η_n) of the n^{th} tooth are equally spaced, the total force components therefore are found out by integrating and summing $\overrightarrow{F_G}$ for all the active edge segments, or mathematically

$$\overrightarrow{F_{TG}} = \sum_{n=1}^{Z} \cdot \sum_{j=1}^{J} \cdot G \cdot \overrightarrow{F_G}$$

Where:

$$G = \begin{cases} 1 & (\alpha_n - \eta_n \subseteq [2k\pi + \alpha_{ent.},\ \ 2k\pi + \alpha_{ex.}]) \\ 0 & (\text{else}) \end{cases}$$

Z: tooth number of the cutter.
J: element number of the active edge within the range of $[0, \eta_{max}]$.
The angles $\alpha_{ent.}$ and $\alpha_{ex.}$ are calculated as given in section 3.6.2.

3.6.4 Experimental Verification

In the experiment, a helical ball end mill is used. Its nose radius is 5 mm; maximum helix angle is 40^0; number of teeth is 2. Type of workpiece material is steel (C45 HRC 23). Values of force coefficients are $k_{c1.1}$=1765 N/mm^2 and K_a=0.15, K_r=0.4. The value of material index is m_c=0.25. Inclination angles of the tool with respect to the workpiece are δ_f=0 and δ_n=0.

Cutting parameters are depth of cut: a_p=2 mm; width of cut: a_e=5 mm; spindle speed: n=3187 rpm. Cutting Speed: v_c=100 m/min; feed rate: is v_f=127 mm/min; feed /tooth: f_z=0.02mm.

The milling tests were conducted on a 3-axis high-speed machine tool (Matsuura FX-5G)). The total X and Y axis forces (F_x and F_y) in the global system O'-X'Y'Z' (see Figure 3.22) were measured by a KISTLER dynamometer (type 9265B) together with a clamping plate (type 9443B).

A KISTLER charge amplifier 5017A and a Dynamic Signal Analyzer DSA200 with Difa Transfer and Control software D-TAC are employed for the data acquisition. Sampling frequency is 12.8 kHz. The cut-off frequencies of the low pass filters inside the charge amplifier device were all set to 6.4 kHz (refer to Figure 3.3 in section 3.4 for the experimental set-up of the tests).

The predicted and measured instantaneous X-axis and Y-axis forces are given as follows (see a MatLab program in Appendix A):

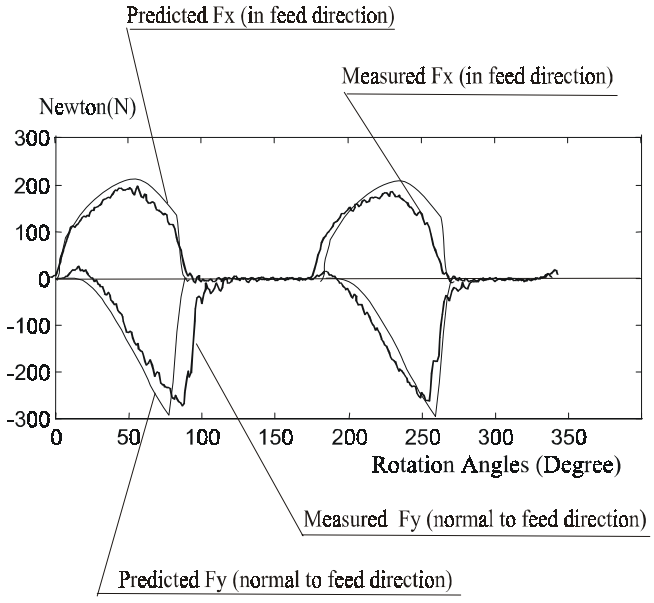

Figure 3.25: A comparison of predicted and measured X- and Y- axis forces

3.7 Analysis of Specific Cutting Forces at Different Cutting/Spindle Speeds

The force model used in the section 3.6 is the O. Kienzle's force formula, which has an exponential form, i.e. the force coefficient k_c in this model is function of the cut thickness. This exponential form is powerful for cutting force prediction, but a simple linear form of it is easier to manipulate than the exponential one if we use it in the coupling equations of process and structural dynamics to predict chatter.

Two questions thus need further clarification or investigation. Does the specific cutting force change with chip thickness in milling as it happens in turning? Does the specific cutting force still remain constant when increasing cutting speed? The experimental results showed that the specific cutting force in milling remains almost constant over a wide range of engagement values (cut thickness), except at material entry. The specific force varies at different cutting speeds.

The cutting speeds used in the tests are 15, 30, 80, 160, and 214 m/min and the corresponding spindle speeds are 598, 1196, 3187, 6373, and 8486 rpm, respectively. The instantaneous force components were measured by the KISTLER dynamometer in the feed and normal to the feed directions, i.e., F_x and F_y components (refer to Figure 3.3 in section 3.4 for the experimental set up and Figure 3.10 in section 3.5 for a schematic presentation of milling operation).

At low cutting speeds (15 m/min and 30 m/min), the measured force component signals are not distorted by vibration noise as shown in Figure 3.26 and Figure 3.27 (thick curve).
These force data can be directly used for the identification of the specific forces. The tangential and radial force components F_t and F_r (also refer to Figure 3.10 in section 3.5) were readily computed by doing some mathematical transformations from the global system (F_x and F_y axes) into the local one (F_t and F_r axes), as shown in Figure 3.28.
The specific cutting forces in the tangential and radial directions versus rotation angles of the tool are shown in Figure 3.29.

The result proves that at a low cutting speed, the specific forces k_t and k_r remain almost constant over a wide range of engagement values (cut thickness) except at the material entry. Based on this investigation, we can use the linear or simplified form of the O. Kienzle's force formula to analyze the instability of the cutting process for milling operation, as done in the model developed in section 3.5. This justifies the use of such

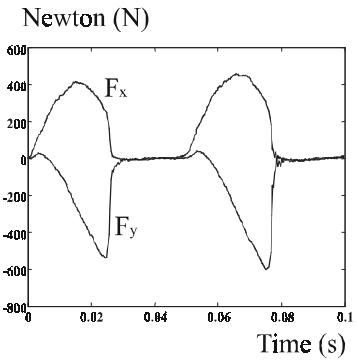

Figure 3.26: the measured X-and Y-axis forces at cutting speed of 15 m/min.

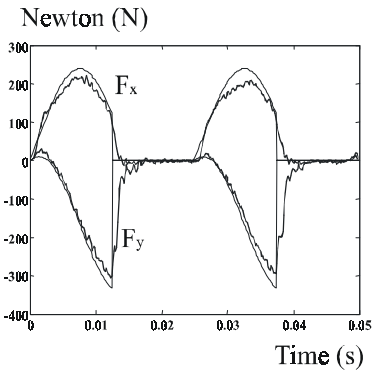

Figure 3.27: the measured (thick curve) and predicted (thin one) X- and Y- axis forces at cutting speed of 30 m/min

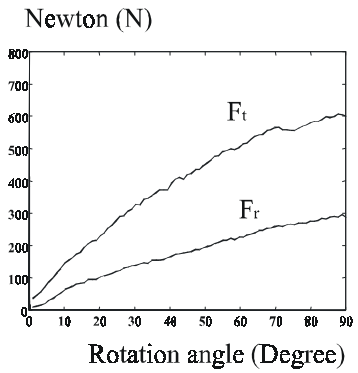

Figure 3.28: The tangential and radial cutting forces at cutting speed of 15 m/min for different position angles

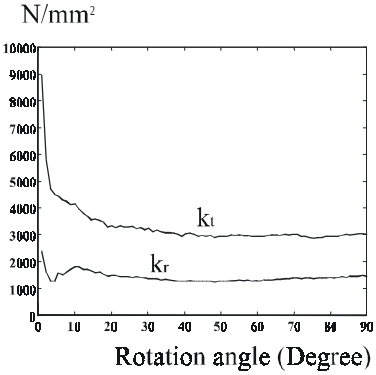

Figure 3.29:The tangential and radial specific cutting forces at cutting speed of 15 m/min for different position angles

simplified model to calculate stable cutting forces or specific cutting force coefficients.

In relatively high speed milling, however, a strong impact is induced while the tool enters the work-piece material, especially for milling hard material.

The force signals are significantly deteriorated by dynamic noise, as shown in Figure 3.30, Figure 3.31, and Figure 3.32 at speeds of 80, 160, and 214 m/min, respectively, by thick solid curves.

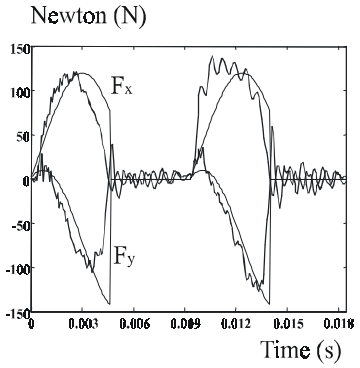

Figure 3.30: The measured (thick curve) and predicted (thin one) X-and Y-axis forces at cutting speed of 80 m/min.

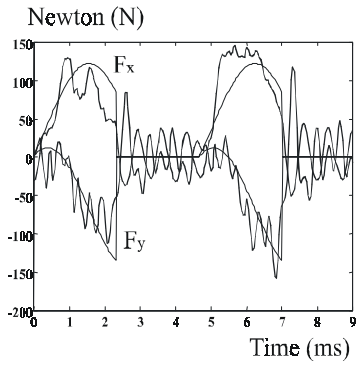

Figure 3.31: The measured (thick curve) and predicted (thin one) X-and Y-axis forces at cutting speed of 160 m/min

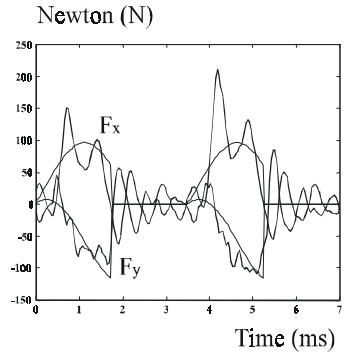

Figure 3.32: The measured (thick curve) and predicted (thin one) X-and Y-axis forces at cutting speed of 214 m/min

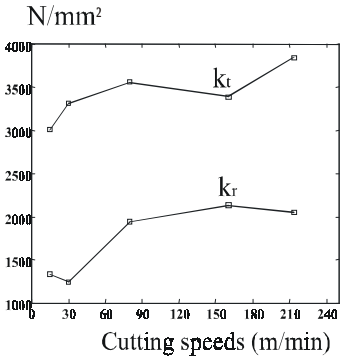

Figure 3.33: The tangential and radial specific cutting forces at different cutting speeds

The method to pick out the stable cutting force signals (see also Figure 3.30, Figure 3.31, and Figure 3.32 by thin solid curves) from the noised measurement signals has been given in section 3.5.

Figure 3.33 shows the calculated results of the specific tangential and radial forces (k_t and k_r) for different cutting speeds. From the k_t and k_r values (see Figure 3.33), it is obvious that the specific tangential and radial cutting forces are not constant for different cutting speeds.

3.8 Summary

In high speed milling, strong impact takes place when the tool enters/exits the workpiece material due to the high cutting/rotation speeds.
The cutting force contains high harmonic components, which are in the neighbourhood of the dynamometer's natural frequencies. These high frequency harmonic excitations make the milling system vibrate at and/or near the resonance frequencies of the dynamometer and thus result in dynamic noise in force measurement.
If these high frequencies are filtered out with a low pass filter, the cutting force signals may also be significantly filtered out together with the dynamic noises. To measure and evaluate high-speed milling force, the dynamics of the dynamometer have to be taken into account.

In this chapter, the basics of force measurement and the influences of the dynamics of the dynamometer on the measured force signals have been discussed in detail.
A force compensation method is illustrated to compensate for the dynamic effects of the dynamometer on the measured force output.
A strategy for identification of specific forces in high-speed milling is developed based on the directly measured noise signals from a dynamometer. The force model employed in this strategy uses a simplified O. Kienzle's force formula, i.e. a linear form.
Force prediction for 5-axis milling with complicated tool geometry is described also in this chapter.
In addition, experimental study of the specific cutting forces in milling has proved that a simplified O. Kienzle's force formula can be used to model the instantaneous cutting forces over a wide range of engagement values (cut thickness), except at material entry. This is helpful for analyzing the system instability, as will be discussed in Chapter 4 ("Chatter in High Speed Milling").

Chapter 4

Chatter in High Speed Milling

4.1 Introduction

The cutting force discussed in Chapter 3 is a theoretical/stable force. Its dynamic component (variation) can be traced back to forced vibrations of some structural elements (machine, dynamometer, …). The structure's response is a steady state response. Any transient vibration of the structure decays exponentially.

In an unstable or "chatter" case, the amplitude of the structure's response increases, and at the limit of stability the magnitude of the vibration remains constant.

Whether or not chatter occurs depends on the closed-loop characteristic equation of the structural and process dynamics, i.e., the impulse response of the coupling system.

The focus of this chapter is on the structure's transient response during cutting. Some of the important concepts in the theory of structural dynamics are first briefly reviewed. The measured frequency response function (FRF) of the tool/tool-holder/spindle assembly given in this chapter helps readers have a general feeling of the impulse response of the high-speed milling machine structure.

The influence of tool holders on tool wear and part surface roughness in high-speed milling of hard steel was experimentally investigated and explained by the effect of transient vibration on the cutting process.

Chatter in high-speed milling is studied both, in an experimental and analytical way. A technique for chatter detection in high-speed milling is suggested. A lot of tests have been done to study the influences of the cutting parameters on chatter. Some of the test results in high-speed milling of aluminium/steel are presented and discussed.

Analytical prediction of chatter is described in detail in this chapter and verified in high-speed milling of aluminium for a single and multiple degree-of-freedom system. Finally, a strategy for selection of optimal spindle speed to avoid chatter is developed and experimentally justified for high-speed milling of aluminium.

4.2 Structural Dynamics Fundamentals and Frequency Response of the High-Speed Milling Machine Structure – Tool/Tool-holder/Spindle Assembly

Some basic and important concepts and equations of the structural dynamics, which will be used in the following sections, are overviewed here with the discussion of a single/multiple degree-of-freedom system.

4.2.1 A Single-Degree-of-Freedom System

A viscously damped single degree of freedom system model is shown in Figure 4.1. It is well known that the governing equation of its dynamics is

$$M\ddot{x}(t) + C\dot{x}(t) + Kx(t) = f(t) \qquad (4.1)$$

Where:
M: the mass
C: the damping
K: the stiffness
$\ddot{x}$: the acceleration
$\dot{x}$: the velocity
x: the response displacement
t: the time variable
f(t): the external force.

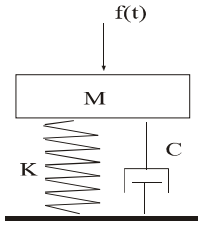

Figure 4.1: A spring-damper-mass model for a single-degree-of-freedom system

Or equivalently with Laplace variable (s):

$$X(s) = H(s)F(s) \qquad \text{with} \quad H(s) = 1/(Ms^2 + Cs + K)$$

H(s) is called *transfer function*. The system's characteristic equation is

$$Ms^2 + Cs + K = 0$$

The solutions to this equation give the system's *poles* as

$$s_{1,2} = -C/(2M) \pm \sqrt{[C/(2M)]^2 - (K/M)} \qquad (4.2)$$

In equation (4.2), we notice that when $C = 2\sqrt{MK}$,

$$[C/(2M)]^2 - (K/M) = 0.$$

Let the *damping ratio* $\xi = C/C_c$ ($C_c = 2\sqrt{MK}$),
So, If ξ=1, the system is *critical damped*. If ξ>1, the system is *over damped*. If ξ=0, there is no damping, and $s_{1,2} = \pm j\sqrt{(K/M)} = \pm j\omega_n$. ω_n is called the *un-damped natural frequency*. If 0<ξ<1, the system is *under damped*, then $s_{1,2} = -\xi\omega_n \pm j\omega_r$ ($\omega_r = \omega_n\sqrt{1-\xi^2}$). $-\xi\omega_n$ is called the *damping factor* and ω_r is called the *damped natural frequency*.

The solution to the *homogeneous* system equation (4.1) gives

$$x(t) = x_1 e^{s_1 t} + x_2 e^{s_2 t}$$

Where: x_1 and x_2 are initial condition dependent constants.

For an un-damping system (ξ=0) with initial displacement (X_0) and velocity (V_0), the system's response x(t) is sinusoidal with constant amplitude:

$$x(t) = \sqrt{X_0^2 + (V_0/\omega_n)^2}\,\sin(\omega_n t + \alpha) \qquad (\alpha = \tan^{-1}(X_0\omega_n/V_0))$$

For an under-damped system (0<ξ<1), the impact response x(t) of the system is sinusoidal but its amplitude decays in the time domain.

For a Dirac impulse response, the response x(t) can be calculated from the inverse Laplace transformation as

$$h(t) = H^{-1}(s) = \left(\frac{1/(j2M\omega_r)}{s - s_1} + \frac{-1/(j2M\omega_r)}{s - s_2}\right)^{-1}$$

The terms $1/(j2M\omega_r)$ and $-1/(j2M\omega_r)$ are called *residues*, which define the initial amplitude. They are a pair of conjugates.

By replacing s (=jω), after some simple manipulation the transfer function H(s) can be expressed in terms of K, ξ and ω_n as

$$H(j\omega) = \omega_n{}^2 /[(\omega_n{}^2 - \omega^2 + j2\xi\omega_n\omega)K]$$

H(jω) is called *frequency response function (FRF).*

The real part (Re) and imaginary part (Im) of H(jω) can be found as

$$\mathrm{Re} = \frac{1-(\omega/\omega_n)^2}{\left[1-(\omega/\omega_n)^2\right]^2 + 4\xi^2(\omega/\omega_n)^2} \cdot \frac{1}{K}$$

$$\mathrm{Im} = -\frac{2\xi(\omega/\omega_n)}{\left[1-(\omega/\omega_n)^2\right]^2 + 4\xi^2(\omega/\omega_n)^2} \cdot \frac{1}{K}$$

All these basic concepts for a single degree-of-freedom system can naturally be extended to a multiple degree-of-freedom system.

4.2.2 A Multiple-Degree-of Freedom System

A viscously damped two-degree-of-freedom system model is shown in Figure 4.2. The equations of motion of the system are

$$M_1\ddot{x}_1(t) + (C_1 + C_2)\dot{x}_1(t) - C_2\dot{x}_2(t) + (K_1 + K_2)x_1(t) - K_2x_2(t) = f_1(t)$$
$$M_2\ddot{x}_2(t) + C_2\dot{x}_2(t) - C_2\dot{x}_1(t) + K_2x_2(t) - K_2x_1(t) = f_2(t)$$

Or in matrix notation (after deleting t)

$$\begin{bmatrix} M_1 & 0 \\ 0 & M_2 \end{bmatrix}\begin{Bmatrix} \ddot{x}_1 \\ \ddot{x}_2 \end{Bmatrix} + \begin{bmatrix} C_1+C_2 & -C_2 \\ -C_2 & C_2 \end{bmatrix}\begin{Bmatrix} \dot{x}_1 \\ \dot{x}_2 \end{Bmatrix} + \begin{bmatrix} K_1+K_2 & -K_2 \\ -K_2 & K_2 \end{bmatrix}\begin{Bmatrix} x_1 \\ x_2 \end{Bmatrix} = \begin{Bmatrix} f_1 \\ f_2 \end{Bmatrix}$$

The dynamic equations of a multiple degree-of-freedom system can generally be written as

$$[M]\{\ddot{x}\} + [C]\cdot\{\dot{x}\} + [K]\cdot\{x\} = \{f\}$$

Where:
[M]: the mass matrix
[C]: the damping matrix
[K]: the stiffness matrix
$\{\ddot{x}\}$: the acceleration vector
$\{\dot{x}\}$: the velocity vector
$\{x\}$: the response vector
{f}: the external forcing vector

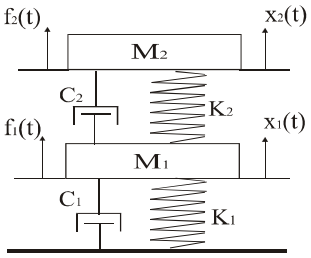

Figure 4.2: A spring-damper-mass model for a two degrees of freedom system

Or

$$\{x(s)\} = [H(s)] \cdot \{f(s)\} \qquad \text{with} \qquad [H(s)] = ([M]s^2 + [C]s + [K])^{-1}$$

[H(s)] is called the *transfer function matrix*.

The system characteristic equation is the determinant of the dynamic stiffness matrix, i.e.

$$\det([M]s^2 + [C]s + [K]) = 0$$

The roots of this equation give the system's poles.

For each pole (s_r), we have the following simultaneous equations:

$$([M]s_r^{\,2} + [C]s_r + [K])\{x\} = \{0\}$$

A non-zero solution {x} of the simultaneous equations defines a *modal vector or mode shape vector.*
From the basic theory of linear algebra, the inverse of a matrix can be calculated from its ad-joint matrix and determinant. Thus [H(s)] can be further expressed as

$$[H(s)] = \frac{\text{adj}([M]s^2 + [C]s + [K])}{\det([M]s^2 + [C]s + [K])}$$

By applying the partial fraction expansion, we obtain

$$[H(s)] = \sum_{r=1}^{N} \left(\frac{[A]_r}{(s - s_r)} + \frac{[A]_r^*}{(s - s_r^*)} \right)$$

Where:
s_r: the pole of the system, i.e., $s_r = -\xi\omega_n + j\omega_r$.
s_r^*: the conjugate of s_r, $s_r^* = -\xi\omega_n - j\omega_r$.
$[A]_r$: the *residue matrix*.
$[A]^*_r$: the conjugate matrix of the *residue matrix* $[A]_r$.

The transfer function matrix thus has the form:

$$[H(j\omega)] = \sum_{r=1}^{N}\left(\frac{[A]_r}{(j\omega - s_r)} + \frac{[A]_r^*}{(j\omega - s_r^*)}\right)$$

$[H(j\omega)]$ is called *the frequency response function matrix*.
Each element of $[H(j\omega)]$ is called *the frequency response function*.

Therefore the frequency response function (FRF) can be interpreted as the sum of a number of components, each equivalent to the response of a single-degree-of-freedom system.

4.2.3 The FRF Measurement of the High-Speed Milling Structure – the Tool/Tool-Holder/Spindle

The experimental set-up of the FRF measurement is schematically shown in Figure 4.3. Two accelerometers (a_x and a_y) (Type: PCB, 303A) were used to measure the X- and Y-axis response upon hammer (type: PC, 208/C03) excitation along the X-axis direction. The tool holder (Type: Tribos, Shunk) together with a ball end mill (Type: PWZH8074118 TAX) was connected to the spindle with a draw bar force.

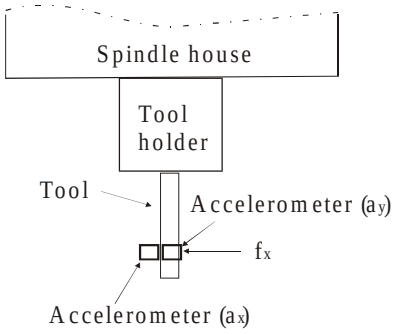

Figure 4.3: Experimental set-up for the FRF measurement of the tool/tool-holder/spindle assembly

The diameter of the tool is 10 mm. The number of teeth is 2. The overhang is 40 mm.
The device DSA200 (Dynamic Signal Analyser series 200) with D-TAC (Difa Transfer And Control) software was used for data acquisition. The low pass filter inside the DSA200 is set to 12.8 kHz. Sampling Frequency is 102.4 kHz. A total of 4096 points were sampled in this measurement.

The measured hammer excitation force (f_x) and acceleration response (a_x and a_y) are shown in Figure 4.4 (a) ~ Figure 4.6 (a) in the time domain and Figure 4.4 (b) ~ Figure 4.6 (b) in the frequency domain.

The frequency response functions (x/f_x and x/f_x) together with their real and imaginary parts are given in Figure 4.7 (a) ~ (c) and Fig. 4.8 (a) ~ (c).

From Figure 4.7 (c) or Figure 4.8 (c), we find that in the frequency range of 0 ~ 1.2 kHz, there are two modes at the frequencies of 0.72 and 1.05 kHz. Some modes at the frequencies even higher than 1.05 kHz may also be possible.

In section 4.4, we will see that chatter frequency in high-speed milling can occur at 3 kHz or even above, due to the very high stiffness of the assembly.

However, it is difficult to obtain the very high harmonic components of the FRF by using hammer excitation. To obtain a very high frequency component, say, 3 kHz, we have to make the impact time between the tip of the hammer and the surface of the structure very small, say, in an order of microseconds. This is very difficult or impossible with hammer excitation, which is controlled by a hand.

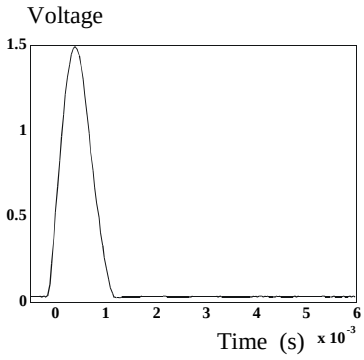

Figure 4.4 (a): Hammer impact force (f) in the time domain

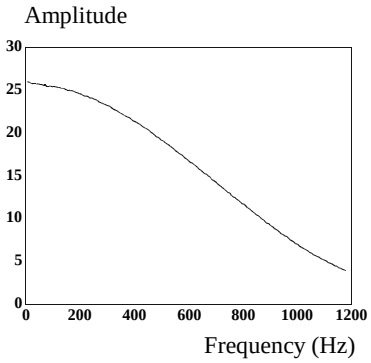

Figure 4.4 (b): Hammer impact force (f) in the frequency domain

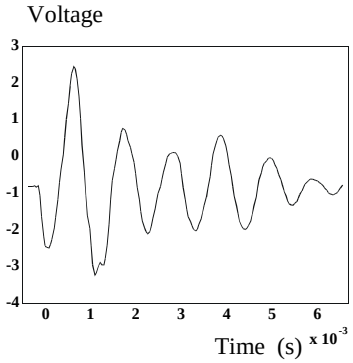

Figure 4.5 (a): X-axis acceleration response (a) in the time domain

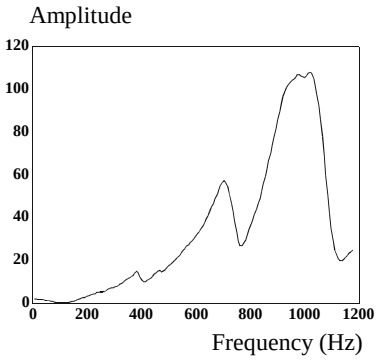

Figure 4.5 (b): X-axis acceleration response(a) in the frequency domain

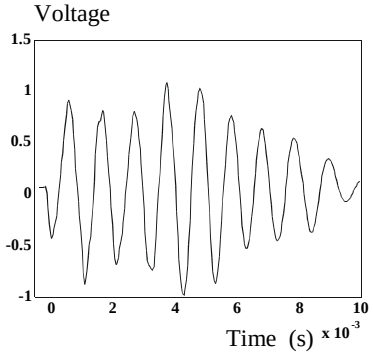

Figure 4.6 (a): Y-axis acceleration response (a) in the time domain

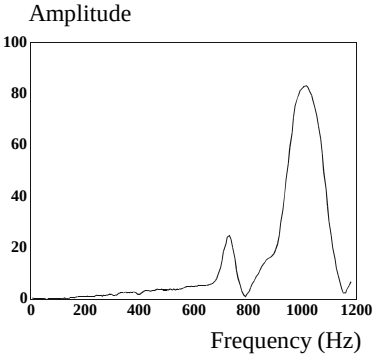

Figure 4.6 (b): Y-axis acceleration response (a) in the frequency domain

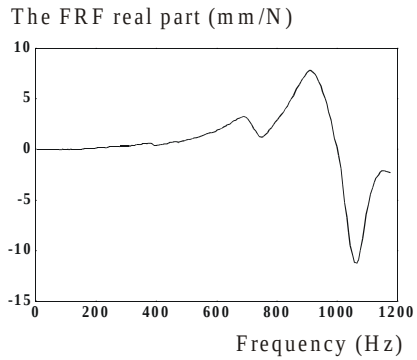

Figure 4.7 (a): The real part of the measured FRF (x/f_x)

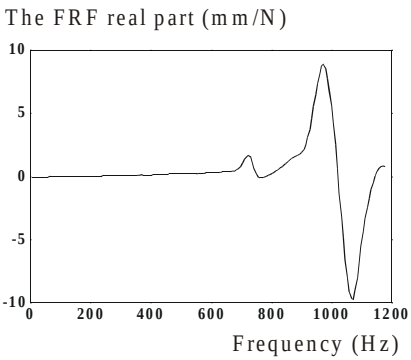

Figure 4.8 (a): The real part of the measured FRF (x/f_x)

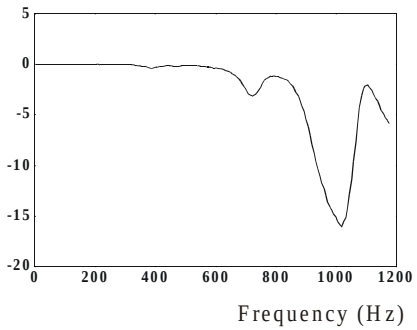

Figure 4.7 (b): The imaginary part of the measured FRF (x/f_x)

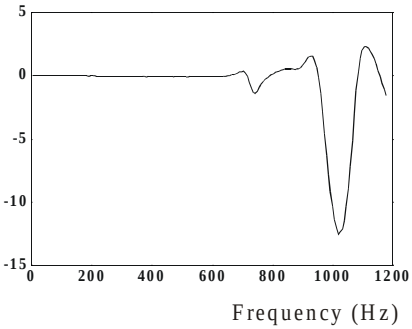

Figure 4.8 (b): The imaginary part of the measured FRF (y/f_x)

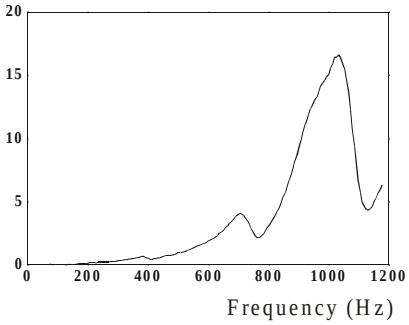

Figure 4.7 (c): The amplitude of the frequency response function (FRF) with hammer impact input (f_x) and X-axis displacement output (x)

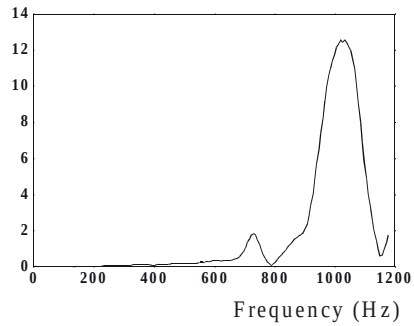

Figure 4.8 (c): The amplitude of the frequency response function (FRF) with hammer impact input (fx) and Y-axis displacement output (y)

4.3 Influence of Transient Vibration on Tool Wear and Part Surface Roughness in High Speed Milling of Hard Steel

4.3.1 Discussion of Effective Clearance Angle in a vibrating Cutting Process

The strong impact in high-speed milling excites the machine structure to vibrate at its dominant mode(s). A schematic presentation of a vibrating slotting operation is shown in Figure 4.9.

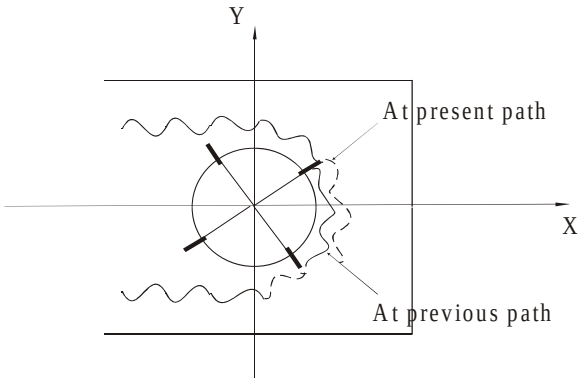

Figure 4.9: A schematic presentation of the dynamic milling operation

The vibration of the tool/tool-holder/spindle assembly relative to the workpiece changes the effective clearance angle of the tool. The variation of clearance angle, especially with a negative angle increases tool wear. The amplitude of the vibration increases part surface roughness.
Figure 4.10 illustrates a vibrating tool at different positions during cutting.

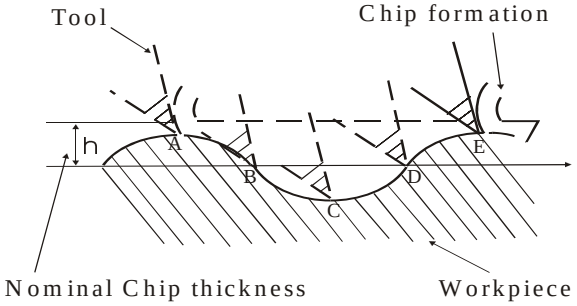

Figure 4.10: The variation of clearance angles due to the vibration of the tool/tool-holder/spindle assembly with respect to the workpiece

The nominal chip thickness value is h. The tool is moving from A to E. The vibration of the tool with respect to the work-piece changes the chip thickness (see the waved curve ABCDE).
When the tool moves downward along curve ABC, the clearance angle decreases first from A to B and takes its minimum value at B (interference may occur depending on the slope of the curve at that point) and then increases from B to C.
When the tool moves upward along curve CDE, the clearance angle increases from C to D and takes its maximum value at position D and then decreases from D to E.

The higher the vibration frequency, the steeper the slope of the vibration curve and the smaller the clearance angle.
A very small clearance angle will increase the friction/interference at the interface of the tool flank and machined surface, and thus will increase tool wear.
The lower the damping of the machine tool structure, the larger the amplitude of the vibration.
The large amplitude of vibration will increase surface roughness.

Even in a stable cutting, transient vibration always occurs. With different type of tool holder, the structure's natural frequency and damping may be different and thus has different transient response.
The transient vibration arising from the intermittent impact of the milling operation, especially in high-speed milling of hard materials, will influence tool wear and surface roughness even if all other conditions are equal.

4.3.2 Observation of Tool Wear and Surface Roughness with Different Types of Tool-Holders in High-Speed Milling of Hard Steel

Several tests have been done to observe tool wear and surface roughness in high-speed milling of hard steel with different types of tool holders.
The tests were conducted on a 3-axis high-speed milling machine Matsuura (Type: FX-5G).
The cutting conditions for all these tests were equal except the type of tool holder used, as listed in Table 4.1.
In each test, the tool flank wear (VB value) and workpiece roughness (R_a value) were measured every 8 minutes of cutting.
The measured results of VB and R_a for Test 1~ Test 5 are shown in Figure 4.11 (a) (b) ~ 4.15 (a) (b), respectively. The cutting processes are all stable. No chatter marks appeared on the workpiece.

From Figure 4.13 (a) (b) to 4.15 (a) (b), we find that the tool life and surface roughness are comparable with each other.
It implies that the transient vibrations at dominant modes with these tool holders are also comparable.
In Figure 4.11 (a) (b), we find that tool life with tool-holder Spantang is much shorter than that with others, but the surface roughness is comparable with the others.
So the dynamic behaviour with tool holder Spantang is significantly different from others.
It means that the natural frequency at dominant mode with tool holder Spantang is much higher than that with others, but the damping is comparable.
Figure 4.12 (a) (b) shows that with tool holder Hydro1, tool life becomes the longest and the mean value of surface roughness is the lowest.
Hence the natural frequency at dominant mode with tool holder Hydro1 is the lowest or its damping is the highest, or both.

So machine structure with high damping and low natural frequency is in favour of tool life and surface smoothness in cutting.

Table 4.1: Machining conditions

	Test 1~Test 5
Tool Holder Types	Test 1: Spantang Test 2: Hydro1 Test 3: Specile Test 4: Hydro2 Test 5: Tribos
Cutting tool	Carbide Ball mill Type: PWZH8074118TAX Diameter: 10(mm) No. of teeth: 2
Work-piece	ORVAR Steel (HRC52)
Fluid	Blaser 2000 (7%)
Spindle speed	n=17,000 (rpm)
Feed/tooth	f_z=0.142 (mm)
Depth of cut	a_p=0.2 (mm)
Pick feed	a_e=0.2 (mm)

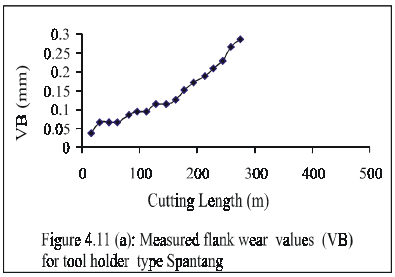

Figure 4.11 (a): Measured flank wear values (VB) for tool holder type Spantang

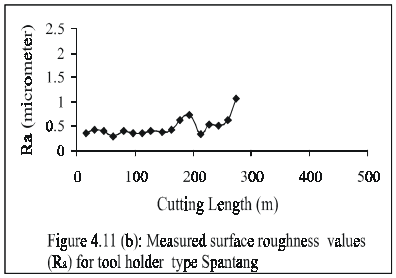

Figure 4.11 (b): Measured surface roughness values (R_a) for tool holder type Spantang

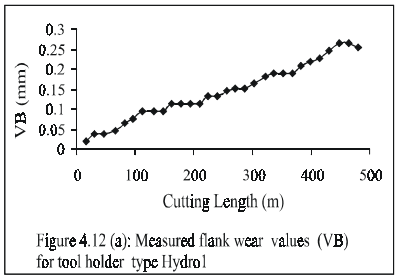

Figure 4.12 (a): Measured flank wear values (VB) for tool holder type Hydro1

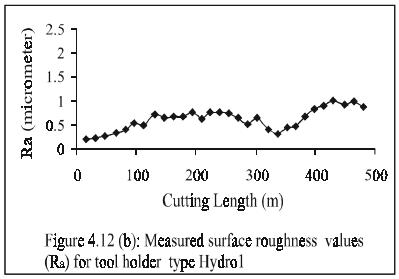

Figure 4.12 (b): Measured surface roughness values (R_a) for tool holder type Hydro1

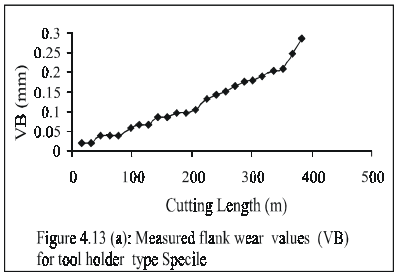

Figure 4.13 (a): Measured flank wear values (VB) for tool holder type Specile

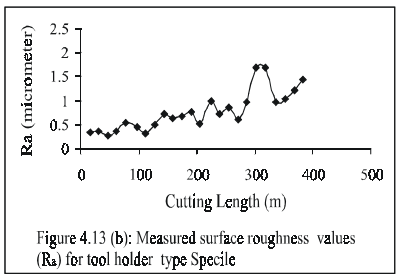

Figure 4.13 (b): Measured surface roughness values (R_a) for tool holder type Specile

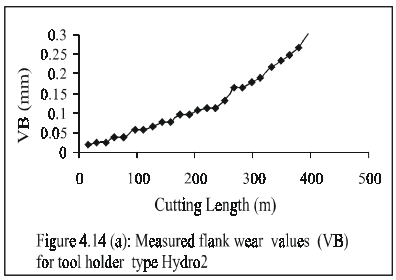

Figure 4.14 (a): Measured flank wear values (VB) for tool holder type Hydro2

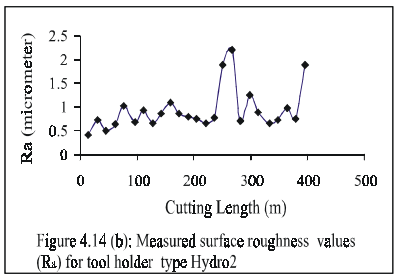

Figure 4.14 (b): Measured surface roughness values (R_a) for tool holder type Hydro2

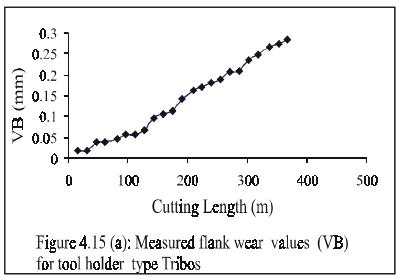

Figure 4.15 (a): Measured flank wear values (VB) for tool holder type Tribos

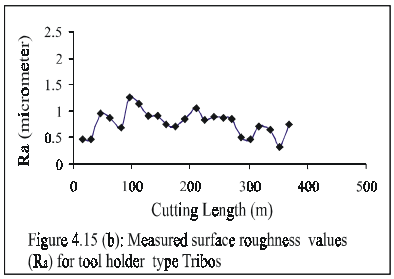

Figure 4.15 (b): Measured surface roughness values (R_a) for tool holder type Tribos

4.4 Experimental Investigation into Chatter Vibration in High Speed Milling with Different Cutting Parameters

To study the influence of cutting parameters on chatter, we need first to develop a technique for chatter detection.
In high speed milling, the chatter frequency detected is about 1 ~ 5 kHz or even above. A very high chatter frequency is difficult/impossible to detect with a dynamometer or accelerometer.
For example, assuming that the cutting process is chattering at frequency say 3 kHz, then the system's response as seen on the workpiece surface is almost zero because the vibration frequency (3 kHz) is much higher than the natural frequencies of the machine table including the dynamometer.
As a result, we can not acquire any signal from the dynamometer or an accelerometer attached onto the workpiece.
However, a microphone is powerful to detect the chatter vibration. When there is chatter, the vibration at chatter frequency will dominate the tool/tool-holder/spindle structure's dynamics. Noise arising from the vibrating cutting process contains a dominant harmonic component at this chatter frequency. After analysing the noise in the frequency domain, we know whether or not chatter occurs.

4.4.1 Chatter Detection in High Speed Milling

Experimental results prove that there is no chatter if the harmonic frequency of the highest peak of the noise signals in cutting is almost equal to one of the three dominant frequencies of the ambient noise detected before cutting or equal to the multiples of the tooth passing frequency. Otherwise a chatter frequency must have been detected with a relatively high level of amplitude. A lot measurements and tests have been done on the machine tool Matsuura (Type: FX-5G). A microphone is placed close to the workpiece to measure the audio signals (see Figure 4.16).

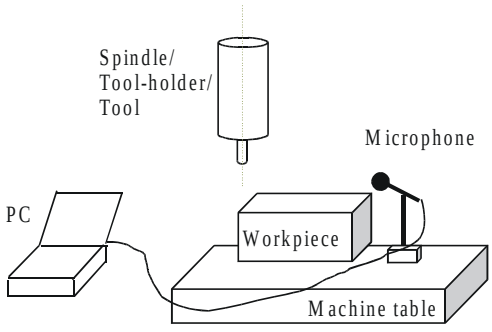

Figure 4.16: Experimental set-up for tests and chatter detection

An end mill with 2 teeth and diameter of 10 mm is used in a dry cutting. The type of the tool holder is Shrink (Hauser). The workpiece material is aluminium. The measured noise at different spindle speeds without material cutting, i.e. air cutting, are listed in Table 4.2 as follows:

Table 4.2: The measured three dominant frequencies and amplitudes of noise in air cutting

Spindle speed (rpm)	Tooth freq. (Hz)	Air cutting					
		1		2		3	
		Freq. (Hz)	Amp. (ratio)	Freq. (Hz)	Amp. (ratio)	Freq. (Hz)	Amp. (ratio)
5,000	167	4685	32	1061	28	937	23
5,500	183	3092	27	2061	25	2127	17
6,000	200	2249	83	3373	55	1124	16
6,500	217	1217	54	2437	35	3656	23
7,000	233	3934	62	2622	49	4572	41
7,500	250	2813	68	3182	49	1405	38
8,000	267	1499	70	3393	33	3001	28
8,500	283	3604	84	3190	34	1593	32
9,000	300	1689	105	3816	57	5068	56
9,500	317	4027	117	1783	115	3566	53
10,000	333	4239	218	1878	157	1874	59
10,500	350	4449	266	1972	128	3936	61
11,000	367	4660	455	2066	148	4122	63
11,500	383	4872	324	2161	160	2155	96
12,000	400	5081	299	2255	114	2249	68
12,500	417	5293	312	2350	99	2343	63
13,000	433	5504	135	2444	104	4888	43
13,500	450	2539	147	5078	107	2531	73
14,000	467	5266	153	2633	137	5925	87
14,500	483	2727	126	5455	115	2719	109
15,000	500	5644	106	2822	79	2813	69
15,500	517	2916	74	3279	68	5832	59
16,000	533	3011	338	3011	163	6770	66
16,500	550	3095	162	6210	126	2124	109
17,000	567	3095	144	6210	115	2124	106
17,500	583	6588	171	3283	126	6720	74
18,000	600	3386	188	3375	158	6772	157
18,500	617	3480	489	6961	179	4834	93
19,000	633	3575	432	7149	218	3562	149
19,500	650	3669	738	7337	297	3815	102
20,000	667	3764	408	7572	245	3750	106

Table 4.3 and Table 4.4 show the measured noise in stable material cutting with feed per tooth f_z = 0.1 mm and depth of cut a_p= 2 and 4 mm, respectively. No chatter occurs in these two cases of test.

Table 4.3: The measured three dominant frequencies and amplitudes of noise in a stable material cutting (without chatter) (a_p=2 mm, f_z=0.1mm)

Spindle speed (rpm)	Tooth freq. (Hz)	Material cutting					
		1		2		3	
		Freq. (Hz)	Amp. (ratio)	Freq. (Hz)	Amp. (ratio)	Freq. (Hz)	Amp. (ratio)
5,000	167	2289	35	1061	27	1227	24
5,500	183	1168	27	2061	21	4852	18
6,000	200	2249	49	3373	41	4317	18
6,500	217	1217	25	3655	24	370	21
7,000	233	3930	68	2969	31	3202	29
7,500	250	2812	74	4218	57	3181	21
8,000	267	3393	54	3000	51	1498	39
8,500	283	1594	81	3604	42	4774	40
9,000	300	3817	189	1688	179	3377	30
9,500	317	1782	144	4027	105	3564	49
10,000	333	4240	241	1877	92	3746	58
10,500	350	1970	121	4451	71	1966	49
11,000	367	4660	424	2064	126	4128	62
11,500	383	4874	131	2159	106	4308	51
12,000	400	2253	169	5084	90	4505	65
12,500	417	2347	180	5296	103	2342	73
13,000	433	2442	155	5506	127	2435	73
13,500	450	2536	196	5073	91	5718	79
14,000	467	2630	166	5261	136	5928	109
14,500	483	5458	89	2725	72	5449	69
15,000	500	5642	50	2812	47	6347	36
15,500	517	2914	120	5829	61	6558	48
16,000	533	3009	194	2999	131	6019	118
16,500	550	3093	459	3104	438	2124	69
17,000	567	3188	222	6398	104	3199	92
17,500	583	3292	135	3281	110	6585	104
18,000	600	3380	229	6760	101	7596	87
18,500	617	3462	97	3475	85	6949	71
19,000	633	3568	227	3556	84	7138	59
19,500	650	3662	333	3649	137	3241	78
20,000	667	3757	239	3742	128	3607	82

Table 4.4: The measured three dominant frequencies and amplitudes of noise in a stable material cutting (without chatter) (a_p=4 mm, f_z=0.1mm)

Spindle speed (rpm)	Tooth Freq. (Hz)	Material cutting					
		1		2		3	
		Freq. (Hz)	Amp. (ratio)	Freq. (Hz)	Amp. (ratio)	Freq. (Hz)	Amp. (ratio)
5,000	167	2289	38	2123	31	1104	24
5,500	183	1032	23	2332	21	2064	20
6,000	200	2252	73	1122	31	926	26
6,500	217	1217	42	2433	23	2440	17
7,000	233	3198	104	3931	72	2621	60
7,500	250	3427	101	3177	79	2808	78
8,000	267	3002	65	1497	50	3389	40
8,500	283	1591	123	1594	84	3601	47
9,000	300	1688	160	3813	71	1684	39
9,500	317	1782	116	4024	59	331	34
10,000	333	4237	122	1876	116	5628	72
10,500	350	4449	186	1970	81	4445	60
11,000	367	4661	160	4119	66	2064	49
11,500	383	2154	106	4308	75	4873	54
15,000	500	2818	105	2811	70	5636	62
18,500	617	3466	300	6932	143	3456	130
19,000	633	3560	349	7127	159	3481	91

The experimental measurement results justify the criterion for chatter detection. For example, at spindle speed of 19,000 rpm, in air cutting one of the dominant frequencies is 3562 Hz (amp. 149) (see Table 4.2). In material cutting without chatter at depth of cut a_p=2 mm, the dominant frequency is 3568 Hz (amp. 227) (see Table 4.3), and also at a_p=4 mm, 3560 Hz (amp. 349). These values of frequency are close to each other. Vibrations at those frequencies are thus all damped transient ones with relatively low amplitude compared to that in a chatter case. The cutting process is stable. No chatter marks appeared on the machined part surface. The measured noise during cutting is mainly contributed by the ambient and/or damped transient vibration noise.

Table 4.5 gives the measured results in an unstable cutting (chatter) case. Comparing the measured dominant chatter frequency and amplitude at a given spindle speed to those in Table 4.2 ~ 4.4, we find that the measured noise in the chatter case is not mainly contributed by the ambient noise and/or forced vibration noise. The harmonic frequencies of forced vibration must be multiples of the teeth passing frequency. Instead the

measured noise in Table 4.5 is mainly contributed by chatter vibration with relatively high amplitude. The chatter frequency is near the natural frequency of a dominant mode of the tool/tool-holder/spindle structure.

Table 4.5: The measured three dominant modes in an unstable cutting case, i.e., with chatter (a_p=4 mm, f_z=0.1mm)

Spindle speed (rpm)	Tooth freq. (Hz)	Material cutting					
		1		2		3	
		Freq. (Hz)	Amp. (ratio)	Freq. (Hz)	Amp. (ratio)	Freq. (Hz)	Amp. (ratio)
12,000	400	3116	972	3515	347	4314	150
12,500	417	3184	744	3599	516	4016	150
13,000	433	3241	694	3672	235	6915	115
13,500	450	3326	451	3776	442	3328	101
14,000	467	3123	1213	3585	222	5259	175
14,500	483	3657	553	3175	497	3177	328
15,500	517	3281	835	3797	386	2912	316
16,000	533	3057	1228	3589	1221	3004	290
16,500	550	3650	960	3101	820	3103	247
17,000	567	3692	489	3130	479	3194	395
17,500	583	3151	1191	3735	405	3289	278
18,000	600	3801	742	3204	615	3371	166
19,500	650	3031	1136	3677	612	3645	340
20,000	667	3051	1110	3714	849	3054	808

4.4.2 Cutting Parameter's Effect on Chatter Vibration in High Speed Milling

Chatter is self-excited vibration due to the interaction of the cutting process with structural dynamics. A change of cutting parameter means a change of the characteristics of the closed-loop milling system (see Figure 2.1 and 2.2 in Chapter 2). The characteristic equation of the closed-loop determines the stability of the cutting process, i.e., whether or not chatter occurs. The settings of cutting parameters include the depth of cut (or chip width) and spindle speed. The overhang of the tool is also crucial for the process stability.

In the following case studies, tests were all conducted on a 3-axis high speed machine Matsuura (Type: FX-5G). Different depth of cut, tool overhang to diameter ratios, and spindle speed were used in dry cutting.

In each set of tests, we change only one parameter for example depth of cut and all others remain the same.

Case 1: The Effect of Depth of Cut (or Chip Width) on Chatter Vibration

Two test results are given here, as shown in Figure 4.17 for test 1 and Figure 4.18 for test 2.

In Test 1, only one speed was used. The end mill used has 3 teeth. The type of tool holder is Collet (NIKKEN). The feed per tooth is 0.05 mm. Two different depths of cut (i.e., a_p = 1, 2 mm) were used for a slot milling at the same spindle speed of 18,000 rpm.

A microphone together with other data acquisition devices was used to measure the audio signals and detect chatter if any (refer to the schematic experimental set-up in Figure 4.16) and the criterion for chatter detection).

The experimental results show that increase of depth of cut will increase the instability of the cutting process. As shown in Figure 4.17, the amplitude of the chatter vibration at a depth of cut of 2 mm is higher than at 1 mm.

The increasing amplitude at chatter frequency will increase the slope of the vibration curve (see section 4.3.1) and thus increase tool wear. But it, in turn, increases the process damping due to the friction at the interface of tool flank and machined surface.

So the measured chatter frequency at the depth of cut of 2 mm is slightly lower than that at 1 mm (see Figure 4.17).

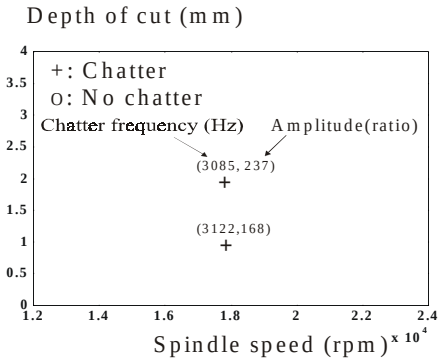

Figure 4.17: The effect of depth of cut on chatter vibration from Test 1

In Test 2, different spindle speeds were checked.

An end-mill with 2 teeth was used. The type of tool holder is Shrink (Hauser). The feed per tooth is 0.1 mm.

The experimental results are shown in Figure 4.18.

The test results justify the observation made in Test 1.

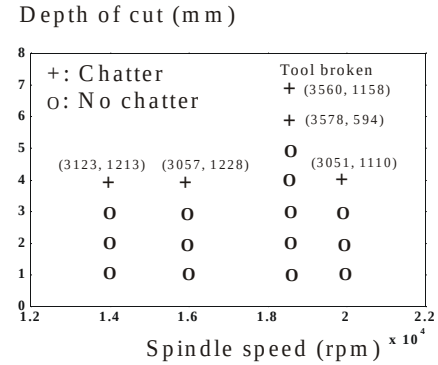

Figure 4.18: The effect of depth of cut on chatter vibration from Test 2

Case 2: The Effect of the Ratio of the Tool Overhang to Diameter on Chatter Vibration

We know that increase of depth of cut will increase process instability and at very low depth of cut there is no chatter as shown in Figure 4.18 of Case 1.
It implies that a transitional state or stability limit must exist at each spindle speed.

To see the influence of the ratio of the tool overhang to diameter on chatter, we thus just compare the stability limit at the same spindle speed for two different overhangs of the same tool.

In tests, two different overhangs (i.e., L_1=60 mm and L_2=65 mm) of an end mill with a diameter of 16 mm and the number of teeth of 4 are used. Feed per tooth (f_z) is 0.05 mm for all the tests. The type of tool holder is Collet (NIKKEN). The data acquisition system and chatter detection techniques are the same as those used in Case 1.

Figure 4.19 shows the experimentally detected stability limits with overhangs of 60 and 65 mm, respectively, at the spindle speeds of 12,705, 14,753, 15,500, 18,000, 21,000, and 23,000 rpm.

This experiment proved that the longer the overhang, the lower the stability.
The static stiffness of the tool/tool-holder assembly with an overhang of 60 mm is obviously higher than that of 65 mm.
The test results show that decrease of static stiffness of the tool/tool-holder assembly will decrease the stability of the cutting process.
This is one of the main reasons why the static stiffness of the tool/tool holder assembly used for high-speed milling is very high.

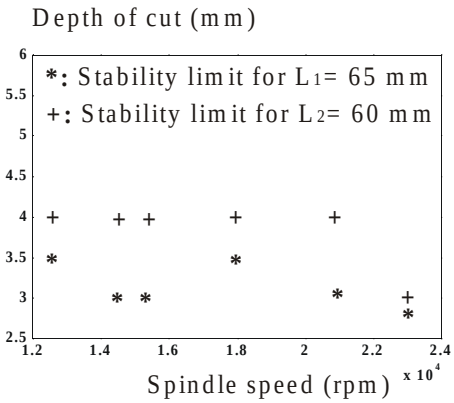

Figure 4.19: The effect of the tool overhang on chatter vibration

Case 3: The Effect of Spindle Speed on Chatter Vibration

Unlike in case 1 and case 2, change of spindle speed will change process stability in a more complicated way. Two test results are given in Figure 4.20 and 4.21. The cutting conditions for Test 1 and 2 are illustrated in Table 4.6 and 4.7, respectively. We find that in some speed range, there is no chatter, but in some others there is chatter. This phenomenon is explained by the "lobe effects" of the stability, which will be discussed in section 4.5 ("Analytical Prediction of Chatter in High-speed Milling").

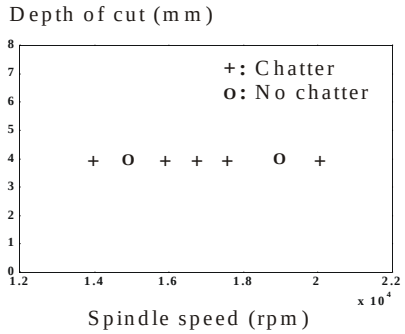

Figure 4.20: The effect of spindle speed on chatter in Test 1

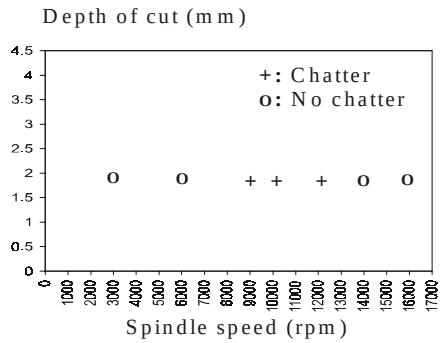

Figure 4.21: The effect of spindle speed on chatter in Test 2

Table 4.6: The cutting conditions for Test 1

Workpiece	Aluminium
Cutting tool	End mill: ∅10(mm), No. of teeth: 2
Tool holder	Shrink (Hauser)
Fluid	Dry
Spindle speed	14,000; 15,000; 16,000; 16,500; 17,500; 19,000; 20,000 (rpm)
Feed/tooth	f_z = 0.1 (mm)
Depth of cut	a_p= 4 (mm)

Table 4.7: The cutting conditions for Test 2

Workpiece	Steel C45 (HRC 23)
Cutting tool	Ball-end mill: ∅10(mm), No. of teeth: 2
Tool holder	Shrink (Hauser)
Fluid	Dry
Spindle speed	3,000, 6,000, 9,000, 10,000, 12,000, 14,000, 16,000 (rpm)
Feed/tooth	f_z = 0.1 (mm)
Depth of cut	a_p= 2 (mm)

4.5 Analytical Prediction of Chatter in High Speed Milling

The reason why the cutting process loses its stability under some cutting conditions as the previous test results show (section 4.4) is that during cutting, dynamic feedback forces are induced from the transient vibration. The induced dynamic force and its effect on the stability of the cutting process will be studied in detail in this section. The method for analytical prediction of chatter and the strategy for selection of optimal spindle speed will be described and verified for a single and multiple degree-of-freedom system in high-speed milling of aluminium.

4.5.1 Dynamic Forces Induced from Vibrating Cutting Process

Figure 4.22 (a) illustrates a dynamic cutting process.
The waviness of chip thickness around the nominal value (h) produces a dynamic force component, which is in phase with the dynamic deviation of chip thickness, as shown in Figure 4.22 (b).

In addition, the clearance angle takes its minimum value at B corresponding to a maximum dynamic force. It takes its maximum value at D corresponding to a minimum force.

At position A, C, and E, the force is equal to a mean value.
The induced

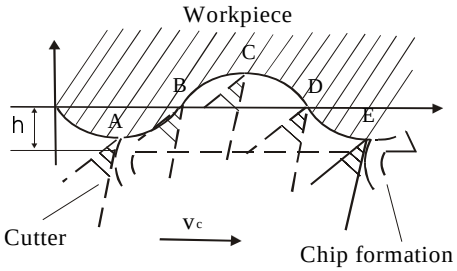

(a):Dynamic chip formation process

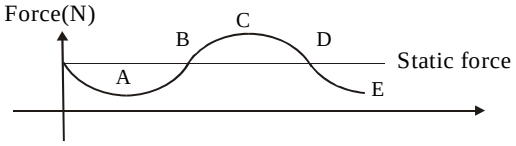

(b): Induced fluctuated force component due to the variation of chip thickness

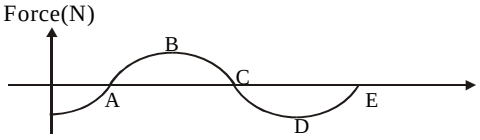

(c): Induced fluctuated force component due to the variation of effective clearance angle

Figure 4.22: The induced dynamic force components due to the vibration of the tool relative to workpiece

dynamic force due to the change of effective clearance angle is schematically plotted in Figure 4.22 (c). It has 90^0 phase shift with the chip variation force (Figure 4.22 (b)).
Given that cutting speed is v_c and vibration frequency is f_c, the wave length (λ) is then expressed as

$$\lambda = v_c / f_c$$

It is clear that if the vibration frequency (f_c) keeps unchanged, the higher the cutting speed (v_c), the longer the wave length, the smaller the slope of the vibration curve at the corresponding point, the larger the clearance angle, the lower the dynamic force induced.

At high-speed milling, this kind of dynamic force will not be taken into account in the following force models for chatter analysis.

4.5.2 Modelling of the Dynamic Milling Force Due to the Variation of Chip Thickness

Here we consider only the vibration of the tool/tool-holder/spindle assembly in the XOY (i.e., horizontal) plane, as shown in Figure 4.23.
The position angle of the tooth j is ϕ_j. Feed (f_z) is in the X-axis direction.
Dynamic displacements (x(t) and y(t)) of the tooth j will influence the chip thickness (h), which is measured in the radial direction (F_r).

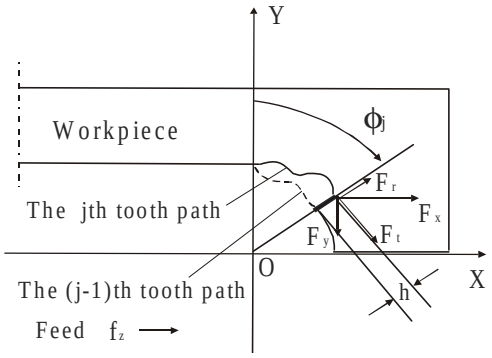

Figure 4.23: A schematic presentation of the milling operation to model the dynamic force

The modulation of chip thickness at present tooth path depends on position angle (ϕ_j) of the tool and the dynamic displacements. It can be expressed as

$$\Delta h_j(\phi_j) = [x(t)\sin(\phi_j) + y(t)\cos(\phi_j)]\, g_j(\phi_j)$$

Where:
$g_j(\phi_j)$ is a unit step function, its value is given as follows:
$g_j(\phi_j) = 0$ (out of cut) or $g_j(\phi_j) = 1$ (in cut)

The dynamic tangential (F_{tj}) and radial (F_{tj}) cutting forces acting on tooth j are both proportional to the axial depth of cut (a_p) and chip thickness variation (Δh_j) over a wide range of engagement (see section 3.7 in Chapter 3), i.e.,

$$F_{tj} = k_t\, a_p\, [\Delta h(\phi_j)]$$
$$F_{rj} = k_r\, a_p\, [\Delta h(\phi_j)]$$

Where:
k_t: the tangential specific force
k_r: the radial specific force

The dynamic force variation in the XOY system for tooth j at the present path is calculated from the coordinate transformation as

$$F_{xj}(t) = -F_{tj}\cos\phi_j - F_{rj}\sin\phi_j$$
$$F_{yj}(t) = -F_{tj}\sin\phi_j - F_{rj}\cos\phi_j$$

After summing the cutting force components contributed by all the teeth, we have

$$F_x(t) = \sum F_{xj}(t)$$
$$F_y(t) = \sum F_{yj}(t)$$

Where:
j = 0,…N-1 (N: the number of teeth).

Combining the above equations, after some mathematical manipulation, a matrix form of the dynamic X- and Y-axis force ($F_{x1}(t)$ and $F_{y1}(t)$) at the present tooth path is

$$\begin{bmatrix} F_{x1}(t) \\ F_{y1}(t) \end{bmatrix} = a_p \cdot \begin{bmatrix} a_{11}(t) & a_{12}(t) \\ a_{21}(t) & a_{22}(t) \end{bmatrix} \cdot \begin{bmatrix} x(t) \\ y(t) \end{bmatrix}$$

Where:
$F_{x1}(t)$: the X-axis force at present tooth path
$F_{y1}(t)$: the Y-axis force at present tooth path
a_p: the depth of cut
$a_{ij}(t)$ (i, j = 1, 2): the time varying directional milling force coefficients.

Unlike in turning, the force direction in milling changes with time due to the time varying coefficient $a_{ij}(t)$. Their value are given as follows:

$a_{11}(t) = [(1/2)] \sum\{-g_j[k_t \sin 2\phi_j + k_r(1-\cos 2\phi_j)]\}$

$a_{12}(t) = [(1/2)] \sum\{-g_j[k_t + k_t \cos 2\phi_j + k_r \sin 2\phi_j]\}$

$a_{21}(t) = [(1/2)] \sum\{g_j[k_t - k_t \cos 2\phi_j - k_r \sin 2\phi_j]\}$

$a_{22}(t) = [(1/2)] \sum\{g_j[k_t \sin 2\phi_j - k_r(1+\cos 2\phi_j)]\}$

Where:
$\phi_j = \omega t + j(2\pi / N)$
$j = 0,1,2, \ldots N-1$
ω: the angular spindle speed
N: the number of teeth

Similarly the X- and Y-axis force (F_{x2} and F_{y2}) produced from the chip waves left by the previous tooth path with tooth period T are found as

$$\begin{bmatrix} F_{x2}(t) \\ F_{y2}(t) \end{bmatrix} = a_p \cdot \begin{bmatrix} a_{11}(t) & a_{12}(t) \\ a_{21}(t) & a_{22}(t) \end{bmatrix} \cdot \begin{bmatrix} x(t-T) \\ y(t-T) \end{bmatrix}$$

By considering $x(t-T) = e^{-TD} x(t)$ and $y(t-T) = e^{-TD} y(t)$, here D is the differential operator d/dt (see a mathematical proof in Appendix B), we can rewrite the above equation as

$$\begin{bmatrix} F_{x2}(t) \\ F_{y2}(t) \end{bmatrix} = a_p \cdot \begin{bmatrix} a_{11}(t) & a_{12}(t) \\ a_{21}(t) & a_{22}(t) \end{bmatrix} \cdot e^{-TD} \cdot \begin{bmatrix} x(t) \\ y(t) \end{bmatrix}$$

The total dynamic force with considering the present and previous tooth path is therefore calculated as

$$\begin{bmatrix} F_x(t) \\ F_y(t) \end{bmatrix} = \begin{bmatrix} F_{x1}(t) - F_{x2}(t) \\ F_{y1}(t) - F_{y2}(t) \end{bmatrix} = a_p \begin{bmatrix} a_{11}(t) & a_{12}(t) \\ a_{21}(t) & a_{22}(t) \end{bmatrix} (1 - e^{-TD}) \begin{bmatrix} x(t) \\ y(t) \end{bmatrix} \qquad (4.3)$$

4.5.3 Modelling of the Structural Dynamics

From section 4.2.2, we know that the equation of motion of a multiple degree-of-freedom system is generally given as

$$\{X(s)\} = [H(s)]\{F(s)\}$$

Where:
{X(s)}: the tool displacement vector relative to the work-piece
{F(s)}: the total cutting force vector
[H(s)]: the transfer matrix as seen at the tool tip.

For milling operation with vibration in both X- and Y-axis direction, the above equation can be further written as

$$\begin{bmatrix} x(s) \\ y(s) \end{bmatrix} = \begin{bmatrix} h_{11}(s) & h_{12}(s) \\ h_{21}(s) & h_{22}(s) \end{bmatrix} \cdot \begin{bmatrix} F_x(s) \\ F_y(s) \end{bmatrix}$$

Where:
x(s), y(s): the X- and Y-axis displacement of the tool relative to workpiece, respectively
$h_{ij}(s)$ (i, j = 1, 2): the element of [H(s)]
$F_x(s)$, $F_y(s)$: the dynamic X- and Y-axis force, respectively

To discuss a time varying system, we rewrite the above model in the time domain as

$$\begin{bmatrix} x(t) \\ y(t) \end{bmatrix} = [H(D)] \cdot \begin{bmatrix} F_x(t) \\ F_y(t) \end{bmatrix} \qquad (4.4)$$

Where:
D: the differential operator d/dt

$$[H(D)] = \begin{pmatrix} h_{11}(D) & h_{12}(D) \\ h_{21}(D) & h_{22}(D) \end{pmatrix}$$

4.5.4 Characteristic Equation of the Closed-Loop System

Combining equation (4.3) and (4.4) yields the equation of motion of the closed-loop system (after eliminating x(t) and y(t)):

$$\begin{bmatrix} F_x(t) \\ F_y(t) \end{bmatrix} + a_p \begin{bmatrix} a_{11} & a_{12} \\ a_{21} & a_{22} \end{bmatrix} (e^{-TD} - 1) \begin{bmatrix} h_{11}(D) & h_{12}(D) \\ h_{21}(D) & h_{22}(D) \end{bmatrix} \cdot \begin{bmatrix} F_x(t) \\ F_y(t) \end{bmatrix} = \begin{bmatrix} 0 \\ 0 \end{bmatrix}$$

Or simplified as

$$\mathbf{F} + a_p \cdot \mathbf{B}(t, D) \cdot \mathbf{F} = \{0\} \qquad (4.5)$$

Where:

$$\mathbf{B}(t, D) = \begin{bmatrix} a_{11} & a_{12} \\ a_{21} & a_{22} \end{bmatrix} (e^{-TD} - 1) \begin{bmatrix} h_{11}(D) & h_{12}(D) \\ h_{21}(D) & h_{22}(D) \end{bmatrix}$$
$$= \mathbf{A}(t) \cdot (e^{-TD} - 1) \cdot \mathbf{H}(D).$$

$$\mathbf{F} = \begin{bmatrix} F_x(t) \\ F_y(t) \end{bmatrix}$$

Noting that the time varying directional force coefficient $a_{ij}(t)$ is a periodic function with the period of T, thus a solution to **F** has the form of

$$\mathbf{F} = e^{st} \cdot \mathbf{P}$$

Where:
P: a periodic function vector with period T.
s: a complex parameter.

We expand the periodic function **P** into the Fourier series as

$$\mathbf{P} = \sum_{k=-\infty}^{\infty} \mathbf{P}_k \cdot e^{jk\omega t}$$

Where:
$\mathbf{P}_k$: the k^{th} Fourier series coefficient of **P**, i.e.,

$$\mathbf{P}_k = \frac{1}{T} \int_0^T \mathbf{P} \cdot e^{-jk\omega t} dt$$

ω: the angular frequency (equal to $2\pi / T$)

Substituting $\mathbf{F} = e^{st}\mathbf{P}$ into equation (4.5), we have

$$e^{st} \cdot \mathbf{P} + a_p \cdot \mathbf{B}(t, D) \cdot e^{st} \cdot \sum_{k=-\infty}^{\infty} (\mathbf{P}_k \cdot e^{jk\omega t}) = \{0\}$$

Or equivalently

$$e^{st} \cdot \mathbf{P} + a_p \cdot \sum_{k=-\infty}^{\infty} [\mathbf{B}(t, D) \cdot e^{(s+jk\omega)t} \cdot \mathbf{P}_k] = \{0\}$$

Considering $\mathbf{B}(t, D) \cdot e^{(s+jk\omega)t} = e^{(s+jk\omega)t} \cdot \mathbf{B}(t, s + jk\omega)$, after making substitution we obtain

$$e^{st} \cdot \mathbf{P} + a_p \cdot \sum_{k=-\infty}^{\infty} e^{(s+jk\omega)t} \cdot [\mathbf{B}(t, s+jk\omega) \cdot \mathbf{P}_k] = \{0\}$$

Be aware that the summation is for all possible k values. Crossing the common term e^{st}, it yields

$$\mathbf{P} + a_p \cdot \sum_{k=-\infty}^{\infty} e^{jk\omega t} \cdot [\mathbf{B}(t, s+jk\omega) \cdot \mathbf{P}_k] = \{0\}$$

Multiplying both sides by $(1/T)e^{-jn\omega t}$ and integrating in [0, T], we have

$$\frac{1}{T}\int_0^T \mathbf{P} \cdot e^{-jn\omega t} \cdot dt + a_p \cdot \sum_{k=-\infty}^{\infty} [\frac{1}{T}\int_0^T [\mathbf{B}(t, s+jk\omega) \cdot e^{-j(n-k)\omega t} \cdot dt] \cdot \mathbf{P}_k = \{0\}$$

We know that **P** and **B**(t, s+jkω) are periodic with period of T. Supposing that the n Fourier series coefficient of **P** is $\mathbf{P}_n$ and the (n-k) Fourier series coefficient of **B**(t, s+jkω) is $\mathbf{B}_{n-k}(s+jk\omega)$, a simplified form is given as follows:

$$\mathbf{P}_n + a_p \cdot \sum_{k=-\infty}^{\infty} \mathbf{B}_{n-k}(s+jk\omega) \cdot \mathbf{P}_k = \{0\} \quad (n, k = 0, \pm 1, \pm 2, ...) \qquad (4.6)$$

Where:

$$\mathbf{P}_n = \frac{1}{T}\int_0^T \mathbf{P} \cdot e^{-jn\omega t} \cdot dt$$

$$\mathbf{P}_k = \frac{1}{T}\int_0^T \mathbf{P} \cdot e^{-jk\omega t} \cdot dt$$

$$\mathbf{B}_{n-k}(s+jk\omega) = \frac{1}{T}\int_0^T \mathbf{B}(t, s+jk\omega) \cdot e^{-j(n-k)\omega t} \cdot dt$$

Equation (4.6) defines numbers of simultaneous linear equations in terms of $\mathbf{P}_i$ (i = 0, ±1, ±2, ±3, …). The equation (4.6) has nontrivial solutions if and only if its determinant is zero. Letting the coefficient matrix of equations (4.6) be $\mathbf{C}_p(s, T)$, thus the characteristic equation of the closed loop system is found as

$$\det(\mathbf{C}_p(s, T, a_p)) = 0$$

When n, k = 0, a zero order approximation of this characteristic equation is thus given as

$$1 + a_p \cdot B_0(s) = 0 \qquad (4.7)$$

Similarly the first order approximation with n, k = 0, –1, +1 is

$$\begin{vmatrix} 1+a_pB_0(s) & a_pB_{-1}(s+j\omega) & a_pB_{-2}(s-j\omega) \\ a_pB_1(s) & 1+a_pB_0(s+j\omega) & a_pB_{-1}(s-j\omega) \\ a_pB_2(s) & a_pB_1(s+j\omega) & 1+a_pB_0(s-j\omega) \end{vmatrix} = 0 \cdot$$

Where:
B_i is the ith Fourier series coefficient of B(t, s).

4.5.5 Chatter Prediction for a Single-Degree-of-Freedom System with the Zero Order Approximation Method

Figure 4.24 is a schematic presentation of a single degree of freedom system in milling operation.
For a single degree of freedom system, the dynamic displacement R(t) of the structure, as seen at the tool tip, has to be on the same line, as shown by the mode direction with a position angle α relative to X-axis.
F_{x+y} is the total dynamic cutting force, i.e. the vector summation of X- and Y-axis force (F_x and F_y) at position angle ϕ_j of the j^{th} tooth. It exerts on the workpiece. From Newton's third law in mechanics, a react force of F_{x+y} must act on the tool tip.

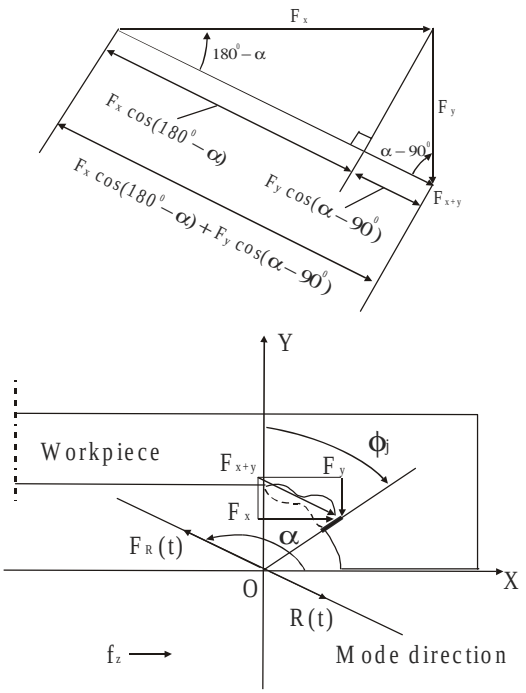

Figure 4.24: The schematic presentation of the vibration of tool/tool-holder/spindle assembly in milling for a single-degree-of-freedom system

This counter-force in general can be decomposed into two components, one in the mode direction and the other perpendicular to the mode direction. In the case of a single-degree-of-freedom system, the force

normal to the mode direction has no influence on the dynamics of the structure. It must be balanced to remain no movement in the direction perpendicular to the mode direction.
Assuming that the component of the total dynamic force F_{x+y} when projected on the mode direction is $F_R(t)$, we use the structural dynamic model (see equation 4.4 in section 4.5.3) and write it for a single degree of freedom system as

$$R(t)= h(D)\, F_R(t) \qquad (4.8)$$

Where:
$F_R(t)$: the component of the total dynamic force F_{x+y} in the mode direction
R(t): the total vibration displacement
h(D): the transfer function in terms of operator D, i.e.
$h(D) = \omega_n^{\,2} /[(\omega_n^{\,2} + D^2 + 2\xi\omega_n D)K]$ (Refer to the FRF in section 4.2.1)

The magnitude of force $F_R(t)$ can be calculated as the summation of the components of both $F_x(t)$ and $F_y(t)$ projected on the mode direction (see the geometric presentation of this relationship in Figure 4.24), or in a matrix form as

$$F_R(t) = -[\cos(180^0 - \alpha) \quad \cos(\alpha - 90^0)] \cdot \begin{bmatrix} F_x(t) \\ F_y(t) \end{bmatrix}$$

Substituting the X- and Y-axis force (see equation 4.3 in section 4.5.2), we have

$$F_R(t) = [\cos(180^0 - \alpha) \quad \cos(\alpha - 90^0)] \cdot a_p \begin{bmatrix} a_{11}(t) & a_{12}(t) \\ a_{21}(t) & a_{22}(t) \end{bmatrix} (e^{-TD} - 1) \begin{bmatrix} x(t) \\ y(t) \end{bmatrix} \qquad (4.9)$$

To establish the relationship between the force $F_R(t)$ and the total displacement R(t) as seen at the tool tip, we decompose the total displacement R(t) into two components, one in the X-direction and the other in the Y- direction (x(t) and y(t)), i.e.

$$\begin{bmatrix} x(t) \\ y(t) \end{bmatrix} = \begin{bmatrix} \cos\alpha \\ \sin\alpha \end{bmatrix} \cdot R(t) \qquad (4.10)$$

Combining equation (4.9) and (4.10), with some mathematical manipulation we obtain (after deleting t)

$$F_R = a_p \cdot a_0 \cdot (1 - e^{-TD}) \cdot R \qquad (4.11)$$

Where:

$$a_0 = -\sin\alpha \cdot \cos\alpha \cdot a_{21}(t) - \sin^2\alpha \cdot a_{22}(t) + \cos^2\alpha \cdot a_{11}(t) + \sin\alpha \cdot \cos\alpha \cdot a_{12}(t)$$

Combining equation (4.11) and (4.8) yields

$$F_R + a_p \cdot B(t, D) \cdot F_R = 0$$

Where:

$$B(t, D) = a_0 \cdot (e^{-TD} - 1) \cdot h(D)$$

The characteristic equation with zero order approximation for a single degree-of-freedom system can thus be found as (see equation (4.7) in section 4.5.4)

$$1 + a_p \cdot B_0(s) = 0$$

Where:

$$B_0(s) = (e^{-Ts} - 1) \cdot h(s) \cdot \frac{1}{T} \cdot \int_0^T a_0 \cdot dt$$

After substituting h(s) and $B_0(s)$, it yields

$$1 - a_p \cdot (1 - e^{-sT}) \cdot \frac{\omega_n^2}{(s^2 + 2\xi\omega_n s + \omega_n^2) \cdot K} \cdot \frac{1}{T} \cdot \int_0^T a_0 \cdot dt = 0$$

Or equivalently

$$1 - \frac{\omega_n^2}{(s^2 + 2\xi\omega_n s + \omega_n^2)} \cdot a_p \cdot C_p \cdot (1 - e^{-sT}) = 0$$

Where:

$$C_p = \frac{1}{KT} \cdot \int_0^T a_0 \cdot dt \ )$$

C_p is the average value of $(1/KT)a_0$ over the period T (based on zero order approximation). It depends on structure stiffness K, tooth period T and a_0. Notice that the time varying coefficients a_{11}, a_{12}, a_{21} and a_{22} are time variant with period T (see the definition of a_{ij} (i, j = 1, 2) in section 4.5.2). Hence a_0 is also time variant with period T (see the expression of a_0 below

equation 4.11). Its value depends on mode direction α and the time varying coefficients a_{ij}, which are function of the specific cutting force k_t and k_r, the number of teeth N, unit step function g_j and the angular spindle speed ω.

Letting $s = j\omega_c$ (at stability limit), we have

$$1 - \frac{\omega_n^2}{\omega_n^2 - \omega_c^2 + 2\xi\omega_n j\omega_c} a_p C_p (1 - e^{-j\omega_c T}) = 0$$

After rearranging the above equation and taking into account

$$e^{-j\omega_c T} = \cos(\omega_c T) - j\sin(\omega_c T), \text{ then}$$

$$\omega_n^2 - \omega_c^2 + \omega_n^2 a_p C_p (\cos\omega_c T - 1) + (2\xi\omega_n\omega_c - \omega_n^2 a_p C_p \sin\omega_c T) j = 0$$

or rewritten as two simultaneous equations:

$$\omega_n^2 - \omega_c^2 + \omega_n^2 a_p C_p (\cos\omega_c T - 1) = 0 \qquad (4.12)$$

$$2\xi\omega_n\omega_c - \omega_n^2 a_p C_p \sin\omega_c T = 0 \qquad (4.13)$$

Eliminating $\omega_n^2 a_p C_p$ of equation (4.12) and (4.13), after making some simple mathematical manipulation, we obtain

$$\omega_n^2 - \omega_c^2 = 2\xi\omega_n\omega_c \tan(\frac{\omega_c T}{2}) \qquad (4.14)$$

Equation (4.14) establishes the relationship of the teeth passing period, chatter frequency, natural frequency, and damping ratio.
It implies that the dynamic characteristics of the structure ω_n and ξ can be picked out if the same mode is responsible for two cases of chatter, i.e., at different spindle speeds, i.e. different T values.
Furthermore the constant C_p can also be found from equation (4.12) and (4.13) given a known limit depth of cut a_p and measured chatter frequency ω_c as well as the natural frequency ω_n and damping ratio ξ for a given spindle speed (see equation 4.17 below).
The stability lobes for a single degree of freedom system can therefore be readily calculated by using previous equations. More specifically, from equation (4.14), after rearrangement we have

$$\omega_c T = \left[2\pi - 2\tan^{-1}\left(\frac{\omega_c^2 - \omega_n^2}{2\xi\omega_n\omega_c}\right) \right] + 2k\pi \qquad (k = 0, 1, 2, \cdots) \qquad (4.15)$$

$\omega_c T$ is the angular distance traveled by the tooth at the chatter frequency ω_c during tooth period T. Thus $\omega_c T$ presents the phase shift of two successive tooth engagements.

The tooth period T is then derived as

$$T = \frac{2(k+1)\pi}{\omega_c} - \frac{2}{\omega_c}\tan^{-1}\left(\frac{\omega_c^2 - \omega_n^2}{2\xi\omega_n\omega_c}\right) \quad (k = 0, 1, 2, \cdots)$$

Spindle speed (n) can be calculated from tooth passing period T, i.e.,

$$n = \frac{1}{N \cdot T} = \frac{\omega_c}{N \cdot [2(k+1)\pi - 2\tan^{-1}\left(\frac{\omega_c^2 - \omega_n^2}{2\xi\omega_n\omega_c}\right)]} \quad (k = 0, 1, 2, \cdots) \qquad (4.16)$$

Where:
N is the number of teeth.

The Limit depth of cut (a_p) is found from equation (4.12) and (4.13) as

$$a_p = \frac{(\omega_n^2 - \omega_c^2)^2 + 4\xi^2\omega_n^2\omega_c^2}{2C_p\omega_n^2(\omega_n^2 - \omega_c^2)} \qquad (4.17)$$

The mapping of spindle speeds (n) and depths of cut (a_p), which are calculated from equations (4.16) and (4.17), respectively, defines a group of curves in a graph with spindle speed (n) and depth of cut (a_p) as co-ordinates. They are so-called stability lobes (see Figure 2.3 in section 2.2 of Chapter 2).

To have a physical understanding of these equations (4.14) ~ (4.17), we discuss the possible values of phase shift ($\omega_c T$).

Case 1: phase shift $\omega_c T = 2k\pi$ (k = 0, 1, 2…)

For a harmonic vibration x(t) in the X direction, letting $x(t) = \sin(\omega_c t)$ with vibration amplitude of 1 for simplicity and at limit stability (i.e. amplitude

of x(t) equals that of previous tooth path x(t – T), both equal to 1), we have the following derivation of x(t – T) :

$$x(t-T) = \sin[\omega_c(t-T)] = \sin(\omega_c t - \omega_c T) = \sin(\omega_c t - 2k\pi) = \sin(\omega_c t) = x(t)$$

Similarly, for the harmonic vibration y(t) in the Y direction, we have

$$y(t-T) = \sin[\omega_c(t-T)] = \sin(\omega_c t - \omega_c T) = \sin(\omega_c t - 2k\pi) = \sin(\omega_c t) = y(t)$$

The derivations prove that the dynamic vibration (at the stability limit) at the present and previous path is equal. Thus the chip variation is zero and hence the dynamic force is zero, too.
This is an ideal case, in which no chatter can happen because the total dynamic feedback force is zero.

Case 2: the phase shift: $2k\pi + \pi < \omega_c T < 2k\pi + 2\pi$ (k = 0, 1, 2…)

If $2k\pi + \pi < \omega_c T < 2k\pi + 2\pi$, then

$$\tan(\frac{\omega_c T}{2}) < 0 \quad \text{and} \quad \sin(\omega_c T) < 0$$

From equation (4.14), we derive

$$\omega_c > \omega_n \quad (\text{because } \omega_n > 0 \text{ and } \xi > 0).$$

It implies that the chatter frequency is always in the negative part of the real part of the frequency response function (FRF) of the machine structure (refer to the measured real part of the FRF in Figure 4.7(a) and 4.8 (a) of section 4.2.3).

In addition, from equation (4.13), we derive that

$$C_p = \frac{1}{KT} \cdot \int_0^T a_0 \cdot dt \; < 0$$

The sign of C_p is dependent on time varying force coefficient a_0 (see the definition of a_0 in equation 4.11).

The negative value of C_p means the dynamic cutting force ($F_R(t)$) in the mode direction is in anti-phase (i.e.,180^0) with displacement (R(t)), as shown in Figure 4.24.

After dividing both the numerator and denominator of the right hand side of equation (4.17) by ω_n^4, and making some rearrangement, we have

$$a_p = \frac{1}{2 \cdot C_p \cdot \dfrac{1-(\omega_c/\omega_n)^2}{\left[1-(\omega_c/\omega_n)^2\right]^2 + 4\xi^2(\omega_c/\omega_n)^2}}$$

$$= \frac{1}{2 \cdot a_0 \cdot \dfrac{1-(\omega_c/\omega_n)^2}{\left[1-(\omega_c/\omega_n)^2\right]^2 + 4\xi^2(\omega_c/\omega_n)^2} \cdot \dfrac{1}{K}}$$

$$= \frac{1}{2 \cdot a_0 \cdot \mathrm{Re}[h_0(j\omega)]} \quad (a_0 < 0 \text{ when } C_p < 0)$$

Where:

$$\mathrm{Re}[h_0(j\omega)] = \frac{1-(\omega_c/\omega_n)^2}{\left[1-(\omega_c/\omega_n)^2\right]^2 + 4\xi^2(\omega_c/\omega_n)^2} \cdot \frac{1}{K}$$

(See the expression of the real part of the FRF in section 4.2.1)

So, the limit depth of cut is inversely proportional to the real part of the frequency response function (FRF) of the structure.
It is obvious that the lower the static stiffness K, the larger the absolute value of $\mathrm{Re}[h_0(j\omega)]$, and the lower the limit depth of cut a_p, thus the lower the stability of the cutting process.
This agrees with the experimental results shown in Figure 4.19 of section 4.4.2 case 2.

The minimum a_p is obtained when $\mathrm{Re}[h_0(j\omega)]$ takes its maximum negative value. Let $r = \omega_c/\omega_n$, and take the derivative of the function of a_p with respect to variable r, we find that when $r = \sqrt{1+2\xi}$ the minimum value of a_p is

$$a_{min} = \frac{2K\xi(1+2\xi)}{-a_0} \qquad (a_0 < 0)$$

In addition, we write the expression of phase shift ($\omega_c T$) of equation (4.15) as

$$\omega_c T = \varepsilon + 2k\pi \qquad (k = 0, 1, 2, \cdots)$$

Or equivalently

$$f_c / f_t = \varepsilon / 2\pi + k \qquad (\pi <= \varepsilon < 2\pi)$$

Where:
f_c: the chatter frequency (Hz).
f_t: the tooth passing frequency (Hz).
k: the highest integer to meet the above equation.
ε: the phase shift (radian) of the two successive tooth passes after crossing the angle of $2k\pi$.

The value of ε is given as (see equation (4.15))

$$\varepsilon = 2\pi - 2\tan^{-1}\left(\frac{\omega_c^2 - \omega_n^2}{2\xi\omega_n\omega_c}\right) = 2\pi - 2\tan^{-1}\left(\frac{\mathrm{Re}[h_0(j\omega)]}{\mathrm{Im}[h_0(j\omega)]}\right)$$

Where:
$\mathrm{Re}[h_0(j\omega)]$: the real part of the frequency response function (FRF)
$\mathrm{Im}[h_0(j\omega)]$: the imaginary part of the frequency response function (FRF) (see the expression of the imaginary part of the FRF also in section 4.2.1)

The value of $(\varepsilon/2\pi)$ corresponds to the fractional part of the ratio (f_c/f_t).
The phase shift (ε) is thus determined by the ratio of the real part to imaginary part of the FRF, as graphically shown in Figure 4.25.

The integer number k is the number of waves contained over the phase shift.
A graphic presentation of the regenerative relationship is shown in Figure 4.26.

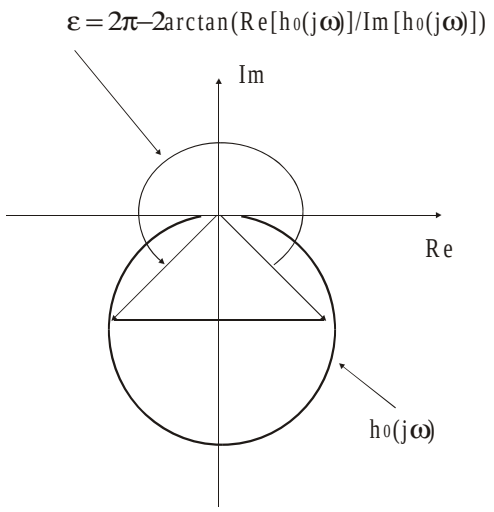

Figure 4.25: A graphic presentation of the relationship of the phase shift and structure frequency response function

We know that when $r = \sqrt{1+2\xi}$ ($r=\omega_c/\omega_n$), the depth of cut (a_p) takes its minimum value (a_{min}).
The corresponding critical phase shift can be calculated as

$$\varepsilon_c = 2\pi - 2\tan^{-1}\left(\frac{\omega_c^2-\omega_n^2}{2\xi\omega_n\omega_c}\right)$$

$$= 2\pi - 2\tan^{-1}\left(\frac{1}{\sqrt{1+2\xi}}\right)$$

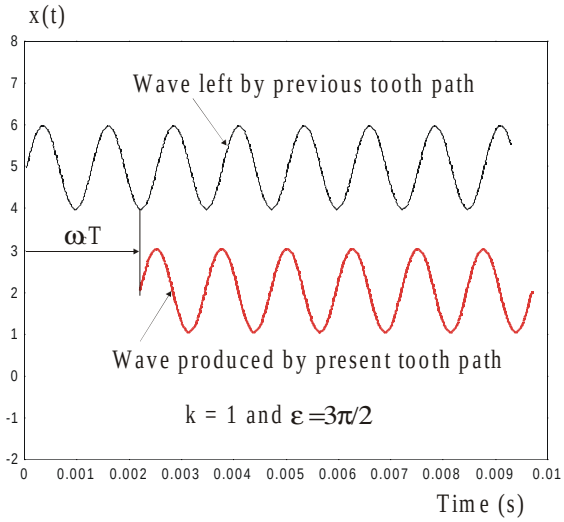

Figure 4.26: A graphic presentation of the relationship between phase shift and the number of waves

It is worth noting that the maximum dynamic force occurs when $\varepsilon = \pi$ (full anti-phase), but it doesn't correspond to the least stability. Instead the minimum depth of cut a_p corresponds to the critical phase shift ε_c, which depends on the damping of the structure.

Case 3: the phase shift: $2k\pi < \omega_c T < 2k\pi + \pi$ (k = 0, 1, 2…)

If $2k\pi < \omega_c T < 2k\pi+\pi$, then

$$\tan\left(\frac{\omega_c T}{2}\right) > 0 \quad \text{and} \quad \sin(\omega_c T) > 0$$

From equation (4.14), we derive

$$\omega_c < \omega_n \quad (\text{because } \omega_n > 0 \text{ and } \xi > 0).$$

It means that the chatter frequency is always in the positive region of the real part of the frequency response function (FRF) of the machine structure (also refer to the measured real part of the FRF in Figure 4.7(a) and 4.8 (a) in section 4.2.3).
In addition, from equation (4.13), we have

$$C_p > 0.$$

The positive value of C_p means the dynamic cutting force ($F_R(t)$) in the mode direction is in phase (i.e., 0^0) with dynamic displacement (R(t)), as shown in Figure 4.27.

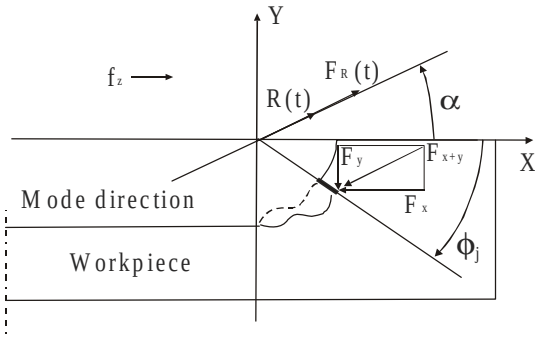

Figure 4.27: The dynamic cutting force $F_R(t)$ is in phase with the displacement R(t) in the mode direction for a single degree of freedom system

Many tests and measurements have been done on the machine Matsuura (Type: FX-5G) in high speed milling aluminium to observe the possible values of phase shift for these two cases.

In each test, chatter frequencies at stability limits were detected with a microphone (refer to the experimental set-up in Figure 4.16 in section 4.4.1). Some of the experimental results are listed in Table 4.8 for Case 2 and Table 4.9 for Case 3 as follows:

Table 4.8: the experimental results for Case 2, i.e.,
$2k\pi + \pi < \omega_c T < 2k\pi + 2\pi$, $k = 0, 1, 2\ldots$

	Test 1	Test 2	Test 3	Test 4
Chatter freq. (Hz)	4179	5486	3933	2813
Amplitude (ratio)	481	1543	277	1072
Speed (rpm)	22,000	23,000	21,000	23,000
Tooth period (s)	0.00014	0.0009	0.00013	0.0017
Phase shift (rad.)	35.81	29.97	17.65	23.05
No. of waves (k)	5	4	2	3
ε (degree)	251^0	277^0	291^0	240^0
$\tan(\omega_c T/2)$	– 1.389	– 0.8792	– 0.6829	– 0.7849
Tool type	End mill	End mill	End mill	End mill
Tool diameter (mm)	10	10	16	10
No. of teeth	2	3	4	6
Tool holder Type	Shrink (Hauser)	Collet (NIKKEN)	Collet (NIKKEN)	Shrink (Hauser)
Overhang (mm)	41	30	70	51
Fluid	Dry	Dry	Dry	Dry
Feed/tooth (mm)	0.1	0.05	0.05	0.1
Depth of cut (mm)	4	4	3	2

Table 4.9: the experimental results for Case 3, i.e.,
$2k\pi < \omega_c T < 2k\pi + \pi$, $k = 0, 1, 2\ldots$

	Test 5	Test 6	Test 7	Test 8
Chatter freq. (Hz)	3801	3173	2805	3151
Amplitude (ratio)	481	607	1112	1191
Speed (rpm)	18,000	14,550	12,705	17,500
Tooth period (s)	0.0017	0.0014	0.0012	0.0017
Phase shift (rad.)	39.80	27.40	20.81	33.94
No. of waves (k)	6	4	3	5
ε (degree)	120^0	130^0	112^0	144^0
$\tan(\omega_c T/2)$	1.7532	2.1516	1.4884	3.1350
Tool type	End mill	End mill	End mill	End mill
Tool diameter (mm)	10	10	16	10
No. of teeth	2	3	4	2
Tool holder type	Shrink (Hauser)	Collet (NIKKEN)	Collet (NIKKEN)	Shrink (Hauser)
Overhang (mm)	30	40	60	30
Fluid	Dry	Dry	Dry	Dry
Feed/tooth (mm)	0.1	0.05	0.05	0.1
Depth of cut (mm)	4	2	3	4

From Table 4.8 and 4.9, it is clear that different cutters with different tool overhangs may have different dynamic characteristics (i.e. different natural frequency and damping as well as mode direction, as also mentioned in section 4.3.1). Thus the measured chatter frequency is different (see the experimental result in Test 4 for Case 2 in Table 4.8 and in Test 5 for Case 3 in Table 4.9.

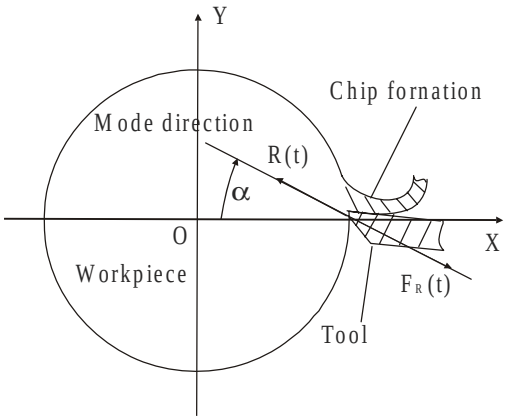

Figure 4.28: A schematic presentation of the turning operation in which the dynamic force $F_R(t)$ is always anti-phase with the dynamic displacement R(t).

Generally speaking, any change of the tool/tool-holder type and/or cutting parameters may change the dynamic behaviour of the cutting process and thus influences the process stability and change the

chatter frequency and phase shift as well.
It is worth noting that in turning the chatter frequency (ω_c) is always larger than the natural frequency (ω_n) because the dynamic force ($F_R(t)$) is always anti-phase with the dynamic displacement ((R(t)), as discussed in Case 2 (see a schematic presentation of the turning operation in Figure 4.28).
In milling, however, this is not always the case as shown in Figure 4.27, in which the dynamic force $F_R(t)$ is in phase with the dynamic displacement (R(t)).

Application and Verification

An example together with the experimental result is given here to illustrate the method of chatter prediction for a single degree of freedom system in high-speed milling of aluminium.
The test was done on the 3-axis high-speed milling machine tool Matsuura (FX-5G). The type of tool holder is Shrink (Hauser). The end mill has 2 teeth. Its diameter is 10 mm. No fluid is used in cutting. Feed per tooth is 0.1 mm. The data acquisition and acoustic measurement system are the same as those given in section 4.4.1 (also refer to the experimental set-up in Figure 4.16).
To identify the characteristics of the structural and process dynamics, two chatter frequencies are needed at two different speeds with different limit depths of cut. The state of chatter at a limit depth of cut is just the transitional state from no chatter to chatter.
During tests, at speeds of 12,000 and 12,500 rpm, two chatter frequencies are measured as 3116 and 3184 Hz with limit depths of 3.5 and 4 mm, respectively.
The tooth periods of these two spindle speeds are 0.0025 and 0.0024 seconds, respectively (noting that the number of teeth is 2).
After substituting these values into the phase shift equation (4.14), we obtain the following two simultaneous equations:

$$\omega_n^2 - (2\pi \cdot 3116)^2 = 2\xi\omega_n (2\pi \cdot 3116) \tan(\frac{(2\pi \cdot 3116)0.0025}{2})$$

$$\omega_n^2 - (2\pi \cdot 3184)^2 = 2\xi\omega_n (2\pi \cdot 3184) \tan(\frac{(2\pi \cdot 3184)0.0024}{2})$$

The solutions to these equations are

ω_n = 19332 (radian/s) or 3077 (Hz) and ξ = 0.0163.

It means that the vibration mode with a natural frequency of 3077 Hz and damping ratio of 0.0163 is responsible for these two cases of chatter vibrations.
The constant C_p is found from equation (4.17), i.e.,

$$C_p = \frac{(\omega_n^2 - \omega_c^2)^2 + 4\xi^2\omega_n^2\omega_c^2}{2a_p\omega_n^2(\omega_n^2 - \omega_c^2)}$$

Putting the values of ω_n and ξ plus a_p=3.5 mm and the chatter frequency $\omega_c = 2\pi$ (3116) radian/s into the above equation, we have

$$C_p = -0.01 \text{ (1/mm)}$$

With a_p = 4 mm and chatter frequency $\omega_c = 2\pi$ (3184) radian/s, we obtain C_p = -0.009 (1/mm), which is almost equal to -0.01 (1/mm). This check on C_p value justifies the point that the same mode is responsible for these two cases of chatter vibration at different spindle speeds.
The spindle speed (n) and depth of cut (a_p) can be readily computed by using equation (4.16) and (4.17) for different values of k and ω_c, i.e.,

$$n = \frac{1}{N \cdot T} = \frac{\omega_c}{N \cdot [2(k+1)\pi - 2\tan^{-1}(\frac{\omega_c^2 - \omega_n^2}{2\xi\omega_n\omega_c})]} \quad (k = 0,\ 1,\ 2, \cdots)$$

$$a_p = \frac{(\omega_n^2 - \omega_c^2)^2 + 4\xi^2\omega_n^2\omega_c^2}{2C_p\omega_n^2(\omega_n^2 - \omega_c^2)}$$

(see a MatLab program in Appendix C).

Stability lobes for the case of a single-degree-of-freedom system are thus figured out and shown in Figure 4.29 together with experimental observations.

This example shows a good agreement between the calculated lobes and the experimental observations.

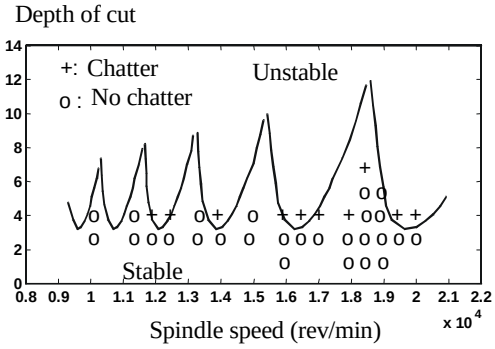

Figure 4.29: Stability Lobes and test results for one degree of freedom system to predict chatter vibration.

This is due to the fact that the structural dynamics of the milling system in this case is dominated by one mode. It is tool/tool-holder assembly dependent. Unfortunately, in many other cases of the tests, the structural dynamics are dominated by two or even three modes.
A technique in chatter prediction for a multiple-degree-of-freedom system therefore needs to be developed. This is done in next section.

4.5.6 Chatter Prediction for a Multiple-Degree-of-Freedom System

For a multiple degree of freedom system, the interaction of different modes of the structure makes the coupled dynamic behaviour more complicated than that for a single degree of freedom system. A case of two degrees of freedom system is shown in Figure 30.

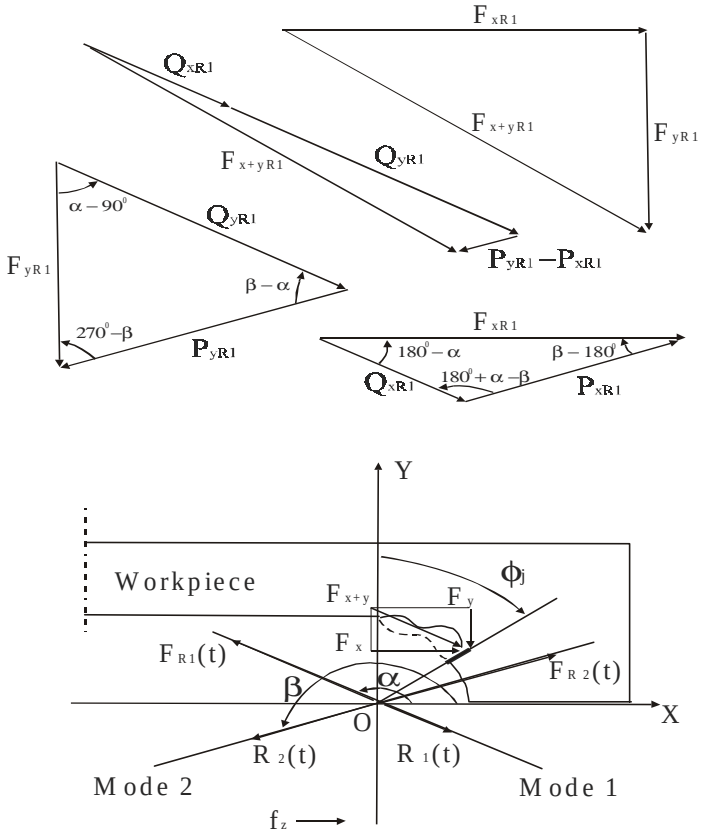

Figure 4.30: A schematic presentation of the vibration of Tool/ tool-holder/spindle structure for a 2 degree-of-freedomsystem and the graphic presentation of the force relationships

We assume that two independent dynamic displacements $R_1(t)$ and $R_2(t)$ as seen at the tool tip take place during cutting. These two dynamic vibrations occur on the lines Mode 1 and Mode 2, respectively. Position angles of Mode 1 and Mode 2 with respect to X-axis are α and β, respectively.
$R_1(t)$ and $R_2(t)$ can both be decomposed as two vibration components on X- and Y-axis, i.e. $x_1(t)$ and $y_1(t)$ for $R_1(t)$, and $x_2(t)$ and $y_2(t)$ for $R_2(t)$, Or mathematically

$$\begin{bmatrix} x_1(t) \\ y_1(t) \end{bmatrix} = \begin{bmatrix} \cos\alpha \\ \sin\alpha \end{bmatrix} \cdot R_1(t)$$

$$\begin{bmatrix} x_2(t) \\ y_2(t) \end{bmatrix} = \begin{bmatrix} \cos\beta \\ \sin\beta \end{bmatrix} \cdot R_2(t)$$

From equation 4.3 in section 4.5.2, we can calculate the resultant dynamic X- and Y-axis force components $F_{xR1}(t)$ and $F_{yR1}(t)$ from displacement $R_1(t)$, and also $F_{xR2}(t)$ and $F_{yR2}(t)$ from $R_2(t)$, separately, i.e.

$$\begin{aligned} \begin{bmatrix} F_{xR1}(t) \\ F_{yR1}(t) \end{bmatrix} &= a_p \begin{bmatrix} a_{11}(t) & a_{12}(t) \\ a_{21}(t) & a_{22}(t) \end{bmatrix} (1 - e^{-TD}) \begin{bmatrix} x_1(t) \\ y_1(t) \end{bmatrix} \\ &= a_p \begin{bmatrix} a_{11}(t) & a_{12}(t) \\ a_{21}(t) & a_{22}(t) \end{bmatrix} (1 - e^{-TD}) \begin{bmatrix} \cos\alpha \\ \sin\alpha \end{bmatrix} R_1(t) \end{aligned} \qquad (4.18)$$

$$\begin{aligned} \begin{bmatrix} F_{xR2}(t) \\ F_{yR2}(t) \end{bmatrix} &= a_p \begin{bmatrix} a_{11}(t) & a_{12}(t) \\ a_{21}(t) & a_{22}(t) \end{bmatrix} (1 - e^{-TD}) \begin{bmatrix} x_1(t) \\ y_1(t) \end{bmatrix} \\ &= a_p \begin{bmatrix} a_{11}(t) & a_{12}(t) \\ a_{21}(t) & a_{22}(t) \end{bmatrix} (1 - e^{-TD}) \begin{bmatrix} \cos\beta \\ \sin\beta \end{bmatrix} R_2(t) \end{aligned} \qquad (4.19)$$

The X- and Y-axis force components $F_{xR1}(t)$ and $F_{yR1}(t)$ both can further be decomposed as two components on mode 1 and Mode 2, i.e. Q_{xR1} and P_{xR1} for $F_{xR1}(t)$, and Q_{yR1} and P_{yR1} for $F_{yR1}(t)$, as illustrated in Figure 4.30 by two triangles of forces.
From the basics of geometry, we have

$$\frac{Q_{xR1}}{\sin(\beta - 180^0)} = \frac{P_{xR1}}{\sin(180^0 - \alpha)} = \frac{F_{xR1}}{\sin(180^0 + \alpha - \beta)}$$

$$\frac{Q_{yR1}}{\sin(270^0-\beta)}=\frac{P_{yR1}}{\sin(90^0-\alpha)}=\frac{F_{yR1}}{\sin(\beta-\alpha)}$$

Solving for Q_{xR1}, Q_{yR1}, P_{xR1} and P_{yR1}, we obtain

$$Q_{xR1}=\frac{\sin(\beta-180^0)}{\sin(180^0+\alpha-\beta)}F_{xR1},\quad Q_{yR1}=\frac{\sin(270^0-\beta)}{\sin(\beta-\alpha)}F_{yR1}$$

$$P_{xR1}=\frac{\sin(180^0-\alpha)}{\sin(180^0+\alpha-\beta)}F_{xR1},\quad P_{yR1}=\frac{\sin(\alpha-90^0)}{\sin(\beta-\alpha)}F_{yR1}$$

The vector summation of F_{xR1} and F_{yR1} gives the dynamic force F_{x+yR1} resulting from the displacement $R_1(t)$ (see a triangle of forces in Figure 4.30). F_{x+yR1} is equivalent to the vector summation of Q_{xR1}, Q_{yR1}, P_{xR1} and P_{yR1} (see a triangle of forces also in Figure 4.30).

We make summation of Q_{xR1} and Q_{yR1}, both parallel to the line Mode 1, and also summation of P_{xR1} and P_{yR1} both parallel to the line Mode 2. Hence, the total dynamic force components Q_{R1} and P_{R1} parallel to Mode 1 and Mode 2, respectively, are found as follows:

$$Q_{R1}=Q_{xR1}+Q_{yR1}=\frac{\sin(\beta-180^0)}{\sin(180^0+\alpha-\beta)}F_{xR1}+\frac{\sin(270^0-\beta)}{\sin(\beta-\alpha)}F_{yR1}$$

$$P_{R1}=P_{xR1}+P_{yR1}=\frac{\sin(180^0-\alpha)}{\sin(180^0+\alpha-\beta)}F_{xR1}+\frac{\sin(\alpha-90^0)}{\sin(\beta-\alpha)}F_{yR1}$$

Or equivalently in a matrix form

$$\begin{bmatrix}Q_{R1}\\P_{R1}\end{bmatrix}=[T]\cdot\begin{bmatrix}F_{xR1}(t)\\F_{yR1}(t)\end{bmatrix}\qquad(4.20)$$

Where:

$$[T]=\begin{bmatrix}\dfrac{\sin(\beta-180^0)}{\sin(180^0+\alpha-\beta)} & \dfrac{\sin(270^0-\beta)}{\sin(\beta-\alpha)}\\ \dfrac{\sin(\beta-180^0)}{\sin(180^0+\alpha-\beta)} & \dfrac{\sin(\alpha-90^0)}{\sin(\beta-\alpha)}\end{bmatrix}$$

Similarly, the total dynamic force components Q_{R2} and P_{R2}, resultant from $R_2(t)$, parallel to Mode 1 and Mode 2, respectively, can be expressed as

$$\begin{bmatrix} Q_{R2} \\ P_{R2} \end{bmatrix} = [T] \cdot \begin{bmatrix} F_{xR2}(t) \\ F_{yR2}(t) \end{bmatrix} \qquad (4.21)$$

Combining equation (4.18) and (4.20), and also equation (4.19) and (4.21), we have

$$\begin{bmatrix} Q_{R1} \\ P_{R1} \end{bmatrix} = [T] \cdot a_p \begin{bmatrix} a_{11}(t) & a_{12}(t) \\ a_{21}(t) & a_{22}(t) \end{bmatrix} (1 - e^{-TD}) \begin{bmatrix} \cos\alpha \\ \sin\alpha \end{bmatrix} R_1(t) \qquad (4.22)$$

$$\begin{bmatrix} Q_{R2} \\ P_{R2} \end{bmatrix} = [T] \cdot a_p \begin{bmatrix} a_{11}(t) & a_{12}(t) \\ a_{21}(t) & a_{22}(t) \end{bmatrix} (1 - e^{-TD}) \begin{bmatrix} \cos\beta \\ \sin\beta \end{bmatrix} R_2(t) \qquad (4.23)$$

Finally, the total dynamic force components $F_{R1}(t)$ and $F_{R2}(t)$, resultant from both $R_1(t)$ and $R_2(t)$, parallel to Mode 1 and Mode 2, respectively, are written as

$$\begin{bmatrix} F_{R1}(t) \\ F_{R2}(t) \end{bmatrix} = \begin{bmatrix} Q_{R1}(t) \\ P_{R1}(t) \end{bmatrix} + \begin{bmatrix} Q_{R2}(t) \\ P_{R2}(t) \end{bmatrix} \qquad (4.25)$$

Notice that in equation 4.22 and 4.23, the element $a_{ij}(t)$ (i, j = 1, 2) of the engagement matrix is time varying with tooth period T (see the definition of $a_{ij}(t)$ in section 4.5.2). We again use zero order approximation and calculate its average value as follows:

$$A_{ij} = \frac{1}{T} \cdot \int_0^T a_{ij}(t) \cdot dt \qquad (i, j = 1, 2)$$

After replacing $a_{ij}(t)$ of equation (4.22) and (4.23) by their corresponding average values A_{ij} and taking Laplace transform, we can rewrite equation (4.22) and (4.23) with complex variable s as

$$\begin{bmatrix} Q_{R1}(s) \\ P_{R1}(s) \end{bmatrix} = [T] \cdot a_p \cdot [A] (1 - e^{-Ts}) \begin{bmatrix} \cos\alpha \\ \sin\alpha \end{bmatrix} R_1(s)$$

$$\begin{bmatrix} Q_{R2}(s) \\ P_{R2}(s) \end{bmatrix} = [T] \cdot a_p \cdot [A] (1 - e^{-Ts}) \begin{bmatrix} \cos\beta \\ \sin\beta \end{bmatrix} R_2(s)$$

Where:

$$[A]=\begin{pmatrix} A_{11} & A_{12} \\ A_{21} & A_{22} \end{pmatrix}$$

Equation (4.25) can also be rewritten as

$$\begin{bmatrix} F_{R1}(s) \\ F_{R2}(s) \end{bmatrix}=\begin{bmatrix} Q_{R1}(s) \\ P_{R1}(s) \end{bmatrix}+\begin{bmatrix} Q_{R2}(s) \\ P_{R2}(s) \end{bmatrix}$$

Or more specifically

$$\begin{bmatrix} F_{R1}(s) \\ F_{R2}(s) \end{bmatrix}=a_p(1-e^{-Ts})[T][A][\begin{bmatrix} \cos\alpha \\ \sin\alpha \end{bmatrix}R_1(s)+\begin{bmatrix} \cos\beta \\ \cos\beta \end{bmatrix}R_2(s)]$$

Let

$$[T][A]\begin{bmatrix} \cos\alpha \\ \sin\alpha \end{bmatrix}=\begin{bmatrix} a_1 \\ a_{21} \end{bmatrix} \quad \text{and} \quad [T][A]\begin{bmatrix} \cos\beta \\ \cos\beta \end{bmatrix}=\begin{bmatrix} a_{12} \\ a_2 \end{bmatrix},$$

we simplify the above equation as

$$\begin{bmatrix} F_{R1}(s) \\ F_{R2}(s) \end{bmatrix}=a_p(1-e^{-Ts})\begin{bmatrix} a_1 & a_{12} \\ a_{21} & a_2 \end{bmatrix}\cdot\begin{bmatrix} R_1(s) \\ R_2(s) \end{bmatrix}$$

Notice that $\begin{bmatrix} a_1 & a_{12} \\ a_{21} & a_{21} \end{bmatrix}$ is a scalar matrix depending on [T], [A], α and β.

The equations of motion with mode-coupling terms for a two degree-of-freedom system are found as

$$(M_1s^2+C_1s+K_1)\cdot R_1(s)+a_p\cdot a_1\cdot(1-e^{-sT})\cdot R_1(s)+a_p\cdot a_{12}\cdot(1-e^{-sT})\cdot R_2(s)=0$$

$$(M_2s^2+C_2s+K_2)\cdot R_2(s)+a_p\cdot a_2\cdot(1-e^{-sT})\cdot R_2(s)+a_p\cdot a_{21}\cdot(1-e^{-sT})\cdot R_1(s)=0$$

Where:
M_1, M_2: the mass of mode 1 and mode 2, respectively
C_1, C_2: the damping of mode 1 and mode 2, respectively
K_1, K_2: the stiffness of mode 1 and mode 2, respectively

Or equivalently in a matrix form

$$[D]\cdot\begin{bmatrix} R_1(t) \\ R_2(t) \end{bmatrix} = 0$$

Where:

$$[D] = \begin{bmatrix} M_1 s^2 + C_1 s + K_1 + a_p \cdot a_1 \cdot (1 - e^{-sT}) & a_p \cdot a_{12} \cdot (1 - e^{-sT}) \\ a_p \cdot a_{21} \cdot (1 - e^{-sT}) & M_2 s^2 + C_2 s + K_2 + a_p \cdot a_2 \cdot (1 - e^{-sT}) \end{bmatrix}$$

Assuming that the mode coupling effects can be negligible, we simplify the matrix [D] as

$$[D] = \begin{bmatrix} M_1 s^2 + C_1 s + K_1 + a_p \cdot a_1 \cdot (1 - e^{-sT}) & 0 \\ 0 & M_2 s^2 + C_2 s + K_2 + a_p \cdot a_2 \cdot (1 - e^{-sT}) \end{bmatrix}$$

So the characteristic equation of a two-degree-of-freedom system is

$$[M_1 s^2 + C_1 s + K_1 + a_p \cdot a_1 \cdot (1 - e^{-sT})] \cdot [M_2 s^2 + C_2 s + K_2) + a_p \cdot a_2 \cdot (1 - e^{-sT})] = 0$$

The two uncoupled single-degree-of-freedom systems are described by the following equations:

$$M_1 s^2 + C_1 s + K_1 + a_p \cdot a_1 \cdot (1 - e^{-sT}) = 0$$

$$M_2 s^2 + C_2 s + K_2) + a_p \cdot a_2 \cdot (1 - e^{-sT}) = 0$$

Stability lobes are thus defined by these two equations with $s = j\omega$. It means that the lobes for a two-degree-of-freedom system can be figured out by the principle of superposition, i.e., superposing the plots of the two sets of lobes in a single stability diagram with spindle speed and depth of cut as the axes.
The same idea can be used for a general multiple-degree-of-freedom system.

Application and Verification

To verify this technique for a multiple-degree-of-freedom case, many tests have been done. The following example shows the procedure of finding

the stability lobes to predict chatter for a two-degree-of-freedom system. The machining conditions are listed in Table 4.10.

Table 4.10: Machining conditions

Machine tool	Matsuura (FX-5G)
Cutting tool	Helical End-mill
Tool diameter	16 (mm)
Number of teeth	4
Tool holder	Collet (NIKKEN)
Tool hangover	60 (mm)
Work-piece	aluminium
Fluid	Dry
Spindle speeds	14750 and 15500, 12700 and 23000 (rpm)
Pick feed	20 (mm)
Feed per tooth	0.05 (mm)

We started the machining at a depth of cut of 2 mm and used an increment of 1 mm. The transitional state was found from the depth of cut of 3 to 4 mm at the spindle speed of 14,750 rpm. The chatter frequency detected is 840 Hz with the highest amplitude of 958. So the limit depth of cut is set as 3.5 mm.
Similarly another transitional state was found at the spindle speed of 15,500 rpm with a limit depth of cut of 3.8 mm. The chatter frequency is 850 Hz.

From equation (4.14), after putting into these values of the chatter frequencies and tooth periods (i.e. 0.001 and 0.0009 (second) for the speeds of 14,750 and 15,500 rpm, respectively, with the number of teeth 4), we obtain the following simultaneous equations:

$$\omega_n^2 - (2\pi \cdot 840)^2 = 2\xi\omega_n (2\pi \cdot 840) \tan(\frac{(2\pi \cdot 840)0.001}{2})$$

$$\omega_n^2 - (2\pi \cdot 850)^2 = 2\xi\omega_n (2\pi \cdot 850) \tan(\frac{(2\pi \cdot 850)0.0009}{2})$$

Soloving these equations, we obtain

ω_n=5047 (rad./s) or 803 (Hz)

ξ = 0.09

Putting the values of ω_n and ξ, a_p=3.5 mm and $\omega_c=2\pi(840)$ (radian/s) into equation (4.17), the constant C_p is calculated as -0.07 (1/mm) for $\omega_c=2\pi(840)$ (radian/s) and -0.06 (1/mm) for a_p=3.8 mm and $\omega_c=2\pi(850)$ (radian/s).
The stability lobes for one mode are therefore calculated by using equation (4.16) and (4.17) and shown in Figure 4.31.

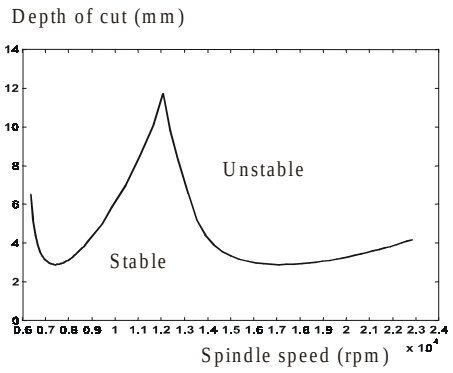

Figure 4.31: Stability lobes for the mode with ω_n = 803 Hz, ξ = 0.09, and C_p = -0.07(1/mm)

To find the other mode, we try cutting at the speed of 23,000 rpm.
A chatter frequency of 2610 Hz was detected. This is far away of the former chatter frequency which was around 840 ~ 850 Hz.
So, this clearly indicates that it might relate to a different vibration mode.
Searching for another spindle speed yielding chatter at a similar frequency resulted at 12,700 rpm with chatter frequency 2800 Hz.
Applying the same procedure as before, the natural frequency and damping ratio were found as

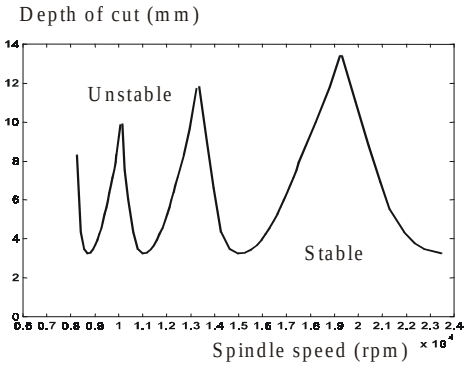

Figure 4.32: Stability lobes for the mode with ω_n = 2700 Hz, ξ = 0.025, and C_p = -0.016(1/mm)

ω_n=16967 (rad./s) or 2700 (Hz)

ξ = 0.025.

The constant C_p is -0.016 (1/mm) for a_p=3 mm and $\omega_c=2\pi(2610)$ (rad./s) and -0.012 (1/mm) for a_p=4 mm and ω_c

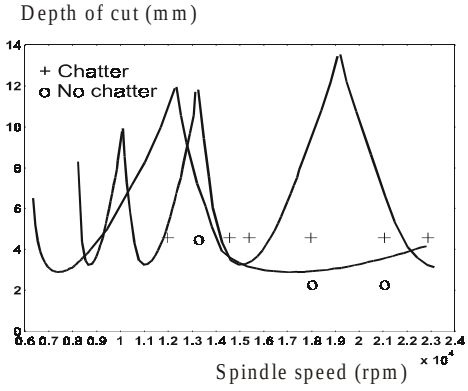

Figure 4.33: Stability lobes for the superposition of these two modes

$=2\pi(2800)$ (rad./s) at spindle speed 23,000 and 12700 rpm, respectively. Stability lobes were calculated, as shown in Figure 4.32.

The stability lobes for a two-degree-of-freedom system are just the superposition of these two lobes and shown in Figure 4.33 together with the experimental checks.
A narrowed relatively stable zone is identified. Its spindle speed is about 12,500 ~ 13,500 rpm if we consider only the high-speed range of 6,000 ~ 24,000 rpm.

4.5.7 A Strategy for Selection of Optimal Spindle Speed to Avoid Chatter

To optimize the cutting process and avoid chatter, we need a practical and systematic way by which a most stable zone can be found. A strategy for selection of optimal cutting parameters for chatter avoidance is illustrated in Figure 4.34.
We know that the depth of cut has the most significant influence on the occurrence of chatter. We start cutting from a suitable depth of cut at a given spindle speed of interest and increase or decrease the depth of cut, for example starting at 2 mm with an increment or decrement of 1 mm for machining of aluminum.
After the first cut the decision will be made for the further cut, based on whether or not chatter occurs. The technique for chatter detection has been given in section 4.5.6.
If there is no chatter, we will increase the depth of cut by the specified increment until chatter starts to occur or vice versa.
In the tests, normally three or four cuts are sufficient to identify a transition between stable and unstable machining. When a transitional state has been found, the limit depth of cut at which chatter starts to occur and the chatter frequency at that specific spindle speed are recorded.
This process is repeated to detect another transitional state. From the two known transitional states, the method introduced in section 4.5.5 is used to obtain the stability lobes for that mode, which is responsible for the chatter.
The local optimal stable zones are thus figured out based on the single-degree-of-freedom solution. We select the most stable speed, or the one with a possible highest limit depth of cut.
If during that optimization process, we detect chatter at a significantly different chatter frequency (and might point to a second vibration mode), we repeat the same procedure to obtain another set of stability lobes that is

responsible for the chatter detected at that frequency. This might lead to a 2nd set of stability lobes caused by a second vibration mode.
The procedure might then be repeated to identify a 3rd dominant mode and associated lobes if other chatter frequency or vibration modes are detected.
By following this iteration, a global optimal stable zone can be found after taking into account all possible dominant modes.
Fortunately, in practice after accounting for two or three modes good or even optimal cutting conditions can be found.

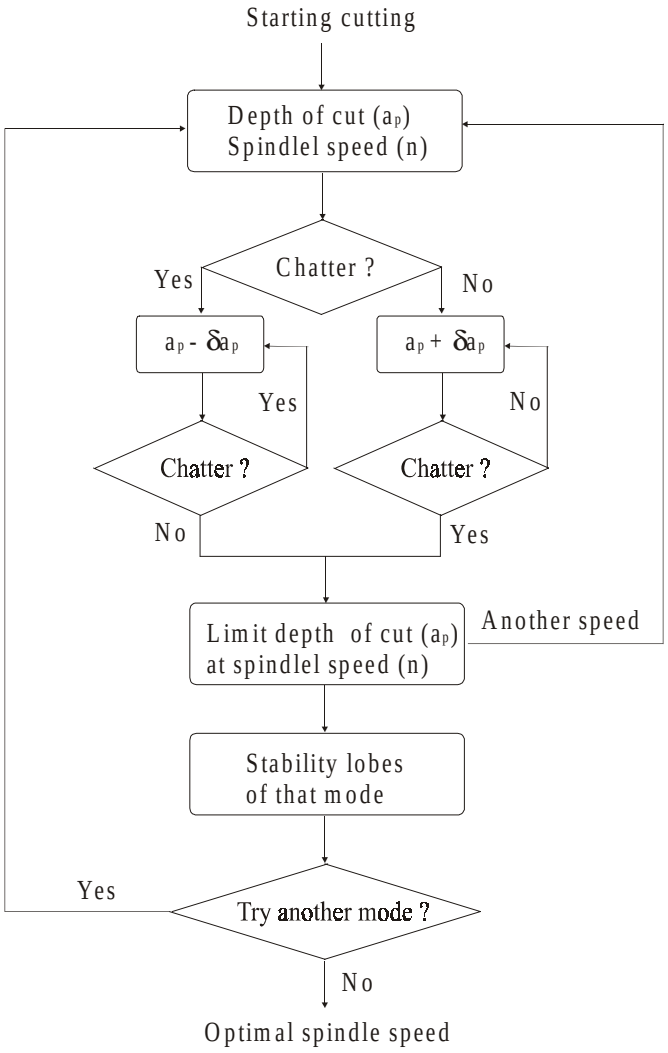

Figure 4.34: A strategy to find optimal spindle speed in high-speed milling

4.6 Summary

Chatter is an instability problem occurring during cutting. Whether or not chatter occurs depends on the closed-loop characteristic equation.
In high-speed milling, chatter frequency detected (refer to section 4.4) is often about 1 ~ 5 kHz. It implies that the machine structure's stiffness is relatively high compared to conventional machines.
For example, the measured FRF of the tool/tool-holder/spindle structure with hammer excitation (section 4.2) proves that a mode at the frequency of 1.05 kHz exists.
However, very high frequency modes in machine structures are difficult to measure with hammer excitation.
In this chapter, a method has been developed to identify modal parameters and process constant in high-speed milling.
Based on the understanding of high-speed milling coupled with structural dynamics (section 4.5.1 ~ 4.5.4), the structure's natural frequencies and damping ratios together with the process constants are found out from the cutting process itself for both a single (section 4.5.5) and multiple degree-of-freedom system (section 4.5.6) without doing measurements separately before cutting.
Experimental results given in section 4.4 prove that process stability is influenced by cutting parameters (spindle speed and depth of cut) and the structure's stiffness (the tool overhang).
A method for chatter prediction based on calculated stability lobes (i.e., in terms of spindle speeds and depth of cut at stability limit) is described in details in this chapter and verified in high-speed milling of aluminum.
It is worth noting that the process models developed in section 4.5.1~ 4.5.2 are only justified for high-speed milling cases. In conventional milling, the dynamic force induced from the variation of clearance angle may not be negligible (see section 4.5.1 and also 4.3.1). Those forces are not included in the models.
The strategy (section 4.5.7) for finding the most stable zone, i.e. the optimal spindle speed, shows the benefit of incorporating the stability lobes into CAD/CAM systems to predict good cutting conditions and avoid chatter in high-speed milling.

`

Chapter 5

General Conclusions and Future Work

Main Conclusions

In this dissertation, the instantaneous cutting forces and chatter vibration in high-speed milling have been studied.

- **Cutting Forces in High Speed Milling**

High speed milling is characterized by intermittent strong impact when the tool enters/exits the work-piece material. This strong impact due to high cutting speed produces high harmonic frequency components. Teeth passing frequency due to high spindle speed is also very high in high speed milling.
These high frequency harmonic excitations from strong impact and high teeth passing frequency make the structure vibrate in the neighborhood of the natural frequencies of the dynamometer.
The measured force signals are hence significantly distorted by the dynamic noise. If we use a low pass filter to filter out the noise, the high frequency harmonic components of the cutting force signals will be filtered out together with the dynamic noise as well.
As a result, we have to take the dynamic effects of the dynamometer into account in measuring/evaluating the high speed milling forces.

This thesis work proposes a force compensation method to discount the resultant inertia force of the workpiece together with the dynamometer.

This inertia force can be calculated from the accelerations measured and the equivalent mass of both the dynamometer and workpiece.

In addition, from this research a force coefficient method is developed. This method uses a new strategy to evaluate the instantaneous cutting forces in high speed milling. Firstly, the concept of engagement matrix is defined as functions of the nominal cutting parameters (spindle speed, feed per tooth and depth of cut) as well as the position angle of the tool tip. Secondly, the force signals are measured with a dynamometer. Thirdly, the set of simultaneous equations is established in the frequency domain based on the measured force signals. The force coefficients are worked out from these equations. Cutting forces are therefore readily identified based on these coefficients and the engagement matrix.

Moreover, this research has proven that O. Keinzle's force formula, which has been verified in turning operation, can still be used for milling operation in a wide range of engagement (chip thickness). By using O. Keinzle's formula for milling operation, the author introduces a technique to predict the instantaneous cutting force in 5-axis high speed milling with complicated tool geometry like e.g. a helical-fluted ball end mill.

Furthermore, an experimental observation of specific cutting forces at different cutting/spindle speeds has been done to have a feeling/understanding of the high speed milling process from the perspective of instantaneous cutting forces.

- **Chatter Vibration in High Speed Milling**

One of the key issues on process optimization is to avoid chatter and maximize the metal removal rate. Generally speaking, two strategies have been used for chatter suppression/avoidance in conventional milling. One is the online process control technique. The other is the process planning approach. These two strategies face challenges in high speed milling. The former needs to design a reliable feedback control system with a very quick response. The latter requires the frequency response function (FRF) of the structure, as seen at the tip of the tool, and the specific cutting forces for the models. The FRF is usually measured with hammer excitation. The specific cutting forces are obtained with a dynamometer. Chatter frequency detected in high speed milling is often very high (say about 1 ~ 5 kHz) due to the very high stiffness of the machine structure – the tool/tool-holder/spindle assembly. The very high frequency mode is difficult/impossible to measure with hammer excitation on one hand and

the specific forces are also not easy to obtain due to the difficulties in high speed milling force measurement on the other.

A new method is developed from this research to obtain the knowledge of modal parameters and process constants in case of high-speed milling. The basic idea of this method is that the structure's natural frequencies and damping ratios together with the process constants are picked out from the cutting process itself without doing measurement separately before cutting.

This doctoral research also develops a new technique for chatter detection. This technique takes into account the three dominant harmonic components of the acoustic noise, measured separately in air and material cutting, and compares their frequencies and amplitudes to tell whether or not chatter occurs.

Furthermore, through this research work coupling models of the structural and process dynamics for both a single and multiple degree-of-freedom system are derived from the fundamentals of chatter theory. These models have been successfully applied to analyze process stability. By using these models, the author has satisfactorily explained a new observation – the phase shift can have the value beyond the range $[2(0.5+k)\pi, 2(k+1)\pi]$ for a single degree-of-freedom system. This observation contradicts the generally accepted viewpoint, i.e. phase shift must always lie in the range of $[2(0.5+k)\pi, 2(k+1)\pi]$ for a single degree-of-freedom system.

Finally a new strategy for finding the most stable cutting zone at the optimal spindle speed is developed from this research. This iterative strategy shows the bright future in using CIM technology to maximize metal removal rate.

- **Recommendations for Future Research**

Developing a kind of software, which can be incorporated into the existing data acquisition system to measure instantaneous high-speed milling forces.

Using the developed optimization strategy to machine hard materials and comparing both the tool-wear and surface roughness to those without using the optimization strategy.

Bibliography

1. Agapiou, J., “Tool-holder/Spindle Interfaces for CNC Machine Tools”, Annals of the CIRP, Vol.44/1: 383-387, 1995.

2. Altintas, Y., A. Spence, “End Milling Force Algorithms for CAD Systems” Annals of the CIRP, Vol.40/1: 31-34, 1991.

3. Altintas, Y., Budak, E., Analytical Prediction of stability Lobes in Milling, Annals of the CIRP, Vol. 44/1: 357-362, 1995.

4. Altintas, Y., Lee, P., 1996, A General Mechanics and Dynamics Model for Helical End Mills, Annels of CIRP, Vol. 45/1: 59-64.

5. Altintas, Y., Lee, P., 1998, Mechanics and Dynamics of Ball End Milling, ASME Trans. J. Manuf. Science and Eng. Vol.1: 684-692.

6. Armarego, E. J. A., and Deshpande, N. P., “Computerized End Milling Force Predictions with Cutting Models Allowing for Eccentricity and Cutter Deflections”, Annals of the CIRP, Vol.40/1: 25-29, 1991.

7. Armarego, E. J. A., and Wang, J., “Computer-Aided Predictive Cutting Model for Forces in Face Milling Allowing for Tooth Run-out”, Annals of the CIRP, Vol.44/1: 43-48, 1995.

8. Balaji, A. K., “The Effects of Cutting Tool Thermal Conductivity on Tool-Chip Contact Length and Cyclic Chip Formation in Machining with Grooved Tools”, Annals of the CIRP, Vol.48/1: 33-37, 1999.

9. Bedi, S., and Gravelle, S., “Principal Curvature Alignment Technique for Machining Complex Surfaces”, ASME Trans. J. Eng. for Industry, Vol.119: 756-765, 1997.

10. Ber, A. and Rotberg, J., “A Method for Cutting Force Evaluation of End Mills”, Annals of the CIRP, Vol.37/1: 37-40, 1998.

11. Blum, T., Inasaki, I., A Study on Acoustic Emission from the Orthogonal Cutting Process, Journal of Engineering for Industry, Vol.112: 203-211, 1990.

12. Budak, E., Altintas, Y., Armarego, E.J.A., 1996, Prediction of Milling Force Coefficients from Orthogonal Cutting Data, ASME Trans. J. Eng. for Industry, Vol.118: 216-224.

13. Chandrasekaran, H. and Thuvander, A., “Modelling of Tool Stresses in Peripheral Milling”, Annals of the CIRP, Vol.31/1: 41-44, 1998.

14. Dautzenberg, J. H., Van Dijck, J. A. B., and Kals, J, A. G., “Metal Structures by Friction in Mechanical Working Processes”, Annals of the CIRP, Vol.38/1: 567-570, 1989.

15. Davies, M. A. and Dutter, B., “On the Dynamics of High-Speed Milling with Long, Slender Endmills”, Annals of the CIRP, Vol.47/1: 55-60, 1998.

16. Delio, T., Tlusty, J., Smith, S., Use of Audio Signals for Chatter Detection and Control, ASME Trans. J. Eng. for Industry, Vol.114: 146-157, 1992.

17. Eugene, R. “Tooling Structure: Interface between Cutting /edge and Machine Tool”, Annals of the CIRP, Vol.49/2: 591-631, 2000.

18. Grabec, I., Gradisek, J., and Govekar, E., “A New Method for Chatter Detection in Turning”, Annals of the CIRP, Vol.48/1: 29-32, 1999.

19. Habraken, J. H., “Formability of Rapid-Solidification-Processed Hypereutectic Al-Si Alloys”, Annals of the CIRP, Vol.43/1: 211-214, 1994.

20. Hahn, N. H., and Tobias, S., A., 1974, A theory of nonlinear regenerative chatter, J. Eng. Ind. 96: 247-255.

21. Heisel, U. and Feinauer, A. “Dynamic Influence on Workpiece Quality in High-Speed Milling”, Annals of the CIRP, Vol.48/1: 321-324, 1999.

22. Heisel, U., “Vibrations and Surface Generation in Milling”, Annals of the CIRP, Vol.43/1: 337-340, 1994.

23. Kaldor, S., Rafael, M., and Messinger, D., “On the CAD of Profiles for Cutters and Helical Flutes – Gemetrical Aspects”, Annals of the CIRP, Vol.37/1: 53-56, 1998.

24. Kops, L., and Vo, D. T., “Determination of the Equivalent Diameter of an End Mill Based on its Compliance”, Annals of the CIRP, Vol.39/1: 93-96, 1990.

25. Kruth, J.-P., Erzi, A.-G., Lauwers, B., 1996, Influence of Tool Orientation on Surface Accuracy in 5-axis Milling, Proc. Intern. Manuf. Eng. Conf.: 137-139, 1996.

26. Kruth, J.-P., Klewais, P., “Optimization and Dynamic Adaptation of the Cuttk. er Inclination during Five-Axis Milling of Sculptured Surfaces”, Annals of the CIRP, Vol.43/1: 443-448, 1994.

27. Kruth, J.-P., Vanherck, P., Liu, A.M., A Solution to Identification of Force Coefficients in High-speed Milling with Complex Cutting Edge Geometry, Proc. 1st Intern. Seminar on Progress in Innovative Manuf. Eng. pp: 27-32, Italy, 2001.

28. Kruth, J.-P., Vanherck, P., Liu, A.M., analysis of specific cutting forces at different cutting speeds in milling of steel with ball end mill, 3rd intern. conf. on metal cutting and high speed machining, pp: 91-94, metz, France, 2001.

29. Kruth, J.-P., Vanherck, P., Liu, A.M., Dynamics of Milling System and Force Measurements in High-Speed Milling, Proc. 5th National Congress on Theoretical and Applied Mechanics: pp: 271-274, Belgium, 2000.

30. Kwon, K. B., and Cho, D. W., “A Fluid Dynamic Analysis Model of the Ultra-Precision Cutting Mechanism”, Annals of the CIRP, Vol.48/1: 43-48, 1999.

31. Lazoglu, I. And Liang, S. Y., “Modelling of Ball-End Milling Forces with Cutter Axis Inclination”, Trans. ASME Journal of Engineering for Industry, 122: 3-11, 2000.

32. Mamoru, Shin’ichi, Taksshi, and Takaaki, “Development of a System Which Dynamically Determines Machining Conditions Based on Real-Time Machining State Detection”, The Japan Society for Precision Engineering, Advancement of Intelligent Production, pp: 221-225, 1994.

33. Merrit, H.E., “Theory of Self-excited Machine Tool Chatter,” Trans. ASME Journal of Engineering for Industry, 87: 447-454, 1965.

34. Minis, I., and Tembo, A., “Experimental Verification of a Stability Theory for Periodic Cutting Operations”, ASME Trans. J. Eng. for Industry, Vol.115: 9-14, 1993.

35. Minis, I., Yanushevsky, R., A New Theoretical Approach for the Prediction of Machine Tool Chatter in Milling, ASME Trans. J. Eng. for Industry, Vol.115/1: 1-8, 1993.

36. Minis, I., Yanushevsky, R., Tembo, R., and Hocken, R., Analysis of Linear and Non-linear Chatter in Milling, Annals of the CIRP, Vol.39: 459-462, 1990.

37. Montgomery, D., Altintas, Y., 1991, “Mechanism of Cutting Force and Surface Generation in Dynamic Milling”, Trans. ASME J. Eng. for Ind., Vol.113: 160-168.

38. Morishige, K., Takeuchi, Y., and Kase, K., “Tool Path Generation Using C-Space for 5-Axis Control Machining”, ASME Trans. J. Eng. for Ind, Vol.121: 144-149, 1999.

39. Mounayri, H. and Spence, A. D., “Milling Process Simulation – A Generic Solid Modeller Based Paradigm”, Trans. ASME J. Eng. for Ind., Vol.120: 23-221, 1998.

40. Nayfeh, A., Chin, C. M., and Pratt, J., “Perturbation Mehtods in Nonlinear Dynamics – Applications to Machining Dynamics”, Trans. ASME J. Eng. for Ind., Vol.119: 485-493, 1997.

41. Ostafierv, V. and Ostafiev, D., “Distrbution of Cutting Tool Contact Loads along Rake and Flank Surfaces”, Annals of the CIRP, Vol.43/1: 55-58, 1994.

42. Park, S., and Jun, Y. T., “Determining the Cutting Conditions fpr Sculptured Surfsce Machining”, Int. J. Adv. Manuf. Technol. Vol. 8: 61-70, 1993.

43. Peters, J., Vanherck, P. Van Brussel, H., “The Measurement of the Dynamic Cutting Coefficient”, Annals of the CIRP, Vol.2/1: 129-136, 1971.

44. Pratt, J. R., and Davies, M. A., “Dynamic Interrogation of a Basic Cutting Process”, Annals of the CIRP, Vol.48/1: 39-42, 1999.

45. Roichard, D., “New Developments in the High-Speed Machining of Hardened Mould and Die Steels”, Prototyping and Tooling, Vol. 6: 52-58, 1998.

46. Rotberg, J., Shoval, S., Ber, A., 1997, Fast Evaluation of Cutting Forces in Milling Applying no Approximate Models, Intern. J. of Advanced Manuf. Technology, Vol. 13: 17-26.

47. Schulz, H., and Hock, St., “High-Speed Milling of Dies and Moilds – Cutting Conditions and Technology”, Annals of the CIRP, Vol.44/1: 35-38, 1995.

48. Schulz, H., and Herget, T., “Simulation and Measurement of Transient Cutting Force Signal in High-Speed Milling”, Production Engineering, I(2): 19-22, 1994.

49. Schulz, H., and T. Wurz, Balancing Requirements for Fast Rotating Tools and Spindle Systems, Annals of CIRP, Vol. 47/1/: 321-324, 1998.

50. Sexton, J.S., Stone, B.J., The Stability of Machining with Continuously Varying Spindle Speed, Annals of the CIRP, Vol.24/1: 405-409, 1978.

51. Shrida, R., Hohn, R. E., and Long, G. W., “A General Formulation of the milling Process Equation”, J. Eng. Ind. 90: 317-334, 1968a.

52. Shrida, R., Hohn, R. E., and Long, G. W., “A Stability Algorithm for the General milling Process”, J. Eng. Ind. 90: 317-334, 1968b.

53. Smith, S. Jacobs, T. P., and Halley, J., “The Effect of Drawbar Force on Metal Removal Rate in Milling”, Annals of the CIRP, Vol.48/1: 293-296, 1999.

54. Smith, S. Tlusty, J., Efficient Simulation Programs for Chatter in Milling, Annals of the CIRP, Vol.42/1: 463-466, 1993.

55. Smith, S. Tlusty, J., Stabilising Chatter by Automatic Spindle Regulation, Annals of the CIRP, Vol.41/1: 433-436, 1992.

56. Smith, S., and Tlusty, J., “An Overview of Modeling and Simulation of the Milling process”, J. of Eng. For Industry, Vol. 113: 169-175, 1991.

57. Smith, S., Winfough, W.R., and Halley, J., “The Effect of Tool Length on Stable Metal Removal Rate in High-Speed Milling”, Annals of the CIRP, 47/1: 307-310, 1998.

58. Spiewak, S., “An Improved Model of the Chip Thickness in Milling”, Annals of the CIRP, 44/1: 39-42, 1995.

59. Spiewak, S., “Instrumented Milling Cutter for In-Process Measurement of Spindle Error Motion”, Annals of the CIRP, 41/1: 429-432, 1992.

60. Sutherland, J. W. and Devor, R. E., “An Improved Method for Cutting Force and Surface Error Prediction in Flexile and Milling Systems”, J. of Eng. For Industry, Vol. 108: 269-279, 1986.

61. Takemura, T., Kitamura, T., Hoshi, T., Adaptive Suppression of Chatter by Programmed Variation of Spindle Speed, Annals of the CIRP, Vol.23/1: 121-122, 1974.

62. Taminiau, D. A., Dautzenberg, J. H., “Bluntness of the Tool and Process Forces in High-Precision Cutting”, Annals of the CIRP, Vol.40/1: 65-68, 1991.

63. Teti., R., Dornfeld, D. A., Modelling and Experimental Analysis of Acoustic Emission from Metal Cutting, Journal of Engineering for Industry, Vol.111: 229-237, 1989.

64. Teti., R., La., U., Compare Cutting Conditions and Work Materials State Identification through Acoustic Emission, Annals of the CIRP, Vol.141/1: 89-96, 1992.

65. Tian, J. and Hutton, S., G., “Chatter Instability in Milling Systems with Flexible Rotating Spindles – A New Theoretical Approach”, J. Eng. Ind. 123: 1-9, 2001.

66. Tlusty, J., “Dynamics of High-speed Milling”, J. Eng. Ind. Vol.108: 59-67, 1986.

67. Tlusty, J., “High-Speed Maching”, Annals of the CIRP, 42/2: 733-738, 1993.

68. Tlusty, J., and Ismail, F., “Basic Nonlinearity in Machining Chatter”, Annals of the CIRP, 30: 21-25, 1981.

69. Tlusty, J., and Smith, S., “High-Speed High Power Spindles with Roller Bearings”, Annals of the CIRP, 36/1: 267-272, 1987.

70. Tlusty, J., and Smith. S., Winfough, W., R., “Technique for the Use of Long Slender End Mills in High-Speed Milling”, Annals of the CIRP, 45/1: 393-396, 1996.

71. Tlusty, J., Smith, S., Zamudio, C., “New NC Routines for Quality in Milling”, Annals of the CIRP, 39/1: 517-521, 1990.

72. Tlusty,J., and Ismail, F., Special Aspects of Chatter in Milling. ASME J. Vib., Stress, Reliab. Des. 105: 24-32, 1983.

73. Tlusty,J., and Ismail, F., Special Aspects of Chatter in Milling. ASME J. Vib., Stress, Reliab. Des. 105: 24-32, 1983.

74. Tonshoff, H. k., “High-Speed or High-Performance Cutting – a Comparison of New Machining Technilogies”, Production Engineering Vol. VIII/1: 5-8, 2001.

75. Tonshoff, H. k., Arendt, C., Ben Amor, R., “Cutting Hardened Steel”, Annals of the CIRP, 49/2: 1-19, 2000.

76. Toshimichi, M., Eiji, S., “Analysis of Thermal Deformation of an Ultra-precision Air Spindle System”, Annals of the CIRP, Vol.47/1: 315-319, 1998.

77. Van Brussel, H., 1971, Dynamische Analyse Van het Verspaningsproces, Doct. Dissertatie, Leuven.

78. Weck, M., Hennes, N., Krell, M., “Spindle and Toolsystems with High Damping”, Annals of the CIRP, Vol.48/1: 297-302, 1999.

79. Weck, M., Koch, A., “Spindle-Bearing Systems for High-Speed Applications in Machine Tools”, Annals of the CIRP, Vol.24/1: 445-448, 1993.

80. Weck, W., Verhaag, E., Gather, M., Adaptive Control for Face-Milling Operations with Strategies for Avoiding Chatter Vibrations and for Automatic Cut Distribution, Annals of the CIRP, Vol.24/1: 405-409, 1975.

81. Weinert, K., and Mehnen, J., “On the Analysis of the Dynamics of High-Speed Milling by Means of Time Series Analysis Methods”, Production Engineering, Vol. VI/2: 21-24, 1999.

82. Wertheim, R., Satran, A., and Ber, A., “Modifications of the Cutting Edge Geometry and Chip Formation in Milling”, Annals of the CIRP, Vol.43/1: 63-68, 1994.

83. Weule, H. and Schmidt, J., “Simulation of the High_Speed Milling Process”, Production Engineering Vol. VII/2: 23-26, 2000.

84. Wu, K.R., Bayer, R.G., Engle, P.A., and Sun, D.C., “Wear of Physical Vapor Deposition TiN Coatings Sliding Against Cr-Steel and WC Counterbodies”, ASME Trans. J. Eng. for Industry, Vol.120: 482-488, 1998.

85. You, S. J., and Ehmann, K. F., “Synthesis and Generation of Surfaces Milled by Ball Nose End Mills under Teriary Cuter Motion”, J. of Eng. For Industry, Vol. 113: 17-24, 1991.

86. Yucesan, G., and Altintas, Y., “Prediction of Ball End Milling Forces”, ASME Trans. J. Eng. for Industry, Vol.1, No 1: 95-103, 1996.

87. Zeljkovic, M., and Gatalo, R., “Experimental and Computer Aided Aqnalysis of High-Speed Spindle Assembly Behaviour”, Annals of the CIRP, Vol.48/1: 325-328, 1999.

Appendix A

MatLab Program for Force Prediction

```
%Input
clear;
%correction coefficients
ro=10;
io=15;
c1=(109-1.5*ro)/100;
c2=(94-1.5*io)/100;
c3=1.3;
c4=0.9;

%force model coefficients and index
kc11=1765;  kc=kc11*c1*c2*c3*c4;  kf=0.3;  kb=0.3;   mc=0.25;

%tool parameters
Ro=5;  Bo=pi/6;  Z=2;

%cutting conditions
ap=1.5;  ae=3;   fz=0.05;

%setting initial values
I=61;
J=30;

%Main program
%calculating the limits of location angles
gc=(Ro-(Ro*Ro-ae*ae/4)^0.5)/Ro*cot(Bo);
gmax=ap/Ro*cot(Bo);

%spacing both rotation and location angles
a=2*pi/I;
g=gmax/J;

%setting empty matrices
Ftg=zeros(3,I);
Jsum=zeros(3,J);
Fgn=zeros(3,Z);
```

```
T=zeros(3,Z);

%force computation
for i=1:I
for j=1:J
for n=1:Z

%fixing entrance and exit angles and active cutting ranges
an(n)=i*a+(n-1)*2*pi/Z;
gn(n)=j*g;
if round((an(n)-gn(n))/(2*pi))<=(an(n)-gn(n))/(2*pi)
kn(n)=round((an(n)-gn(n))/(2*pi));
else
kn(n)=round((an(n)-gn(n))/(2*pi))-1;
end;
if gc<=gn(n) & gn(n)<=gmax
xae=ae-Ro*(gn(n)*cot(Bo)*(2-gn(n)*cot(Bo)))^0.5;
yae=-(2*Ro*ae*(gn(n)*cot(Bo)*(2-gn(n)*cot(Bo)))^0.5-ae*ae)^0.5;
R=Ro*(1-(1-gn(n)*cot(Bo))^2)^0.5;
if xae>=0
aentn(n)=acos(yae/R);
else
aentn(n)=acos(yae/R)+2*(pi-acos(yae/R));
end;
else
aentn(n)=pi/2;
end;
aexn(n)=3*pi/2;
if 2*kn(n)*pi+aentn(n)<=an(n)-gn(n) & an(n)-
gn(n)<=2*kn(n)*pi+aexn(n)
G(n)=1;
else
G(n)=0;
end;

%calculating the width(b) and depth(h) of cut and transformation matrix
b(n)=g*((Ro^2*(1-(1-
gn(n)*cot(Bo))^2)+(Ro^2*cot(Bo)^2)+(Ro^2*cot(Bo)^2*(1-
gn(n)*cot(Bo))^2)/(1-(1-gn(n)*cot(Bo))^2)))^0.5;
h(n)=((fz*(1-(1-gn(n)*cot(Bo))^2)^0.5)*abs(cos(an(n)-gn(n))))^(1-mc);
T(:,n)=[-cos(an(n)-gn(n))-kf*sin(an(n)-gn(n));sin(an(n)-gn(n))-
kf*cos(an(n)-gn(n));kb];
```

```
%total force calculation
Fgn(:,n)=kc11*b(n)*h(n)*T(:,n)*G(n);
sum(Fgn')';
Jsum(:,j)=sum(Fgn')';
Ftg(:,i)=sum(Jsum')';
end;
end;
end;

%calculating mean forces
for m=1:I
mFtgx(m)=mean(Ftg(1,:));
mFtgy(m)=mean(Ftg(2,:));
mFtgz(m)=mean(Ftg(3,:));
end;

%Output
x=1*a*180/pi:a*180/pi:I*a*180/pi;
%whitebg;
plot(x,Ftg,'k');
hold on
plot(x,mFtgx,'r');
plot(x,mFtgy,'g');
plot(x,mFtgz,'b');
hold off
and
```

Appendix B

Derivation of Mathematical Equation

For functions x(t – T) and x(t), we have the following equation

$$x(t-T) = e^{-TD}x(t)$$

Where:
t: a real variable
T: a constant
D: the operator d/dt

Proof:
From Taylor expansion formula, we have

$$\begin{aligned} x(t-T) &= x(t) - x'(t)T + \frac{x''(t)}{2!}T^2 - \frac{x'''(t)}{3!}T^3 + \cdots \\ &= 1 - T\frac{dx(t)}{dt} + \frac{T^2}{2!}\frac{d^2x(t)}{dt^2} - \frac{T^3}{3!}\frac{d^3x(t)}{dt^3} + \cdots \end{aligned}$$

and

$$e^{-TD} = 1 - TD + \frac{T^2D^2}{2!} - \frac{T^3D^3}{3!} + \cdots$$

The right-hand side of the equation can thus be rewritten as

$$\begin{aligned} e^{-TD}x(t) &= (1 - TD + \frac{T^2D^2}{2!} - \frac{T^3D^3}{3!} + \cdots)x(t) \\ &= 1 - TDx(t) + \frac{T^2D^2x(t)}{2!} - \frac{T^3D^3x(t)}{3!} + \cdots \\ &= 1 - T\frac{dx(t)}{dt} + \frac{T^2}{2!}\frac{d^2x(t)}{dt^2} - \frac{T^3}{3!}\frac{d^3x(t)}{dt^3} + \cdots \end{aligned}$$

So

$$x(t-T) = e^{-TD}x(t)$$

Appendix C

MatLab Program for Lobe Computation

```
%stability lobe simulation for single degree-of-freedom system

clear;
rpm_try=13500;
ap_try=3.5;
a_max=[5];
a_min=[2];
freq_natur=[3051/1.1];
rpm_start=12000;
rpm_max=24000;
interval=10;
phase_shift=[0;0.75];
num_tooth=4;
num_natur=1;
num_wave=15;

%model the best and the worst possible spindle speeds for each modes
for k=1:num_natur
  num_wave=12;
  %create best_row and worst_row of the num_wave
  for j=1:num_wave
    best_row(j)=60*freq_natur(k)/(num_tooth*(j+phase_shift(1)));
    worst_row(j)=60*freq_natur(k)/(num_tooth*((j-1)+phase_shift(2)));
  end;
  %cut of the rpms of both the best and worst rows to fit into rpm_start

while(num_wave>1)&(best_row(num_wave)<rpm_start)&(worst_row(nu
m_wave)<rpm_start)&(best_row(num_wave-1)<rpm_start)
    best_row(num_wave)=[];
    worst_row(num_wave)=[];
    num_wave=num_wave-1;
  end;
  %cut off the rpms of both the best and worst rows to fit into rpm_max
  [nu,num_worst]=size(worst_row);
```

```
  while
(num_worst>1)&(worst_row(1)>rpm_max)&(best_row(1)>rpm_max)&(
worst_row(2)>rpm_max)
     best_row(1)=[];
     worst_row(1)=[];
     num_worst=num_worst-1;
  end;
  %combine the two rows
  rpm_best_worst=sort([best_row worst_row]);

  %assign possible depths of cut to the best and worst cases
  [n,M]=size(rpm_best_worst);
 m=M/2;
 for i=1:2:2*m-1
  ap(i,k)=a_max(k);
 end;
 for i=2:2:2*m
  ap(i,k)=a_min(k);
 end;

%find the coefficients of the curves--left and right ones with respect to the
lowest points
  for i=1:2:2*m-1
     an(i,k)=(ap(i,k)-ap(i+1,k))/(rpm_best_worst(i)-
rpm_best_worst(i+1))^2;
  end;
  for i=2:2:2*(m-1)
     an(i,k)=(ap(i+1,k)-ap(i,k))/(rpm_best_worst(i+1)-
rpm_best_worst(i))^2;
  end;

%interpolate the ap values for the whole speed range for all possible
modes
    for i=1:2:2*m-1
        if rem((rpm_best_worst(i+1)-rpm_best_worst(i)),interval)==0
           num_points(i,k)=(rpm_best_worst(i+1)-
rpm_best_worst(i))/interval;
        else
           num_points(i,k)=fix((rpm_best_worst(i+1)-
rpm_best_worst(i))/interval)+1;
        end;
      for j=1:num_points(i,k)
         rpm_wave_matrix(j,i)=rpm_best_worst(i)+(j-1)*interval;
```

```
        f(j,i)=an(i,k)*(rpm_wave_matrix(j,i)-
rpm_best_worst(i+1))^2+ap(i+1,k);
      end;
   end;
   for i=2:2:2*(m-1)
       if rem((rpm_best_worst(i+1)-rpm_best_worst(i)),interval)==0
         num_points(i,k)=(rpm_best_worst(i+1)-
rpm_best_worst(i))/interval;
       else
         num_points(i,k)=fix((rpm_best_worst(i+1)-
rpm_best_worst(i))/interval)+1;
       end;
     for j=1:num_points(i,k)
        rpm_wave_matrix(j,i)=rpm_best_worst(i)+(j-1)*interval;
       f(j,i)=an(i,k)*(rpm_wave_matrix(j,i)-rpm_best_worst(i))^2+ap(i,k);
     end;
  end;

[row,col]=size(f);
num_tot=row*col;
ap_tot_col=reshape(f,num_tot,1);
rpm_tot_col=reshape(rpm_wave_matrix,num_tot,1);

%cancel zeros of ap_tot_col and rpm_tot_col
i=1;
count=1;
   while count<=num_tot
      if ap_tot_col(i)~=0
         count=count+1;
         i=i+1;
      else
         count=count+1;
         ap_tot_col(i)=[];
         rpm_tot_col(i)=[];
      end;
   end;

   %set ap_tot_col and rpm_tot_col to the rpm_max range
   [num_rpm_max,n_]=size(rpm_tot_col);
   i=1;
   count=1;
   while (count<=num_rpm_max)&(rpm_tot_col(count)<=rpm_max)
     count=count+1;
```

```
      i=i+1;
    end;
    while count<=num_rpm_max
      ap_tot_col(i)=[];
      rpm_tot_col(i)=[];
      count=count+1;
    end;

 % save the information of rpm_tot_col of each mode and set up two
matrices to store rpm and ap for all modes
    [R,c]=size(rpm_tot_col);
   first_elem(k)=rpm_tot_col(1);
   R_tot(k)=R;
   for i=1:R
     rpm_tot_matrix(i,k)=rpm_tot_col(i);
     ap_tot_matrix(i,k)=ap_tot_col(i);
   end;
   f=[];
   rpm_wave_matrix=[];
end;
%(ending the for k=1:natur loop here)


%find the row number of starting rpm for each k
  first_max=max(first_elem);
  for k=1:num_natur
     i=1;
     while rpm_tot_matrix(i,k)<first_max
      i=i+1;
     end;
      row_rpm_start(k)=i;
  end;

%calculate the number of each k from the starting rpm to the end of each
k
for k=1:num_natur
   num_st_end(k)=R_tot(k)-row_rpm_start(k)+1;
end;

%set up new common matrics to store rpm and ap
num_common=min(num_st_end);
for k=1:num_natur
   for i=1:num_common
```

```
    rpm_matrix_common(i,k)=rpm_tot_matrix(row_rpm_start(k)+i-1,k);
    ap_matrix_common(i,k)=ap_tot_matrix(row_rpm_start(k)+i-1,k);
  end;
end;
ap_min=ap_matrix_common;


%plot(rpm_matrix_common,ap_matrix_common,'b');
plot(rpm_matrix_common(:,1),ap_matrix_common(:,1),'k');
hold on
%plot(rpm_matrix_common(:,2),ap_matrix_common(:,2),'b');
%plot(rpm_matrix_common(:,3),ap_matrix_common(:,3),'g');
%plot(rpm_matrix_common(:,1),ap_min,'r');


%find N most stable speeds rpm and ap
N=12;
rpm_min=rpm_matrix_common(:,1);

for n=1:N
  [val_max,pos_max]=max(ap_min);
  most_stable_rpm(n)=rpm_min(pos_max);
  ap_reference(n)=val_max;
  ap_min(pos_max)=[];
  rpm_min(pos_max)=[];
end;

%find the shift value of the lobe with the specified lobe shape by a_max
and a_min values
i=1;
%find the position of rpm_try by the i value
while rpm_matrix_common(i)<rpm_try
  i=i+1;
end;
%set the shift value and change the ap_matrix_common value
ap_shift=ap_try-ap_matrix_common(i);
ap_matrix_common=ap_matrix_common+ap_shift;

plot(rpm_matrix_common,ap_matrix_common,'r');
ap_shift
most_stable_rpm
ap_reference
a_max
```

```
%stability lobe simulation for a multiple degree-of-freedom system

clear;
ap_ch=[4;4];
fc=[3116;3184];
rpm_chat=[12000;12500]/60;
rpm_start=12000/60;
rpm_max=23000/60;
num_tooth=2;

%find damping ratio (c) and natural frequency (fn) with e=2pi-
2arctan(r^2-1/2cr),r=fc/fn
wcT1=2*pi*fc(1)/rpm_chat(1);
wcT2=2*pi*fc(2)/rpm_chat(2);
a1=sin(wcT1)/(1-cos(wcT1))/fc(1);
a2=sin(wcT2)/(1-cos(wcT2))/fc(2);
fn=sqrt((a1*fc(1)*fc(1)-a2*fc(2)*fc(2))/(a1-a2));
c1=a1*(fn*fn-fc(1)*fc(1))/(2*fn*fc(1));
c2=a2*(fn*fn-fc(2)*fc(2))/(2*fn*fc(2));
r1=fc(1)/fn;
r2=fc(2)/fn;
a1
a2
fn
c1
c2
c=c1
%find system and process coefficient with blim=co/Re[G]=co*((1-
r^2)^2+4*c^2*r^2)/(1-r^2)
co1=ap_ch(1)*(1-r1^2)/((1-r1^2)^2+4*c^2*r1^2);
co2=ap_ch(2)*(1-r2^2)/((1-r2^2)^2+4*c^2*r2^2);
co1
co2
if (co1>0)&(co2>0)
  co=mean([co1 co2]);
end;
if (co1<0)&(co2<0)
  co=abs(mean([co1 co2]));
end;
if (co1<0)&(co2>0)
  co=co2;
end;
if (co2<0)&(co1>0)
```

```
  co=co1;
end;

%find the range of number of waves (Nst ~Nmax) within the defined
speed range (rpm_start ~ rpm_max)
Nmax=fix(fn/(num_tooth*rpm_start));
Nst=fix(fn/(num_tooth*rpm_max));

%find the lobe alim and corresponding rpm_spin from Nmax to Nst

if Nmax~=0
  N=Nmax:(-1):Nst;
else
  N=0;
end;
r=1.0005:0.002:0.002*8+1.0005;
N
[row,n_wave]=size(N);
[ro,n_point]=size(r);

for k=1:n_wave
  for i=1:n_point
    er(i)=2*pi-2*atan((r(i)^2-1)/(2*c*r(i)));
    rpm_spin(i,k)=60*fn*r(i)/(num_tooth*(N(k)+er(i)/2/pi));
    alim(i,k)=co*((1-r(i)^2)^2+4*c^2*r(i)^2)/(1-r(i)^2);
    alim_plot(i,1)=abs(alim(i,k));
    rpm_spin_plot(i,1)=abs(rpm_spin(i,k));
  end;
  rpm_spin(1,k)
  plot(rpm_spin_plot,alim_plot,'k');
  hold on;
  alim_plot=[];
  rpm_spin_plot=[];
end;
```